Nuclear Science and Techniques (2026) 37:57
https://doi.org/10.1007/s41365-025-01876-0

Conceptual design of the muonium-to-antimuonium conversion experiment (MACE)

Ai-Yu Bai[1,2] · **Han-Jie Cai**[3,4] · **Chang-Lin Chen**[5] · **Si-Yuan Chen**[1,2] · **Xu-Rong Chen**[3,4,6] · **Yu Chen**[1,2] · **Wei-Bin Cheng**[7] · **Ling-Yun Dai**[5,8] · **Rui-Rui Fan**[9,10,11] · **Li Gong**[7] · **Zi-Hao Guo**[12] · **Yuan He**[3,4] · **Zhi-Long Hou**[9] · **Yin-Yuan Huang**[1,2] · **Huan Jia**[3,4] · **Hao Jiang**[1,2] · **Han-Tao Jing**[9] · **Xiao-Shen Kang**[7] · **Hai-Bo Li**[4,9] · **Jin-Cheng Li**[3,4] · **Yang Li**[9] · **Da-Ming Liu**[13] · **Shu-Lin Liu**[4,9,11] · **Gui-Hao Lu**[1,2] · **Han Miao**[4,9] · **Yun-Song Ning**[1,2] · **Jian-Wei Niu**[3,14] · **Hua-Xing Peng**[4,9,11] · **Alexey A. Petrov**[15] · **Yuan-Shuai Qin**[3] · **Ming-Chen Sun**[1,2] · **Jian Tang**[1,2] · **Jing-Yu Tang**[16] · **Ye Tian**[3] · **Rong Wang**[3,4] · **Xiao-Dong Wang**[17,18] · **Yi Wang**[13] · **Zhi-Chao Wang**[1,2] · **Chen Wu**[9,10] · **Tian-Yu Xing**[19,20] · **Wei-Zhi Xiong**[21] · **Yu Xu**[22] · **Bao-Jun Yan**[9,11] · **De-Liang Yao**[5,8] · **Tao Yu**[1,2] · **Ye Yuan**[4,9] · **Yi Yuan**[1,2] · **Yao Zhang**[9] · **Yongchao Zhang**[12] · **Zhi-Lv Zhang**[3] · **Guang Zhao**[9] · **Shi-Han Zhao**[1,2]

Received: 24 January 2025 / Revised: 12 June 2025 / Accepted: 5 July 2025 / Published online: 28 January 2026
© The Author(s), under exclusive licence to China Science Publishing & Media Ltd. (Science Press), Shanghai Institute of Applied Physics, the Chinese Academy of Sciences, Chinese Nuclear Society 2026

Abstract
The spontaneous conversion of muonium to antimuonium is an interesting charged lepton flavor violation phenomenon that offers a sensitive probe for potential new physics and serves as a tool to constrain the parameter space beyond the Standard Model. The Muonium-to-Antimuonium Conversion Experiment (MACE) was designed to utilize a high-intensity muon beam, a Michel electron magnetic spectrometer, a positron transport system, and a positron detection system to either discover or constrain this rare process with a conversion probability of $\mathcal{O}(10^{-13})$. This article presents an overview of the theoretical framework and a detailed description of the experimental design for muonium-to-antimuonium conversion.

Keywords Muonium · Lepton flavor violation · Muon beam · Drift chamber · Microchannel plate · Electromagnetic calorimeter

1 Introduction

Neutrino oscillation is a neutral lepton flavor violation process with profound implications for particle physics. On one hand, it points out that neutrinos have mass, and it is therefore the first direct evidence of physics beyond the standard model (BSM). The existence of a neutral lepton flavor violation also leads to the question of whether there is a charged lepton flavor violation (cLFV). However, the origin of neutrino masses remains an unsolved mystery in particle physics. The traditional way to explain neutrino masses is the seesaw mechanism, which is often predicted in conjunction with cLFV effects [1]. For example, in the type-II seesaw model, a Higgs triplet is introduced under $SU(2)$ symmetry. After spontaneous symmetry breaking, the massive Higgs boson can contribute to cLFV processes. Therefore, searching for cLFV is an important task in BSM physics. This is well motivated to push forward experimental efforts to look for BSM physics using cLFV processes.

This project was supported by National Natural Science Foundation of China (Nos. 12075326, 11535014, 11975017, 12475191, 11905092, 12105132 and 12175039), Guangdong Basic and Applied Basic Research Foundation (No. 2025A1515010669), Natural Science Foundation of Guangzhou (No. 2024A04J6243), Fundamental Research Funds for the Central Universities (23xkjc017) in Sun Yat-sen University, Basic Research Conditions and Major Scientific Instrument and Equipment Research and Development Projects of the Ministry of Science and Technology (No. 2022YFF0705602), the State Key Laboratory of Particle Detection and Electronics (SKLPDE-ZZ-202412), Natural Science Foundation of Shandong Province (No. 2023HWYQ-010), the "Fundamental Research Funds for the Central Universities" at Southeast University, the National Development and Reform Commission of China (Large Research Infrastructures of 12th Five-Year Plan: China initiative Accelerator Driven System) (No. 2017-000052-75-01-000590), and Innovation Training Program for bachelor students in Sun Yat-sen University.

Extended author information available on the last page of the article

Many experimental efforts have been made to search for a cLFV. Muon-electron-sector cLFV experiments such as COMET [2] in Japan and Mu2e [3] in the USA are currently under construction to search for coherent muon-to-electron conversion $\mu^- N \to e^- N$. The accelerator muon beam experiments at the Paul Scherrer Institute (PSI) are also searching for cLFV processes, with Mu3e [4] for $\mu^+ \to e^+e^-e^+$ and MEG II [5] for $\mu^+ \to e^+\gamma$.

Muonium is an atom consisting of a muon and an electron and was first discovered by Vernon W. Hughes et al. in 1960 [6]. Another interesting approach to probe BSM physics via cLFV is to consider the muonium atom and determine whether there is a spontaneous conversion from muonium to antimuonium. The original concept was first introduced by Pontecorvo in 1957 [7]. The latest upper limit on the muonium-to-antimuonium conversion probability, established at $P \lesssim 8.3 \times 10^{-11}$ at a 90% confidence level, was reported in a MACS experiment at PSI in 1999 [8]. This result has remained unchallenged in any experiment over the past two decades. The Muonium-to-Antimuonium Conversion Experiment (MACE) aims to discover or further constrain this rare process at an unprecedented level.

In the $\Delta L_\ell = 2$ process, the muonium-to-antimuonium conversion is distinct from $\Delta L_\ell = 1$ charged lepton flavor violation (cLFV) processes, such as $\mu^+ \to e^+\gamma$, $\mu^+ \to e^+e^-e^+$, and $\mu^- N \to e^- N$. From the perspective of the Standard Model effective field theory (SMEFT) [9–12], effective operators that generate $\Delta L_\ell = 1$ processes cannot directly account for $\Delta L_\ell = 2$ cLFV phenomena. Consequently, the sensitivity of these processes to $\Delta L_\ell = 2$ operators is significantly reduced, indicating that, even if $\Delta L_\ell = 1$ cLFV processes are observed, they give little rise to $\Delta L_\ell = 2$ operators. Furthermore, $\Delta L_\ell = 2$ operators can be fundamentally distinct from $\Delta L_\ell = 1$ operators, because they carry different lepton numbers. It is feasible to impose symmetry in the charged-lepton sector that forbids $\Delta L_\ell = 1$ processes while permitting $\Delta L_\ell = 2$ [13]. This suggests that $\Delta L_\ell = 1$ processes may not fundamentally exist. Therefore, searches targeting $\Delta L_\ell = 2$ processes can investigate phenomena inaccessible to $\Delta L_\ell = 1$ processes. As a result, muonium-to-antimuonium conversion is decorrelated from $\Delta L_\ell = 1$ processes, making it a promising target for experimental research.

Specific theoretical models, including neutral or doubly charged Higgs bosons in a type-II hybrid seesaw [14, 15], axion-like particles (ALPs) [16], and flavored gauge bosons, such as Z' [17–20], predict muonium-to-antimuonium conversion at the tree level. Additionally, heavy neutral leptons such as Majorana neutrinos can induce this conversion at the one-loop level [21–24]. A comprehensive theoretical study provided a complete list of models that allow for this conversion process [25]. In many of these models, searches for muonium-to-antimuonium conversion can complement high-energy collider experiments as well as other low-energy experiments, such as muon $g-2$. In addition to these experimental efforts, we can further constrain these models and reveal the mystery of many BSM phenomena, including neutrino masses, matter–antimatter asymmetry, and dark matter.

In addition to the M-to-$\overline{\mathrm{M}}$ conversion process, flavor-violating muonium decay is also of interest. In 1959, C.M. York et al. measured the upper limit of the reaction rate for muon-electron annihilation ($\mu^+e^- \to \gamma\gamma$) in a Cu target [26]. Since then, no analogous experimental results have been reported. In addition, other muonium cLFV decays, such as pair-final-state decay ($\mathrm{M} \to e^+e^-$) and invisible decay ($\mathrm{M} \to$ invisible), have not yet been experimentally constrained. A search for these rare muonium decay modes will complement other existing muon cLFV experiments to provide more evidence for possible new physics [27–34]. The current upper limits of similar processes, such as $\mu^+ \to e^+\gamma\gamma$ ($\mathcal{BR} < 7.2 \times 10^{-11}$) and $\mu^+ \to e^+e^-e^+$ ($\mathcal{BR} < 1.0 \times 10^{-12}$), have been reported by Crystal Box [35] and SINDRUM [36]. The Mu3e experiment was proposed to constrain the limit of the latter process to the level of 10^{-16} [4]. However, no experimental search plan for $\mu^+ \to e^+\gamma\gamma$ has been reported since the 1980s.

The advent of new intense and slow muon sources and significant advances in modern particle detection technologies will lead to new possibilities in the design of new lepton flavor violation experiments. Regarding muonium-to-antimuonium conversion, we intend to improve the present bound by more than two orders of magnitude in the proposed Muonium-to-Antimuonium Conversion Experiment (MACE). For the barely touched process $\mathrm{M} \to \gamma\gamma$, a sensitivity of $\mathcal{O}(10^{-12})$ was pursued in the pilot MACE PHASE-I experiment. The limit of $\mu^+ \to e^+\gamma\gamma$ is also expected to improve by one order of magnitude in this experimental stage. The experimental plan of searching for the aforementioned processes by optimizing the detector system and changing the event selection criteria is also discussed at the end of this article.

The conceptual design study focuses on the following aspects: physics motivation, development of a high-intensity muon beam, high-efficiency muonium production in a vacuum, optimized design of the detector system, and requirements for physical performance. This article summarizes the theoretical and experimental aspects of MACE.

2 Overview of theoretical framework

The main decay channel for muonium is determined by the weak decay of the muon $\mathrm{M} \to e^+e^-\bar{\nu}_\mu\nu_e$. The average lifetime of a muonium state τ_M is expected to be almost the same as that of the muon,

$$\begin{aligned}1/\tau_{\mathrm{M}} &= \Gamma\left(\mathrm{M} \to \mathrm{e}^+\mathrm{e}^-\nu_{\mathrm{e}}\bar{\nu}_{\mu}\right)\\ &\approx \Gamma\left(\mu^+ \to \mathrm{e}^+\nu_{\mathrm{e}}\bar{\nu}_{\mu}\right) = \frac{G_{\mathrm{F}}^2 m_{\mu}^5}{192\pi^3} = 1/\tau_{\mu},\end{aligned} \tag{1}$$

with $\tau_{\mu} = (2.1969811 \pm 0.0000022) \times 10^{-6}$ s [37], in addition to the small effect due to time dilation [29]. Note that Eq. (1) represents the leading order result. The results, including the subleading corrections, are available [29].

Similar to hydrogen atoms, muonium can be formed in two spin configurations. A spin-one triplet state $|\mathrm{M}^{\mathrm{V}}\rangle$ is called an ortho-muonium, whereas the spin-zero singlet state $|\mathrm{M}^{\mathrm{P}}\rangle$ is called a para-muonium. In what follows, we drop the superscript and employ the notation $|\mathrm{M}\rangle$ if the spin of the muonium state is not important for the discussion.

Because interactions with $\Delta L_{\ell} = 2$ can change the muonium state into the antimuonium state, the possibility of studying muonium-antimuonium oscillations arises. Theoretical analyses of the conversion probability from muonium to antimuonium have been performed, particularly in new physics models [7, 38–42], and using the framework of effective field theory [10], where all possible BSM models are encoded in a few Wilson coefficients of effective operators. The observation of muonium conversion into anti-muonium provides clean probes for new physics in the leptonic sector [8, 43].

2.1 Phenomenology of muonium conversion

To determine the experimental observables related to $\mathrm{M} - \overline{\mathrm{M}}$ oscillations, we recall that the treatment of the two-level system that represents muonium and antimuonium is similar to that of meson-antimeson oscillations [44–51]. However, there are several important differences. First, both the ortho- and para-muonium oscillate. Second, the SM oscillation probability is small, as it is related to the function of the neutrino masses. Any experimental indication of oscillation represents a sign of new physics.

In the presence of the interactions coupling M and $\overline{\mathrm{M}}$, the time development of a muonium and anti-muonium states would be coupled, so it would be appropriate to consider their combined evolution,

$$|\psi(t)\rangle = \begin{pmatrix} a(t) \\ b(t) \end{pmatrix} = a(t)|\mathrm{M}\rangle + b(t)|\overline{\mathrm{M}}\rangle. \tag{2}$$

The time evolution of $|\psi(t)\rangle$ evolution is governed by a Schrödinger-like equation,

$$i\frac{\mathrm{d}}{\mathrm{d}t}\begin{pmatrix} |\mathrm{M}(t)\rangle \\ |\overline{\mathrm{M}}(t)\rangle \end{pmatrix} = \left(M - i\frac{\Gamma}{2}\right)\begin{pmatrix} |\mathrm{M}(t)\rangle \\ |\overline{\mathrm{M}}(t)\rangle \end{pmatrix}, \tag{3}$$

where $\left(M - i\frac{\Gamma}{2}\right)_{ik}$ is a 2×2 Hamiltonian (mass matrix) with nonzero off-diagonal terms originating from the $\Delta L_{\ell} = 2$ interactions. CPT invariance dictates that the masses and widths of the muonium and anti-muonium are the same, and thus, $M_{11} = M_{22}, \Gamma_{11} = \Gamma_{22}$. In what follows, we assume CP invariance of the $\Delta L_{\ell} = 2$ interaction. A more general formalism without this assumption follows the same steps as those for B-$\bar{\mathrm{B}}$ or K-$\bar{\mathrm{K}}$ mixing [49, 50]. Then,

$$M_{12} = M_{21}^*, \qquad \Gamma_{12} = \Gamma_{21}^*. \tag{4}$$

The off-diagonal matrix elements in Sect. 2.1 are related to the matrix elements of the effective operators, as discussed in [49, 50]. The related Lagrangian expressed in the effective operators can be found in Sect. 2.2.

$$\begin{aligned}\left(M - \frac{i}{2}\Gamma\right)_{12} &= \frac{1}{2m}\left\langle\overline{\mathrm{M}}\middle|\mathcal{H}_{\mathrm{eff}}\middle|\mathrm{M}\right\rangle\\ &+ \frac{1}{2m}\sum_n \frac{\left\langle\overline{\mathrm{M}}\middle|\mathcal{H}_{\mathrm{eff}}\middle|n\right\rangle\left\langle n\middle|\mathcal{H}_{\mathrm{eff}}\middle|\mathrm{M}\right\rangle}{m - E_n + i\epsilon},\end{aligned} \tag{5}$$

where $m = \left(m_1 + m_2\right)/2$ is the muonium mass and m_i are the masses of the physical mass eigenstates $|\mathrm{M}_{1,2}\rangle$ as discussed below.

To determine the propagating states, the mass matrix must be diagonalized. The basis in which the mass matrix is diagonal is represented by the mass eigenstates $|\mathrm{M}_{1,2}\rangle$, which are related to the flavor eigenstates M and $\overline{\mathrm{M}}$ as

$$|\mathrm{M}_{1,2}\rangle = \frac{1}{\sqrt{2}}\left(|\mathrm{M}\rangle \mp |\overline{\mathrm{M}}\rangle\right), \tag{6}$$

where we employed a convention where $CP|\mathrm{M}_{\pm}\rangle = \mp|\mathrm{M}_{\pm}\rangle$. The mass and the width differences of the mass eigenstates are

$$\Delta m \equiv m_1 - m_2, \quad \Delta\Gamma \equiv \Gamma_2 - \Gamma_1, \tag{7}$$

where, m_i (Γ_i) is the mass (width) of the physical mass eigenstates $|\mathrm{M}_{1,2}\rangle$. It is interesting to see how Eq. (5) defines mass and lifetime differences. Because the first term in Eq. (5) is defined by a local operator, its matrix element does not develop an absorptive part, thus contributing to M_{12}, that is, the mass difference. The second term contains the bi-local contributions connected by physical intermediate states. This term has both real and imaginary parts and thus contributes to both M_{12} and Γ_{12}.

It is often convenient to introduce dimensionless quantities,

$$x = \frac{\Delta m}{\Gamma}, \qquad y = \frac{\Delta\Gamma}{2\Gamma}, \tag{8}$$

where the average width $\Gamma = (\Gamma_1 + \Gamma_2)/2$. Note that Γ is defined by the standard model decay rate of the muon, and x and y are driven by the lepton-flavor violating interactions; we should expect that both $x, y \ll 1$.

The time evolution of flavor eigenstates follows from Eq.(3) [10, 48, 49],

$$\begin{aligned}|\mathrm{M}(t)\rangle &= g_+(t)|\mathrm{M}\rangle + g_-(t)|\overline{\mathrm{M}}\rangle,\\ |\overline{\mathrm{M}}(t)\rangle &= g_-(t)|\mathrm{M}\rangle + g_+(t)|\overline{\mathrm{M}}\rangle,\end{aligned} \tag{9}$$

where the coefficients $g_\pm(t)$ are defined as

$$g_\pm(t) = \frac{1}{2}e^{-\Gamma_1 t/2}e^{-im_1 t}\left(1 \pm e^{\Delta\Gamma t/2}e^{i\Delta m t}\right). \tag{10}$$

As $x, y \ll 1$ we can expand Eq.(10) in power series in x and y to obtain

$$\begin{aligned}g_+(t) &= e^{-\Gamma_1 t/2}e^{-im_1 t}\left(1 + \frac{1}{8}(y - ix)^2(\Gamma t)^2\right),\\ g_-(t) &= \frac{1}{2}e^{-\Gamma_1 t/2}e^{-im_1 t}(y - ix)(\Gamma t).\end{aligned} \tag{11}$$

The most natural way to detect $\mathrm{M} - \overline{\mathrm{M}}$ oscillations experimentally is to produce M state and look for the decay products of the CP-conjugated state $\overline{\mathrm{M}}$. Denoting an amplitude for the M decay into a final state 'f' as $A_\mathrm{f} = \langle \mathrm{f}|\mathcal{H}|\mathrm{M}\rangle$ and an amplitude for its decay into a CP-conjugated final state $\bar{\mathrm{f}}$ as $A_{\bar{\mathrm{f}}} = \langle \bar{\mathrm{f}}|\mathcal{H}|\mathrm{M}\rangle$, we can write the time-dependent decay rate of M into the $\bar{\mathrm{f}}$,

$$\Gamma(\mathrm{M} \to \bar{\mathrm{f}})(t) = \frac{1}{2}N_\mathrm{f}\left|A_\mathrm{f}\right|^2 e^{-\Gamma t}(\Gamma t)^2 R_\mathrm{M}(x, y), \tag{12}$$

where N_f is a phase-space factor and we defined the oscillation rate $R_\mathrm{M}(x, y)$ as

$$R_\mathrm{M}(x, y) = \frac{1}{2}\left(x^2 + y^2\right). \tag{13}$$

Integrating over time and normalizing to $\Gamma(\mathrm{M} \to \mathrm{f})$ we get the probability of M decaying as $\overline{\mathrm{M}}$ at some time $t > 0$,

$$P(\mathrm{M} \to \overline{\mathrm{M}}) = \frac{\Gamma(\mathrm{M} \to \bar{\mathrm{f}})}{\Gamma(\mathrm{M} \to \mathrm{f})} = R_\mathrm{M}(x, y). \tag{14}$$

Equation(14) generalizes the oscillation probability found in previous studies [10, 38, 40] by allowing for a nonzero lifetime difference in $\mathrm{M} - \overline{\mathrm{M}}$ oscillations.

2.2 Muonium conversion and new physics beyond the standard model

The Standard Model Effective Field Theory (SMEFT) serves as a powerful framework for providing a model-independent characterization of new physics beyond the Standard Model [9, 12]. If we believe that the Standard Model acts as a low-energy approximation of a complete theory, the Standard Model Lagrangian can be interpreted as the leading term in a series expansion of the complete theory. Higher-order terms in this series expansion are effective forms of new physics, beyond the Standard Model. The Standard Model operators have a mass dimension of four, whereas higher-dimensional operators, which are scaled by inverse powers of the unknown new physics scale (NP scale), are incorporated into the SMEFT Lagrangian. Thus, the SMEFT Lagrangian can be expressed as a series expansion in terms of the inverse power of NP scale,

$$\begin{aligned}\mathcal{L}_\mathrm{eff} &= \mathcal{L}_\mathrm{SM} + \sum_{n>4}\frac{1}{\Lambda^{n-4}}\sum_i C_i^{(n)}Q_i^{(n)}\\ &= \mathcal{L}_\mathrm{SM} + \frac{1}{\Lambda}\sum_i C_i^{(5)}Q_i^{(5)} + \frac{1}{\Lambda^2}\sum_i C_i^{(6)}Q_i^{(6)} + \cdots.\end{aligned} \tag{15}$$

The leading term in the series is the Standard Model Lagrangian denoted as $\mathcal{L}_\mathrm{SM}$. In higher-order terms, each dimension-n effective operator $Q_i^{(n)}$ is associated with a Wilson coefficient $C_i^{(n)}$ and scaled by the new physics scale Λ. Qualitatively, these higher-order terms encapsulate the potential new physics models through effective operators, whereas the Wilson coefficients represent the coupling strengths. The new physics scale Λ can be interpreted as a characteristic energy scale in the new physics, such as a combination of quantities with dimensions of mass involved in interactions beyond the Standard Model. Both the NP scale and Wilson coefficients will ultimately manifest in observables, allowing experiments to constrain the new physics scale or coupling strengths in a model-independent manner.

Dimension-6 operators are the lowest-order operators, where $\Delta L_\mu = 2$ muonium-to-antimuonium conversion and other cLFV processes can be introduced at the tree level using a single SMEFT vertex [10, 52–54]. There are five independent dimension-6 $\bar{\mu}e\bar{\mu}e$ four-fermion operators that leads to muonium-to-antimuonium conversion [10, 11, 25, 34],

$$\begin{aligned}Q_\mathrm{V}^\mathrm{LL} &= \left(\bar{\mu}\gamma_\alpha(1-\gamma_5)e\right)\left(\bar{\mu}\gamma^\alpha(1-\gamma_5)e\right),\\ Q_\mathrm{V}^\mathrm{RR} &= \left(\bar{\mu}\gamma_\alpha(1+\gamma_5)e\right)\left(\bar{\mu}\gamma^\alpha(1+\gamma_5)e\right),\\ Q_\mathrm{V}^\mathrm{LR} &= \left(\bar{\mu}\gamma_\alpha(1-\gamma_5)e\right)\left(\bar{\mu}\gamma^\alpha(1+\gamma_5)e\right),\\ Q_\mathrm{S}^\mathrm{LR} &= \left(\bar{\mu}(1+\gamma_5)e\right)\left(\bar{\mu}(1+\gamma_5)e\right),\\ Q_\mathrm{S}^\mathrm{RL} &= \left(\bar{\mu}(1-\gamma_5)e\right)\left(\bar{\mu}(1-\gamma_5)e\right).\end{aligned} \tag{16}$$

These five operators contribute to the mass difference, as defined in Sect. 2.1. The width difference can arise from the following $\bar{\mu}e\bar{\nu}_\mu\nu_\mathrm{e}$ four-fermion operators,

$$\begin{aligned}Q_\mathrm{V}^{\mathrm{L}\nu} &= \left(\bar{\mu}\gamma_\alpha(1-\gamma_5)e\right)\left(\bar{\nu}_\mu\gamma^\alpha(1-\gamma_5)\nu_\mathrm{e}\right),\\ Q_\mathrm{V}^{\mathrm{R}\nu} &= \left(\bar{\mu}\gamma_\alpha(1+\gamma_5)e\right)\left(\bar{\nu}_\mu\gamma^\alpha(1-\gamma_5)\nu_\mathrm{e}\right).\end{aligned} \tag{17}$$

However, the contribution of the width difference to the conversion probability is suppressed by a factor of $G_\mathrm{F}m^2 \approx 10^{-7}$ [10, 34], which is orders of magnitude smaller than the contributions from the mass difference as long as $|C_\mathrm{V}^{\mathrm{L}\nu}/C_\mathrm{other}|$ and $|C_\mathrm{V}^{\mathrm{R}\nu}/C_\mathrm{other}|$ are not too large. Therefore, we only considered the mass difference contributions in the following calculations.

The effective Lagrangian for muonium-to-antimuonium conversion can be written as

$$\begin{aligned}\mathcal{L}_{\text{eff}} = \frac{1}{\Lambda^2}\big(&C_{\text{V}}^{\text{LL}} Q_{\text{V}}^{\text{LL}} + C_{\text{V}}^{\text{RR}} Q_{\text{V}}^{\text{RR}} + C_{\text{V}}^{\text{LR}} Q_{\text{V}}^{\text{LR}} + \\ &C_{\text{S}}^{\text{LR}} Q_{\text{S}}^{\text{LR}} + C_{\text{S}}^{\text{RL}} Q_{\text{S}}^{\text{RL}}\big) \,.\end{aligned} \tag{18}$$

The corresponding effective Hamiltonian in Eq.(5) is $\mathcal{H}_{\text{eff}} = -\mathcal{L}_{\text{eff}}$, which generates a muonium-to-antimuonium conversion, as shown in Fig. 1 [55].

According to the SMEFT Lagrangian, we calculated the amplitudes for muonium-to-antimuonium conversion. In the experiments, muonium atoms were produced in two spin states: spin-zero singlet states (para-muonium, denoted as M_{P}) and spin-one triplet states (ortho-muonium, denoted as $\text{M}_{\text{V},m}$, where $m = 0, \pm 1$). The conversion probability is expressed in terms of dimensionless mass differences, that is, x in Sect. 2.1, under the assumption that the width differences are negligible. Each spin state has its own corresponding value of x. They are given by [25, 56]

$$\begin{aligned} x_{\text{P}} &= \frac{16(\alpha\mu)^3}{\pi\Gamma\Lambda^2}\left(C_0 - \frac{3}{2}C_{\text{V}}^{\text{LR}}\right) , \\ x_{\text{V},0} = x_{\text{V},\pm 1} &= \frac{16(\alpha\mu)^3}{\pi\Gamma\Lambda^2}\left(C_0 + \frac{1}{2}C_{\text{V}}^{\text{LR}}\right), \end{aligned} \tag{19}$$

where

$$C_0 = C_{\text{V}}^{\text{LL}} + C_{\text{V}}^{\text{RR}} - \frac{1}{4}\left(C_{\text{S}}^{\text{LR}} + C_{\text{S}}^{\text{RL}}\right) . \tag{20}$$

Here, $\mu = m_{\mu} m_{\text{e}}/(m_{\mu} + m_{\text{e}})$ is the reduced mass of muonium, α is the fine-structure constant, and Γ is the muonium width.

It is important to note that a non-zero external magnetic field will suppress the conversion probability [25, 56–58]. Since the decay kinematics of different spin states are indistinguishable in experiments like MACE, the total conversion probability is expressed as a weighted sum over all spin states, according to their populations,

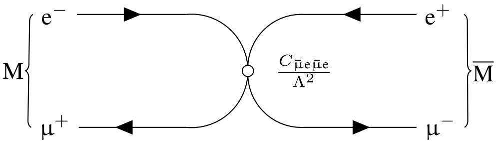

Fig. 1 The SMEFT tree-level diagram for muonium-to-antimuonium conversion with one $\Delta L_{\mu} = 2$ four-fermion effective vertex. The conversion probability is proportional to $1/\Lambda^4$

$$\begin{aligned} P_B(\text{M} \to \overline{\text{M}}) = & f_{\text{P}} P_B(\text{M}_{\text{P}} \to \overline{\text{M}}_{\text{P}}) \\ & + f_{\text{V},0} P_B(\text{M}_{\text{V},0} \to \overline{\text{M}}_{\text{V},0}) \\ & + \sum_{m=\pm 1} f_{\text{V},m} P_B(\text{M}_{\text{V},m} \to \overline{\text{M}}_{\text{V},m}) \,, \end{aligned} \tag{21}$$

where f_{P} and $f_{\text{V},m}$ denote the populations of para- and ortho-muonium states, respectively. P_B denotes the conversion probability in an external magnetic field of magnitude B.

The conversion probabilities for different spin states exhibit distinct magnetic-field dependencies. For the $m = \pm 1$ ortho-muonium states, the external magnetic field induces an energy splitting ΔE_B, which suppresses their conversion probability

$$P_B(\text{M}_{\text{V},\pm 1} \to \overline{\text{M}}_{\text{V},\pm 1}) = \frac{x_{\text{V},\pm 1}^2/2}{1 + \left(\Delta E_B/\Gamma\right)^2} \,, \tag{22}$$

where $\Delta E_B/\Gamma \approx 3.85 \times 10^5 \times B/[\text{T}]$ [25]. The $(\Delta E_B/\Gamma)^2$ term suppresses the conversion probability by $\mathcal{O}(10^{-9})$ in a 0.1 T magnetic field. Consequently, contributions from the $m = \pm 1$ states are quenched in the MACE.

In contrast, $m = 0$ states are free from energy splitting, so the conversion probabilities are still sizeable in a practical external magnetic field. Instead, the $m = 0$ para- and ortho-muonium states are mixed due to the magnetic field, and the dimensionless mass differences are written as

$$\begin{aligned} x_{\text{P}}^B &= \frac{1}{2}\left(x_{\text{P}} - x_{\text{V},0} + \frac{x_{\text{P}} + x_{\text{V},0}}{\sqrt{1 + X^2}}\right) , \\ x_{\text{V},0}^B &= \frac{1}{2}\left(x_{\text{V},0} - x_{\text{P}} + \frac{x_{\text{P}} + x_{\text{V},0}}{\sqrt{1 + X^2}}\right) , \end{aligned} \tag{23}$$

where $X \approx 6.31 \times B/[\text{T}]$ [25]. Here, x_{P}^B and $x_{\text{V},0}^B$ represent the dimensionless mass differences in an external magnetic field of magnitude B.

The total magnetic-field-dependent conversion probability reads

$$\begin{aligned} P_B(\text{M} \to \overline{\text{M}}) = \frac{1}{2}\Bigg(& f_{\text{P}}\left(x_{\text{P}}^B\right)^2 + f_{\text{V},0}\left(x_{\text{V},0}^B\right)^2 \\ & + \sum_{m=\pm 1} \frac{f_{\text{V},m} x_{\text{V},\pm 1}^2}{1 + \left(\Delta E_B/\Gamma\right)^2}\Bigg). \end{aligned} \tag{24}$$

If there exists some sizable magnetic field (typically larger than the geomagnetic field) and contributions from $m = \pm 1$ states are negligible as in MACE's case, the total conversion probability can be simplified as

$$P_B(\text{M} \to \overline{\text{M}}) = \frac{1}{2}\left(f_{\text{P}}\left(x_{\text{P}}^B\right)^2 + f_{\text{V},0}\left(x_{\text{V},0}^B\right)^2\right) . \tag{25}$$

We can now estimate the new physics scale that MACE can probe in a $B = 0.1\,\mathrm{T}$ magnetic field by assuming $f_\mathrm{P} = 0.32$, $f_{\mathrm{V},0} = 0.18$, and taking all Wilson coefficients to be 1. This leads to the result

$$\Lambda \gtrsim \frac{0.02\ \mathrm{TeV}}{P^{\mathrm{up}}_{0.1\,\mathrm{T}}(\mathrm{M} \to \overline{\mathrm{M}})^{1/4}}\,. \tag{26}$$

If the experimental upper limit $P^{\mathrm{up}}_{0.1\,\mathrm{T}}(\mathrm{M} \to \overline{\mathrm{M}})$ is set to $\mathcal{O}(10^{-13})$, we conclude that MACE can probe new physics at a scale of 10–100 TeV.

Since $\Delta L_\ell = 1$ processes are distinct from $\Delta L_\ell = 2$ physics and they are not directly comparable to muonium-to-antimuonium conversion, it is essential to figure out which processes are sensitive to $\Delta L_\ell = 2$ physics. They should involve fermions from two different generations and violate the lepton flavor in two units. An incomplete list of candidate processes for the experimental searches is provided in Table 1. The current most stringent limit is set by the MACS experiment [8], whereas most of the other processes remain unconstrained. These unconstrained processes will likely be targeted for experimental searches or measurements in the coming decades.

The muonium-to-antimuonium conversion generating $\bar{\mu}e\bar{\mu}e$ four-fermion operators can also lead to cLFV scattering processes $\mu^+e^- \to \mu^-e^+$ and $\mu^+\mu^+ \to \ell^+\ell^+$ ($\ell = \mathrm{e}, \tau$), which can be investigated in future lepton colliders. Recently, a muon collider called μTRISTAN was proposed [52]. The conceptual design utilizes an intensive muonium source produced from a multi-layer silica aerogel target to provide an ultra-cold muon source by ionizing muonium atoms. A collider-quality muon beam was produced by reaccelerating ultra-cold muons. The center-of-mass energies for μ^+e^- and $\mu^+\mu^+$ collisions are 346 GeV and 2 TeV, respectively, with estimated instantaneous luminosities of $5.7 \times 10^{32}\ \mathrm{cm}^{-2}\,\mathrm{s}^{-1}$ and $4.6 \times 10^{33}\ \mathrm{cm}^{-2}\,\mathrm{s}^{-1}$. This high luminosity gives μTRISTAN the potential to provide stringent bounds for these two cLFV scattering processes. Based on previous phenomenological calculations on similar four-fermion operators, μTRISTAN can potentially push the new physics scale limit on $\bar{\mu}e\bar{\mu}e$ four-fermion operators up to 50 TeV [59]. Substantial efforts are still required before the μ^+e^- and $\mu^+\mu^+$ colliders can be operational and accessible to physicists.

The MUonE experiment is a fixed-target experiment aimed at measuring the $\mu - e$ scattering differential cross section with unprecedented precision of $\mathcal{O}(10^{-5})$ [60]. MUonE is designed to utilize the intense 150 GeV muon beam available at CERN, incident on beryllium targets, to measure the scattering of muons on atomic electrons. The design aims to achieve the target statistical sensitivity within three years of running time with an integrated luminosity of $15\ \mathrm{fb}^{-1}$. The limit on the $\mu^+e^- \to \mu^-e^+$ cross section can be set by measuring anomalies in the $\mu - e$ scattering cross section. Unfortunately, this approach may not be sufficiently sensitive to heavy new physics to supersede the existing MACS limit owing to the low center-of-mass energy [61, 62].

The process $\mu^+e^- \to \mu^-e^+$ (Fig. 2) is generated from pure four-fermion effective couplings, and its Lagrangian is the same as that of muonium-to-antimuonium conversion. Neglecting lepton masses, the differential cross section for the process $\mu^+e^- \to \mu^-e^+$ is given by

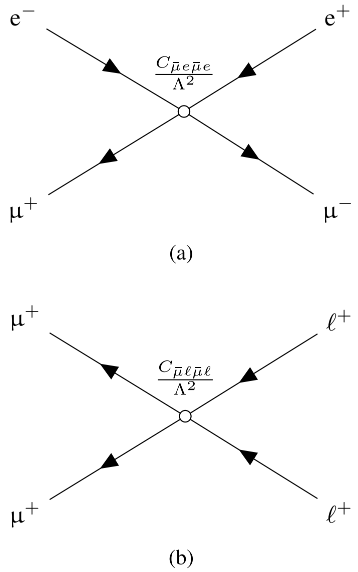

Fig. 2 Charged lepton flavor violating scattering $\mu^+e^- \to \mu^-e^+$ (a) and $\mu^+\mu^+ \to \ell^+\ell^+$ ($\ell = \mathrm{e}, \tau$) (b)

Table 1 $\Delta L_\ell = -\Delta L_{\ell'} = 2$ cLFV processes

Process	Type	Experiment	Current bound
$\mathrm{M} \to \overline{\mathrm{M}}$	$\mathrm{M} - \overline{\mathrm{M}}$ mixing	MACS [8], MACE	$P_{0.1\,\mathrm{T}}(\mathrm{M} \to \overline{\mathrm{M}}) < 8.3 \times 10^{-11}$ [8]
$\mu^+e^- \to \mu^-e^+$	Scattering	μTRISTAN [52]	None
$\mu^+\mu^+ \to e^+e^+$			
$\mu^+\mu^+ \to \tau^+\tau^+$			
$\mu^+ \to e^+\bar{\nu}_e\nu_\mu$	Decay	τ_μ measurement	$\Delta\tau_\mu/\tau_\mu = 1 \times 10^{-6}$ [37]
$Z \to \ell'^\pm\ell'^\pm\ell^\mp\ell^\mp$		CEPC [53], FCC-ee [54]	None

$$\frac{\mathrm{d}\sigma(\mu^+e^- \to \mu^-e^+)}{\mathrm{d}\Omega} = \frac{E_{\mathrm{CM}}^2}{64\pi^2\Lambda^4}\Big(c_0^2(1+\cos^2\theta) + c_1^2\cos\theta + c_2^2(1-\cos^2\theta)\Big), \tag{27}$$

where $E_{\mathrm{CM}} = \sqrt{s}$ is the center-of-mass energy and θ is the angle between the incoming electron and the outgoing muon. The coefficients c_0^2, c_1^2, and c_2^2 are defined as follows,

$$\begin{aligned} c_0^2 &= 4\bigg(\left|C_{\mathrm{V}}^{\mathrm{LL}}\right|^2 + \left|C_{\mathrm{V}}^{\mathrm{RR}}\right|^2 + 2\left|C_{\mathrm{V}}^{\mathrm{LR}}\right|^2 + \frac{1}{2}\left|C_{\mathrm{S}}^{\mathrm{LR}}\right|^2 + \frac{1}{2}\left|C_{\mathrm{S}}^{\mathrm{RL}}\right|^2\bigg), \\ c_1^2 &= 8\bigg(\left|C_{\mathrm{V}}^{\mathrm{LL}}\right|^2 + \left|C_{\mathrm{V}}^{\mathrm{RR}}\right|^2 - 2\left|C_{\mathrm{V}}^{\mathrm{LR}}\right|^2\bigg), \\ c_2^2 &= 2\bigg(\left|C_{\mathrm{S}}^{\mathrm{LR}}\right|^2 + \left|C_{\mathrm{S}}^{\mathrm{RL}}\right|^2\bigg). \end{aligned} \tag{28}$$

The form of the differential cross section is similar to that for $\ell\bar{\ell} \to \ell'\bar{\ell}''$, but without contributions from Z boson or photon couplings [63]. For the heavy new physics mediators considered here, a higher center-of-mass energy leads to a larger cross section and increased sensitivity to new physics. The new physics scale that can be probed by $\sqrt{s} = 346$ GeV μ^+e^- collisions with $16° < \theta_{\mathrm{lab}} < 164°$ in the lab frame is estimated as

$$\Lambda \gtrsim \frac{(0.25\ \mathrm{TeV})^{1/2}}{\sigma_{\mathrm{up}}(\mu^+e^- \to \mu^-e^+)^{1/4}}. \tag{29}$$

Assuming an integrated luminosity of 1 ab^{-1} [59], the μ^+e^- collider could probe new physics on the scale of 10–100 TeV. Operator-dependent new physics scales for the experiments are shown in Fig. 3, where the μTRISTAN result is projected from the background-free upper limit with a 90% confidence level (C.L.). We observed from this result that MACE, as a low-energy experiment, could probe a new physics scale comparable to or even higher than that of a future muon collider. This finding highlights the importance of low-energy experiments in the search for new TeV-scale physics.

3 M-to-$\overline{\mathrm{M}}$ conversion signals and backgrounds

Investigating and understanding signals and backgrounds is essential in experiments to search for new physics beyond the Standard Model. Backgrounds could affect the MACE sensitivity, and a deep understanding of

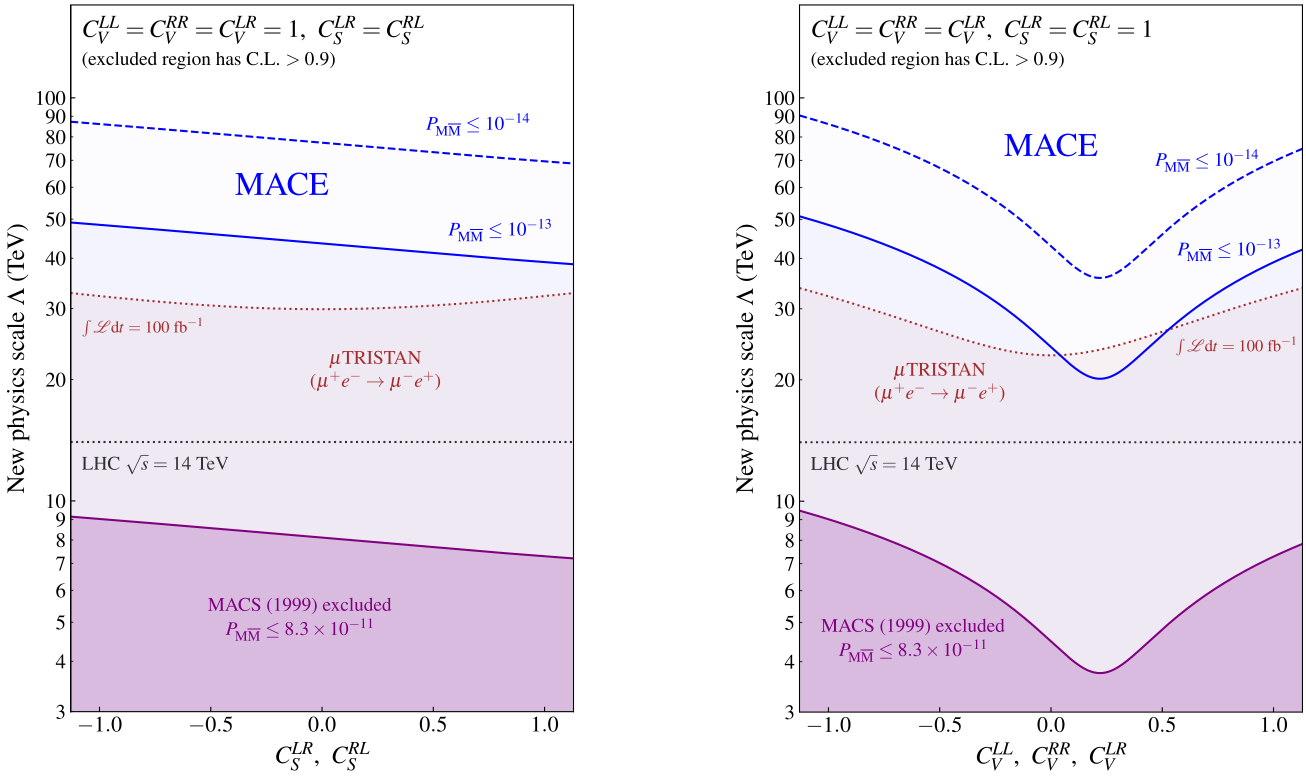

Fig. 3 (Color online) The new physics scale accessible to experiments searching for $\Delta L_\ell = 2$ processes

backgrounds allows for the optimization of experimental designs, data analysis, and signal selection methods, which can improve MACE sensitivity to new physics.

3.1 Signal event signature

MACE aims to search for the muonium-to-antimuonium conversion process by detecting antimuonium decay events in vacuum. The detection scheme is identified the characteristic decay products of antimuonium. Upon the decay of antimuonium, a fast electron, slow positron, and two invisible neutrinos are produced. The fast electron originates from the μ^- decay with a kinetic energy of a few tens of MeV, while the slow positron comes from the atomic shell with a mean kinetic energy of 13.5 eV (considering $1s$ antimuonium, as shown in Fig. 4). By detecting these two opposite decay products, a few antimuonium decay events can be identified from the vast number of muons and muonium decays.

The signal signature in detection is clear: a signal event involves an energetic electron and slow positron. The energy spectra of the signals are shown in Fig. 4. The MACE design employed a silica aerogel target that produced muonium by injecting a high-intensity surface muon beam. The target was designed to be porous and perforated to maximize the diffusion of muonium into vacuum. Following the spontaneous conversion of muonium to antimuonium in vacuum, antimuonium decays into an energetic electron and a slow positron. The energetic electron may traverse the charged particle tracker with a sufficient energy threshold, whereas the positron is guided by the positron transport system toward a position-sensitive detector. Subsequently, the positron may annihilate the detector, producing a pair of 511 keV gamma rays.

3.2 Backgrounds

As a signal event involves an energetic electron and a low-energy positron, any event with such a signature might be misidentified as a signal, making them potential backgrounds. First, the possible sources of the background must be identified. Backgrounds can be grouped into two categories: physical and accidental backgrounds. Physical backgrounds may arise from the decay of muons or muonium atoms, whereas accidental backgrounds could result from two tracks coincident from distinct sources. The following discussion focuses on these two types of backgrounds.

The primary focus of MACE is muonium, raising the important question of whether muonium itself can introduce a physical backgrounds. In a minimal extension of the Standard Model that simply extends right-handed neutrinos, the M-to-$\overline{\mathrm{M}}$ conversion probability will experience GIM-like suppression because of the tiny neutrino masses, similar to cLFV decays Fig. 5, such as $\mu \to \mathrm{e}\gamma$ [64, 65] or $\mu \to \mathrm{eee}$ [66, 67]. Consequently, the conversion probability is expected to be considerably low. Consequently, there is no irreducible physical backgrounds, and any background contribution is expected to originate from muon or muonium decay, as shown in Fig. 6.

MACE operates at an intensive muon beam; therefore, any muon-induced background should not be overlooked. The major decay mode $\mu^+ \to \mathrm{e}^+\nu_\mathrm{e}\bar{\nu}_\mu$ or the radiative decay mode $\mu^+ \to \mathrm{e}^+\nu_\mathrm{e}\bar{\nu}_\mu\gamma$ does not introduce extra electrons, and thus, they are generally safe. However, SM-allowed internal conversion (IC) decay $\mu^+ \to \mathrm{e}^+\mathrm{e}^-\mathrm{e}^+\nu_\mathrm{e}\bar{\nu}_\mu$ introduces an electron in its final state with a branching ratio of 3.4×10^{-5} (with a transverse momentum cut $p_\mathrm{T} > 17\ \mathrm{MeV}/c$) [68]. When the positron has a fairly low momentum and an electron is detected while another is not, the internal conversion decay $\mu^+ \to \mathrm{e}^+\mathrm{e}^-\mathrm{e}^+\nu_\mathrm{e}\bar{\nu}_\mu$ can fake signals. The background

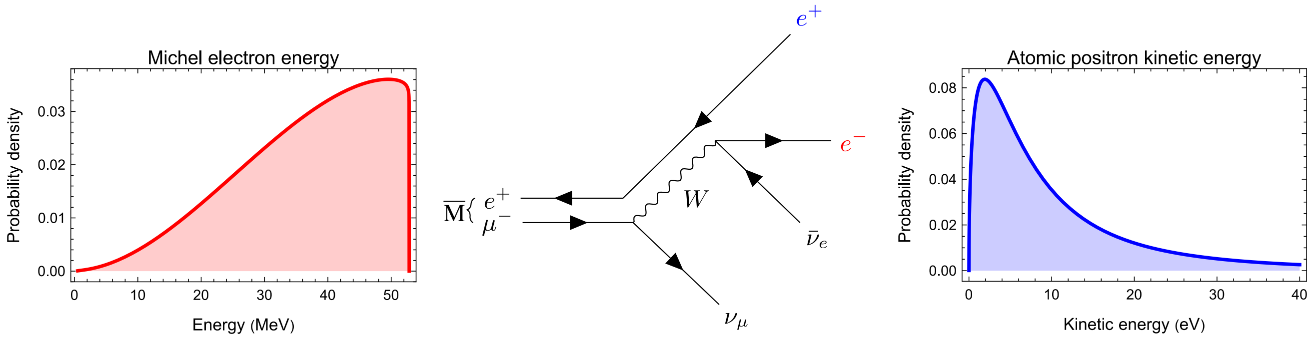

(a) (b) (c)

Fig. 4 (Color online) Energy spectrum and the leading-order diagram of antimuonium decay $\overline{\mathrm{M}} \to \mathrm{e}^+\mathrm{e}^-\bar{\nu}_\mathrm{e}\nu_\mu$. The energy spectrum of the fast decay e^- is accurate to next-to-leading-order, atomic shell e^+ spectrum assumes $1s$ muonium [62]. **a** e^- energy spectrum; **b** Leading-order $\overline{\mathrm{M}}$ decay; **c** e^+ energy spectrum

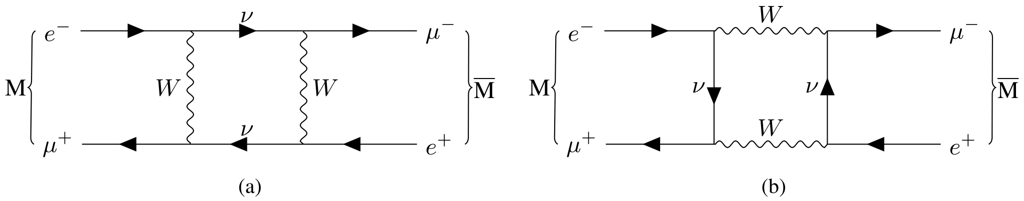

Fig. 5 Muonium conversion to antimuonium by the Standard Model weak interaction. This process is strongly suppressed by the tiny neutrino masses

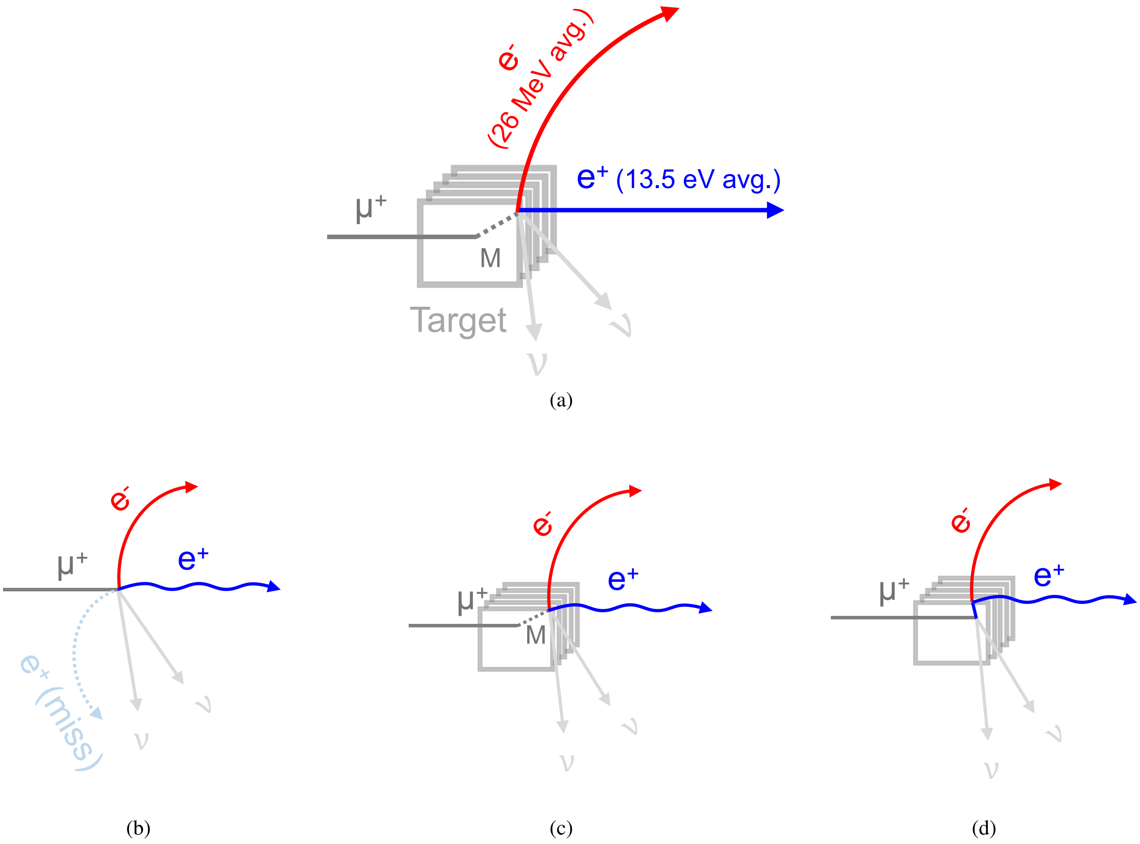

Fig. 6 Event topologies for signals and backgrounds. **a** M-to-$\overline{\text{M}}$ conversion signal; **b** Background: SM allow rare decay $\mu^+ \rightarrow e^+e^-e^+\nu_e\bar{\nu}_\mu$; **c** Background: muonium decay with Bhabha scattering; **d** Accidental backgrounds

event topology is shown in Fig. 6b and the energy spectra of the decay products are shown in Fig. 7. In fact, the internal conversion decay of muon was identified as one of the major background sources in the MACS experiment in PSI [8, 69]. To reduce this type of background, we can utilize the difference in kinematics between the antimuonium decay and muon IC decay.

As shown in the energy spectrum of the lowest positron energy (Fig. 7d), one can observe that the branching fraction decreased significantly at low energies. The signal positron typically has a kinetic energy of only a few tens of electronvolts, providing a strong discriminator between the signal and muon internal conversion decay background, as illustrated in Fig. 8. Selecting low-energy positrons and constraining their kinetic energy to be extremely low in the MACE detector system can effectively suppress the internal conversion decay background and improve the signal-to-background ratio. This approach requires the design of a transverse-momentum-selective positron transport solenoid system, as detailed in Sect. 8.1. However, the longitudinal momentum can be selected by the time-of-flight of the positron. Furthermore, the transverse momentum of the energetic

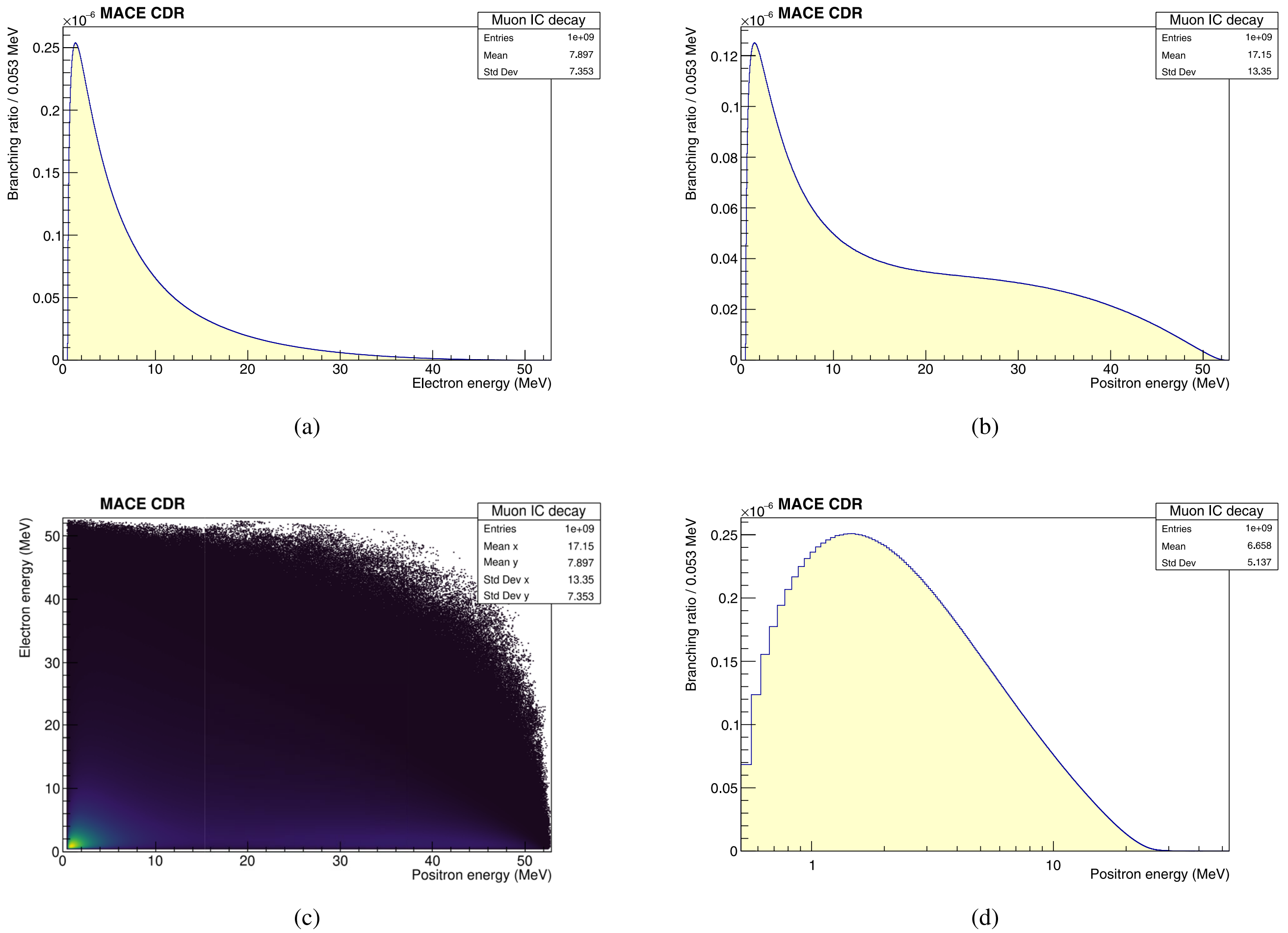

(a)

(b)

(c)

(d)

Fig. 7 (Color online) Spectra of muon internal conversion (IC) decay. **a** e^- energy spectrum of from μ^+ IC decay; **b** e^+ energy spectrum from μ^+ IC decay; **c** Joint energy spectrum of e^+/e^- from μ^+ IC decay; **d** Energy spectrum of e^+ with the lowest energy from μ^+ IC decay

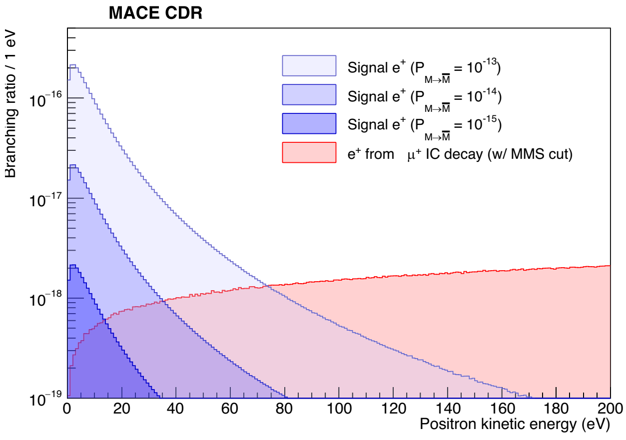

Fig. 8 (Color online) M-to-$\overline{\text{M}}$ signal e^+ kinetic energy spectrum of different conversion probability (blue) and background e^+ kinetic energy spectrum from $\mu^+ \to e^+e^-e^+\nu_e\bar{\nu}_\mu$ decay process (red)

electron from the same decay event is concentrated in the low momentum region, as shown in Fig. 9, in contrast to the signal electron spectrum shown in Fig. 4a. Therefore, selecting the transverse momentum of the energetic electron to be sufficient also aids in background suppression. With these signal purification strategies, the phase space of backgrounds can be strongly constrained while maintaining the majority of signals, eventually improving the signal-to-background ratio.

There is also a possibility that muonium decay could contribute to the physical background of MACE. Muonium shares most of its decay properties with muons, except for the presence of an atomic electron. When a Michel positron from muon decay interacts with an atomic electron and exchanges significant momentum, the muonium decay products behave as low-energy positrons and high-energy electrons, potentially leading to misidentification as antimuonium decay. The event topology is shown in Fig. 6c. This type of background was discussed in a previous theoretical study [38], and the branching ratio with $E_{e^-} > 10$ MeV

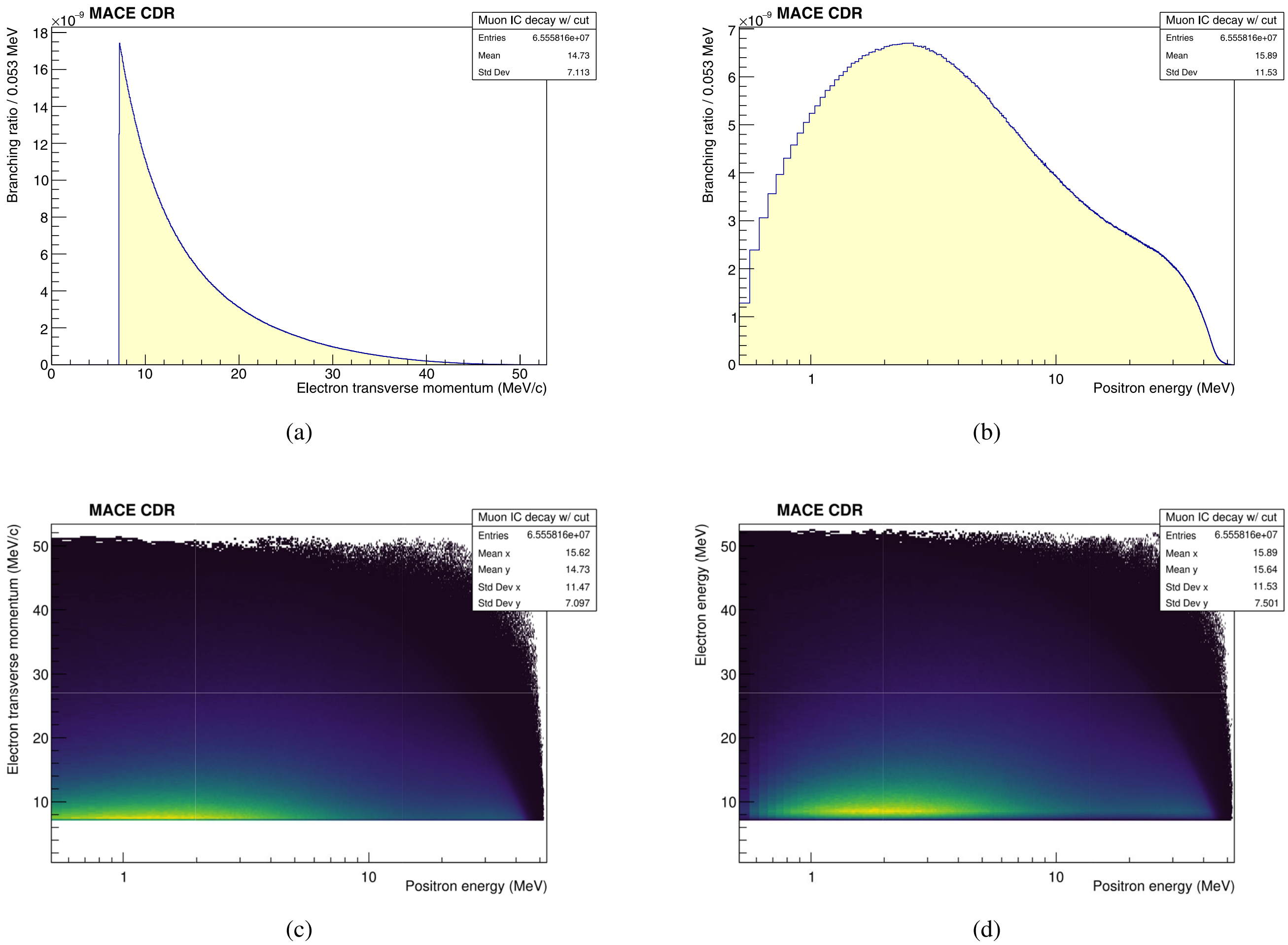

Fig. 9 (Color online) Spectra of muon internal conversion (IC) decay with MACE Michel electron magnetic spectrometer (MMS) geometric acceptance. **a** Transverse momentum spectrum of e^- from μ^+ IC decay (with detector geometric acceptance); **b** e^+ energy spectrum from μ^+ IC decay (with detector geometric acceptance); **c** Joint spectrum of e^+ energy and e^- transverse momentum from μ^+ IC decay; **d** Joint spectrum of e^+ energy and e^- energy from μ^+ IC decay

was estimated to be approximately 10^{-10}. In this scenario, a higher electron energy corresponds to a lower positron energy, indicating a higher momentum exchange and, consequently, a significantly reduced cross section when the final positron energy is sufficiently low. The background level is expected to be suppressed through an optimized detector design and a similar event selection scheme, as discussed above.

Accidental coincidences involving an energetic electron, potentially produced by Bhabha scattering, and a positron from muon or muonium decay represent another potential background source. If a Bhabha scattering event involving a Michel positron and an electron in the porous target material occurs near the material boundary, and the scattered positron is emitted from the material surface with low energy, it could fake a signal event. This process is similar to the Bhabha scattering of muonium decay final states, and similar strategies can be employed to suppress this type of background.

Furthermore, selection in an event-time window can improve the signal-to-background ratio [70]. All three types of background sources from muon or muonium decay are characterized by an exponentially decreasing time distribution proportional to $\exp(-t/\tau_\mu)$, where τ_μ is the muon lifetime. Notably, the muonium-to-antimuonium conversion probability varies over time and is proportional to $t^2 \exp(-t/\tau_\mu)$ [25, 56]. This time-dependent conversion increases the ratio of antimuonium decay to muonium or muon decay by t^2, thereby contributing to the signal-to-background ratio with accumulated time. Background suppression can be achieved by selecting a late event time window between the arrival of two beam pulses in a high-repetition-rate muon beam if necessary. A 40–50-kHz muon beam would potentially be available at the China initiative Accelerator Driven System (CiADS) in Huizhou (see Sect. 4) or Shanghai HIgh repetitioN rate XFEL and Extreme light facility (SHINE) [71].

In a concise overview, the following potential background contributions should be considered in MACE.

- **Internal conversion decay of muon**: The decay $\mu^+ \rightarrow e^+e^-e^+\nu_e\bar{\nu}_\mu$ could introduce an energetic electron and a slow positron in its final states simultaneously. If one positron falls within the signal region, while the other is undetected and the electron momentum is sufficiently high to pass the selection, the decay could fake a signal event.
- **Bhabha scattering of muonium decay final states**: Muonium decay final states involve a slow electron from the atomic shell and an energetic positron. Bhabha scattering between these particles can transfer momentum, potentially leading to a background event if momentum transfer is significant.
- **Accidental coincidences of Michel positron scattered with material electron**: Scattering of positrons generated from muon decay with electrons in the target material could generate an energetic electron and a low-energy positron.

The detector design should be optimized to enhance its ability to identify signals and background events. This includes improving the vertex resolution of the magnetic spectrometer, enhancing the resolution of low-energy positron time-of-flight measurements, and improving the energy resolution of the electromagnetic calorimeter to reduce accidental and physical backgrounds. Utilizing a state-of-the-art positron transport system to select the momentum of the transported particles can yield an optimal signal-to-background ratio. In addition, connecting to a high-repetition-rate muon source can further enhance the signal-to-background ratio. In subsequent sections, we discuss the experimental design and necessary specifications.

4 Beamline

The proposal for a high-intensity muon source, driven by the CiADS linac, has been under consideration for several years. From the perspective of beam power, such a muon source has the potential to be one of the state-of-the-art facilities worldwide. To address the challenges posed by unprecedented beam power, it is essential to explore novel target designs. Solenoid-based capture and transport are also crucial for achieving higher muon rates. Research and development of the CiADS muon source is currently in progress.

4.1 Accelerator and proton beam

The development of a superconducting linac for ADS in China began in 2011. The prototype front-end linac (CAFe), as shown in Fig. 10, was developed in stages and included an Electron Cyclotron Resonance (ECR) ion source, a Radio Frequency Quadrupole (RFQ), a superconducting acceleration section, and a 200-kW beam dump. The commissioning of the hundred kW beam started in 2018 and reached a milestone in early 2021 by producing a 20-MeV proton beam with an average current of 10 mA, demonstrating the feasibility of a superconducting linac in Continuous-Wave (CW) mode.

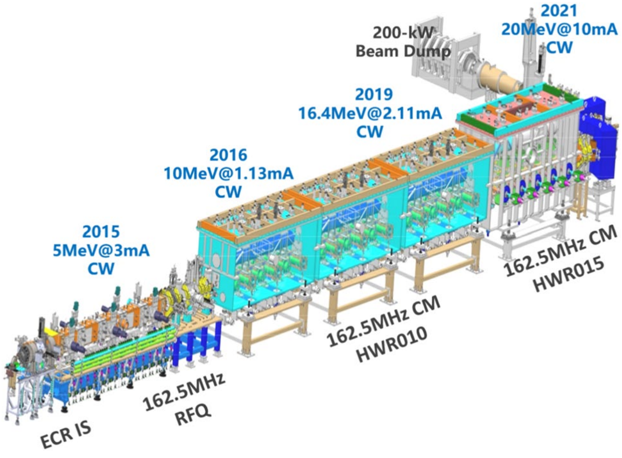

Fig. 10 (Color online) Schematic view of the development and commissioning history of CAFe [72]

The schematic diagram of the CiADS linac, illustrated in Fig. 11, consists of a normal conducting front-end, a superconducting acceleration section, and several High Energy Beam Transport (HEBT) lines. The civil construction of the linac is complete, and work on the experimental terminals is ongoing. The front-end, integrated in December 2022, includes an ECR ion source, a Low Energy Beam Transport (LEBT) with a fast chopper for beam pulse structuring and machine protection, an RFQ, and a Medium Energy Beam Transport (MEBT). The proton beam from the front-end was a CW beam with a current of 5.2 mA and an energy of 2.18 MeV. The superconducting section accelerated the beam from 2.1 MeV to 500 MeV. With a beam current of 50 μA on the target by 2025, the beam power will be 25 kW, and power ramping to 250 kW and 2.5 MW is expected by 2027 and 2029, respectively. The superconducting section houses three types of half-wave superconducting resonators (HWR010, HWR019, and HWR040) and two types of elliptical cavities (Ellip062 and Ellip082) in the 32 cryomodules. With the muon source proposal, the superconducting linac could potentially be upgraded to 600 MeV.

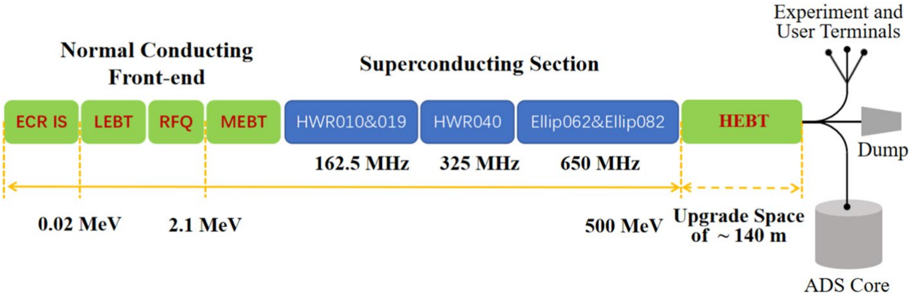

Fig. 11 (Color online) Schematic diagram of the CiADS linac [72]

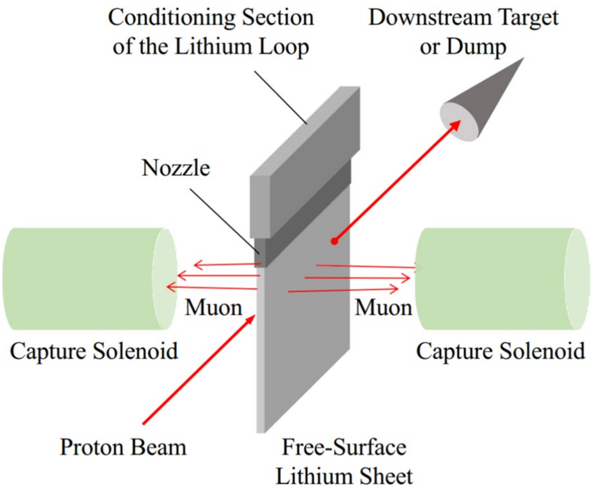

Fig. 12 (Color online) Schematic diagram of the free-surface liquid lithium target [72]

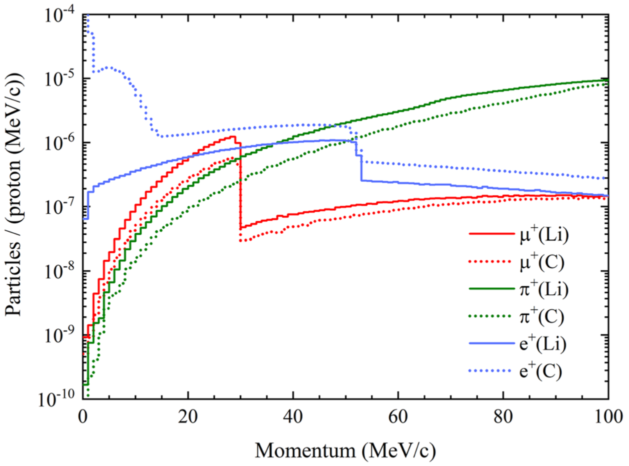

Fig. 13 (Color online) Momentum spectra of μ^+, π^+ and e^+ recorded by the virtual detector beside the target [72]

4.2 Muon production and transport

4.2.1 Muon production target

The production target for a high-intensity muon source is extremely challenging because it requires addressing high-heat densities and a harsh irradiation environment. Arising from the two-body decay of the positive pion stopped close to the surface of the production target, the surface muon escaped from the target with a momentum ranging from 0 to 29.8 MeV/*c*. A new design based on a free-surface and sheet-shaped liquid lithium target is shown in Fig. 12 [72]. Liquid lithium passes through the lithium circuit and forms a sheet jet from a narrow nozzle. The proton beam is collimated to hit the lithium jet at a small angle, and the surface muons produced inside the lithium that escape from both sides of the jet are captured by the solenoids.

Liquid lithium has been used as a neutron production target, radionuclide production target, and ion beam charge stripper because of its low melting point, extremely low saturated vapor pressure, high heat capacity, and good compatibility with structural materials. Maintaining the stability of free-surface liquid lithium flakes in a jet is a challenging design aspect. Extensive research and development studies have been conducted to investigate the feasibility of producing free-surface liquid lithium films or sheets.

A liquid lithium target is particularly well suited for high-intensity muon sources driven by the CiADS linac. First, lithium has a low atomic number *Z*, and research performed at PSI has shown that the surface muon production efficiency is roughly proportional to $Z^{-\frac{2}{3}}$. Second, the lithium target produces more low-energy π^+'s, resulting in more surface muons than the graphite target, with a significantly lower rate of positrons. Figure 13 shows the momentum spectra of the side-leaking μ^+, π^+ and e^+ from lithium and graphite targets recorded by a detector next to the target.

4.2.2 Muon beamline conceptual design

Through the interaction of the high-intensity proton beam with the muon target, the generated muons have a large transverse emittance and a significant longitudinal energy spread. A solenoid-based beamline concept was proposed to collect the large-emittance muon beam, as depicted in Fig. 14.

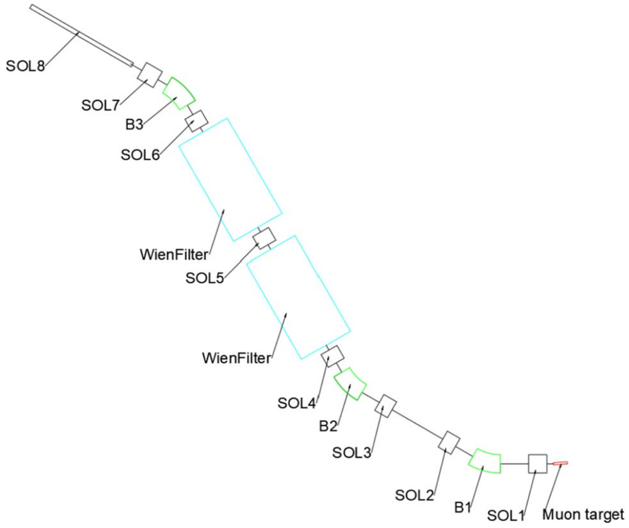

Fig. 14 (Color online) Schematic diagram of the beamline, featuring dipoles, wien filters and solenoids, denoted with the labels

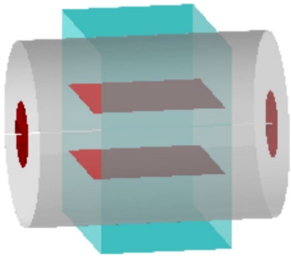

Fig. 15 (Color online) Schematic diagram of a Wien filter

The surface muon rate from the target is expected to reach up to 5×10^{11} μ^+/s with a 5 mA proton beam. The closer the capture solenoid is to the muon target, the higher the transmission efficiency. However, owing to spatial constraints, the capture solenoid was positioned 200 mm away from the muon target. Drawing on design experience from PSI, we opted for a shorter solenoid with a larger aperture to facilitate particle transport and enhance the transmission efficiency. The beamline employed a solenoid with a length of 400 mm and diameter of 500 mm. Considering space utilization and shielding effectiveness, we set three dipoles to rotate the beam clockwise, clockwise, and counterclockwise.

During muon collection in the target area and the subsequent beamline transport, a significant number of positrons are generated, which can affect the accuracy of the subsequent experimental results. The primary mechanisms for positron production include the decay of π^0 mesons into two photons, leading to the positron-electron pair production and the muon decay. Given that the decay length of muons is 170 m, the number of positrons produced during transport is relatively low; thus, the main source is π^0 mesons in the target. Figure 15 shows the schematic diagram of Wien filter modeling with G4beamline. A long Wien filter is typically employed to remove positrons from the low-momentum muon beams. Figure 16 shows the comparisons of positron removal effects using a long Wien filter or two short Wien filters. Simulations using the G4beamline indicate that placing two short Wien filters can effectively eliminate positrons and other charged particles while maintaining the transmission efficiency μ^+.

By externally invoking the TraceWin program and utilizing PSO (Particle Swarm Optimization) algorithm, we optimized each component of the beamline (hard edge model) to maximize overall transmission efficiency while minimizing beam spot size at the end. The optimized beam envelope plot is illustrated in Fig. 17. By externally invoking the G4beamline package and utilizing the Genetic Algorithm (GA) algorithm, we attempted to optimize each component of the beamline (real magnetic field). The transmission efficiency of the beamline was 3% with

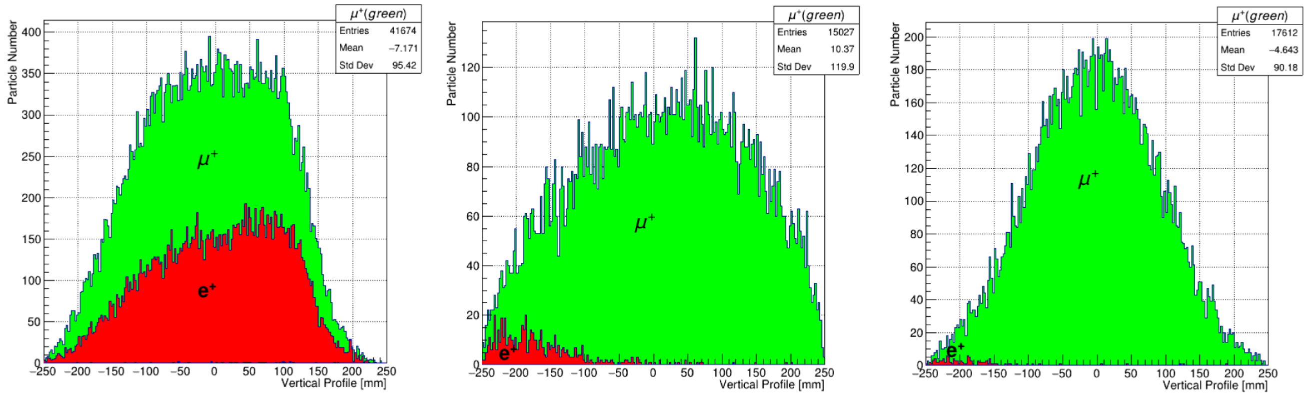

(a) (b) (c)

Fig. 16 (Color online) Comparisons of the positron removal effects using one long Wien filter and two short Wien filters. **a** Particle distribution at the entrance; **b** Particle distribution at the exit of a single long Wien filter; **c** Particle distribution at the exit of the second of two short Wien filter

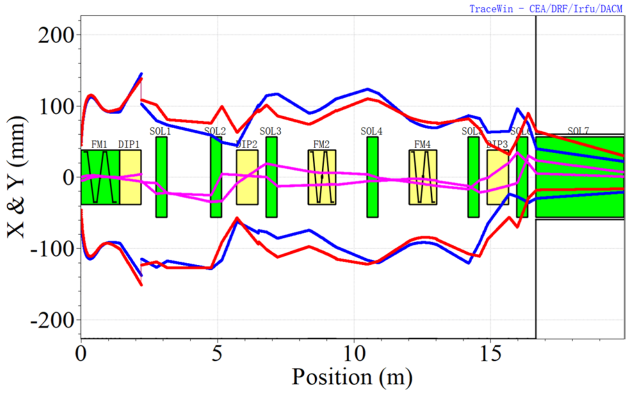

Fig. 17 (Color online) Beam envelope plot from the TraceWin software in the multi-particle mode with hard edge model

a transverse RMS size of approximately 20 mm. The surface muon beam rate will be up to 1.5×10^{10} μ^{+}/s with a 5 mA proton beam. Through further optimization, higher transmission efficiency and surface muon beam rate can be achieved.

5 Muonium production target

5.1 Introduction

The goal of MACE is to identify spontaneous muonium-to-antimuonium conversion events in vacuum. MACE cannot detect antimuonium decay events in materials for two reasons. First, atomic positrons are trapped in the material and are undetectable. Second, muonium-to-antimuonium conversion is a coherent process, and it is suppressed by decoherence owing to interactions between muonium and the material [73]. Therefore, enhancing the muonium yield is crucial for improving the signal-to-noise ratio. Consequently, increasing the sensitivity primarily involves maximizing the muonium yield in vacuum.

In the production of muonium in vacuum, a common approach involves directing a surface muon beam into a specific target material. A muon can spontaneously capture an electron to form a muonium atom. Subsequently, these muonium atoms diffuse within the material, with some escaping into vacuum. The ideal target materials for this purpose are porous and inert materials, such as silica powder or silica aerogel. A silica powder target can reach an efficiency of up to 8% for muonium emission into vacuum [74]. It was used in the MACS experiment, the most recent study on muonium-antimuonium conversion, where 5×10^{-3} muonium atoms were produced in a vacuum per incident muon [8]. In a more contemporary approach, silica aerogel is employed as the target for muonium production. The self-supporting and porous properties of silica aerogel, together with its relatively high muonium production efficiency, make it suitable for MACE.

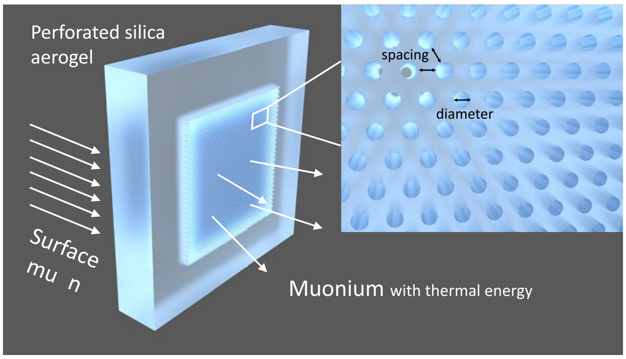

Fig. 18 (Color online) The single-layer perforated silica aerogel target concept [79]

However, research has indicated that a significant portion of muonium atoms remain trapped within the target [75, 76], which presents challenges in enhancing muonium emission efficiency. To enhance the diffusion of muonium atoms from the aerogel into the vacuum, prior studies have demonstrated that a perforated surface downstream, created using a pulsed laser, effectively enhances the diffusion of muonium atoms within the target and their emission into the vacuum [75]. The configuration of these perforations is shown in Fig. 18.

Laser ablation has also been demonstrated to be effective. Beare et al. conducted experiments at TRIUMF, investigating various parameters of the ablation structure, and achieved an emission efficiency (the ratio of muonium decay in a downstream vacuum to the total muonium formed) of up to 2% [77], representing an order of magnitude enhancement compared to the silica powder target. Additionally, Antognini et al. measured of muonium yields in a vacuum at PSI by employing a slow muon beam with momentum ranging from 11 to 13 MeV/*c*, achieving a yield (the ratio of muonium decay in a vacuum to the number of incident muons) of 6%. This yield was enhanced by utilizing a low beam momentum. Furthermore, the J-PARC muon $g-2$ experiment has designed to integrated a perforated silica aerogel target as a crucial component in muon cooling [78].

5.2 Design and optimization of single-layer target

In this study, we developed a Monte Carlo simulation method for muonium formation and diffusion in perforated silica aerogels. The independent simulation results were validated using experimental data. In this section, we summarize the geometrical design and simulation-guided optimization of the design.

For the benchmark design, a single-layer target geometry in the shape of a cuboid was selected, with its short edge aligned parallel to the beam direction (z-axis), and the remaining two longer edges of equal length. The downstream face of the target was perforated with blind-ended cylindrical holes perpendicular to the surface arranged in an equilateral lattice pattern. A schematic is shown in Fig. 18. The geometry was parameterized as follows:

- The cuboid geometry: the width and the thickness of the target;
- The perforation geometry: the spacing (s), the diameter (ϕ) and the depth (d) of the blind-ended holes.

The width and thickness of the target were determined using beam parameters. Specifically, the width is determined by the beam spot size, ensuring that it is sufficiently large to cover the entire beam spot for the maximum utilization of the beam flux. The target thickness was related to the beam momentum and momentum spread. It should be adjusted to maximize muonium yield, taking into account any additional materials, such as beam momentum degraders or beam monitors located upstream. In the benchmark design, the target dimensions were 60 mm × 60 mm (width) × 10 mm (thickness), with an aluminum beam degrader positioned upstream, whose thickness can be tuned.

Perforation geometry requires further consideration. Increasing the spacing between the holes results in more material, thereby leading to higher rates of muon stopping and increased muonium production. However, these muonium atoms may encounter difficulties in vacuum emission owing to obstruction from the material. Conversely, enlarging the hole diameter can enhance the emission efficiency but may decrease the overall muonium yield. Therefore, it is likely that a specific combination of geometric parameters yields the highest vacuum yield when the material and beam conditions are held constant.

It is essential to conduct a combined optimization of the geometric parameters. To perform this process, the first step involves defining the physical quantities relevant to muonium production in vacuum. Five quantities, $f_{\mu^+}^{\mathrm{stop}}$, f_{M}, Y_{tot}, R_{vac}, and Y_{vac}, were used to characterize the formation and emission of muonium. These quantities represent the muonium formation fraction, muon-stopping fraction, total muonium yield, muonium emission efficiency, and muonium yield in vacuum, respectively. They are expressed as

$$f_{\mu^+}^{\mathrm{stop}} = \frac{N_{\mu^+}^{\mathrm{stop}}}{N_{\mu^+}^{\mathrm{OT}}}\,, \quad f_{\mathrm{M}} = \frac{N_{\mathrm{M}}^{\mathrm{tot}}}{N_{\mu^+}^{\mathrm{stop}}}\,, \quad Y_{\mathrm{tot}} = \frac{N_{\mathrm{M}}^{\mathrm{tot}}}{N_{\mu^+}^{\mathrm{OT}}}\,, \\ R_{\mathrm{vac}} = \frac{N_{\mathrm{M}}^{\mathrm{vac}}}{N_{\mathrm{M}}^{\mathrm{tot}}}\,, \quad Y_{\mathrm{vac}} = \frac{N_{\mathrm{M}}^{\mathrm{vac}}}{N_{\mu^+}^{\mathrm{OT}}}\,. \tag{30}$$

In these equations, $N_{\mu^+}^{\mathrm{stop}}$ denotes the number of muons stopped at the target, $N_{\mu^+}^{\mathrm{OT}}$ denotes the total number of muons on the target, $N_{\mathrm{M}}^{\mathrm{tot}}$ denotes the total number of muonium produced, and $N_{\mathrm{M}}^{\mathrm{vac}}$ denotes the number of muonium in vacuum. Noteworthy relationships exist among these quantities, including

$$Y_{\mathrm{tot}} = f_{\mathrm{M}} f_{\mu^+}^{\mathrm{stop}}\,, \quad Y_{\mathrm{vac}} = R_{\mathrm{vac}} Y_{\mathrm{tot}} = R_{\mathrm{vac}} f_{\mathrm{M}} f_{\mu^+}^{\mathrm{stop}}\,. \tag{31}$$

The value of f_{M} is predominantly influenced by the material properties and $f_{\mu^+}^{\mathrm{stop}}$ is associated with both material properties and beam conditions; both R_{vac} and $f_{\mu^+}^{\mathrm{stop}}$ are affected by the aerogel target geometry. A more detailed discussion on the relationships between these quantities can be found in Ref. [79].

Simulation-guided optimization was conducted as follows. The perforation structure is consistent with that shown in Fig. 18, featuring a target size of 60 mm × 60 mm × 10 mm and ablation holes with varying geometric parameters within the 40 mm × 40 mm region at the center of the downstream surface. The temperature was fixed at 322 K, the aerogel density was set to 27 mg/cm^3, and the muonium mean free path was 250 nm, all of which served as inputs for the Monte Carlo model parameters.

An aluminum degrader was positioned 5 mm in front of the target, where the muon beam traverses and loses energy. A fraction of the muons stops in the target and forms muonium atoms. The degrader, with varying thicknesses, produces different distributions of muon stopping positions, thereby influencing the emission of muonium into vacuum and resulting in varying vacuum yields. Therefore, optimizing the degrader thickness is crucial for maximizing the yield, as illustrated in the simulation results shown in Fig. 19. Based on these results, we found that the optimal degrader thicknesses for this single-layer target with momentum spreads of 2.5%, 5%, and 10% are 430 µm, 410 µm, and 370 µm, respectively.

Using these optimal degrader configurations, the perforation geometry can be optimized, involving hole spacing ranging from 0 to 100 µm, diameters ranging from 40 to 360 µm, and depths of 1, 2, and 5 mm. The simulation results are presented in Fig. 20, and the optimal values are shown in Table 2. As illustrated in Fig. 20, maxima in the muonium emission efficiency and vacuum yield are observed. When the spacing and diameter deviate from their optimal values, the yield in vacuum gradually decreases, with significant suppression occurring when the spacing or diameter becomes excessively small.

In summary, for the design of a single-layer target, we recommend an appropriate configuration of perforation parameters that balances the total muonium yield (Y_{tot}) and

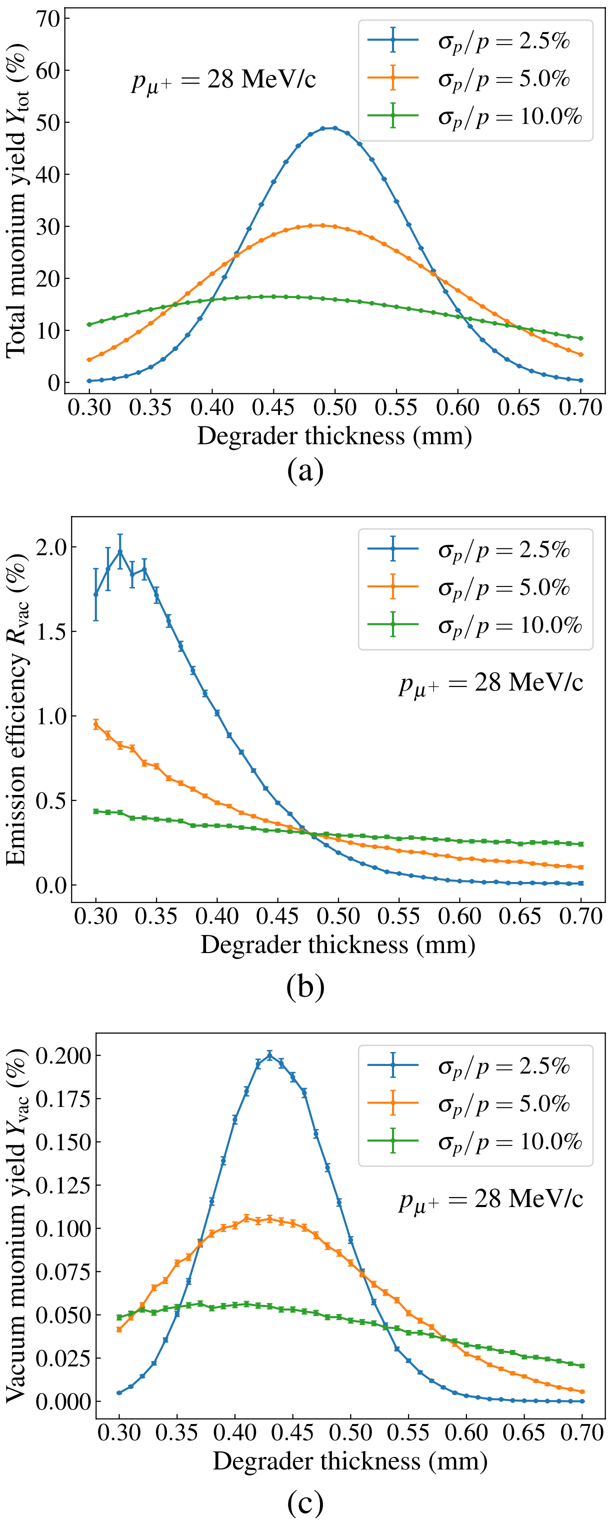

Fig. 19 (Color online) Muonium production and emission from a flat silica aerogel target with different aluminum degraders ($t_{\mathrm{target}} = 10$ mm, $\rho_{\mathrm{target}} = 30$ mg/cm^3, $\lambda = 200$ nm, and $T = 322$ K) [79]. **a** Total yield Y_{tot}; **b** Emission efficiency R_{vac}; **c** Vacuum yield Y_{vac}

muonium emission efficiency (R_{vac}) to achieve an optimal muonium yield in vacuum (Y_{vac}). This optimization can be realized through a combination of the simulation-guided optimization procedure proposed in Ref. [79] and data-driven experimental optimizations. These approaches are shared between single-layer and multi-layer target designs and will be employed in future technical designs to refine and determine optimal configurations.

5.3 Multi-layer target design

The perforated single-layer target has the potential to achieve a high muonium yield in vacuum; however, there is still room for improvement. In the single-layer target design, the perforated surface faces downstream relative to the beam, and it is expected that nearly half of the muons will stop within the target, to maximize the number density of muons stopped near the perforated surface. This configuration implies that nearly half of the muon beam penetrates the target without being used. Additionally, the single-layer target favors a more concentrated momentum spread to minimize the spread of muon stopping positions; therefore, a high muonium yield in vacuum requires a low beam momentum spread. As observed in Sect. 5.2, an increased beam momentum spread significantly suppresses the muonium yield in vacuum, which is not expected because it amplifies the correlation between muonium yield and beam momentum spread. This reduces the design margins and may increase the systematic errors associated with muonium yield. Therefore, we expect a target design that can enhance the utilization of muon beam flux while tolerating a wider beam momentum spread. The design of a multilayer silica aerogel target has the potential to achieve this goal.

The original concept of a multi-layer silica aerogel target was proposed by Zhang et al. [80], with the aim of increasing the total muonium yield in vacuum to enhance the efficiency of converting a surface muon beam into a thermal muon beam by ionizing the muonium atoms produced in vacuum. This technology, known as muon cooling, shares the same objective of increasing the muonium yield in a vacuum as MACE. In the simulation work by Zhang et al., the multilayer target design was shown to increase the muonium yield in vacuum by a factor of 3.45.

The design horizontally aligns multiple silica aerogel targets in parallel, with the muon beam directed parallel to the layers. Each silica aerogel layer was perforated, allowing muonium atoms produced within the layer to diffuse and escape into the interlayer vacuum. If these muonium atoms are converted into antimuonium and decayed, low-energy positrons will be accelerated parallel to the target layer, exiting the target region, and guided to the positron detection system. This target concept is illustrated in Figs. 21 and 22. In scenarios where the beam may be well collimated, it can

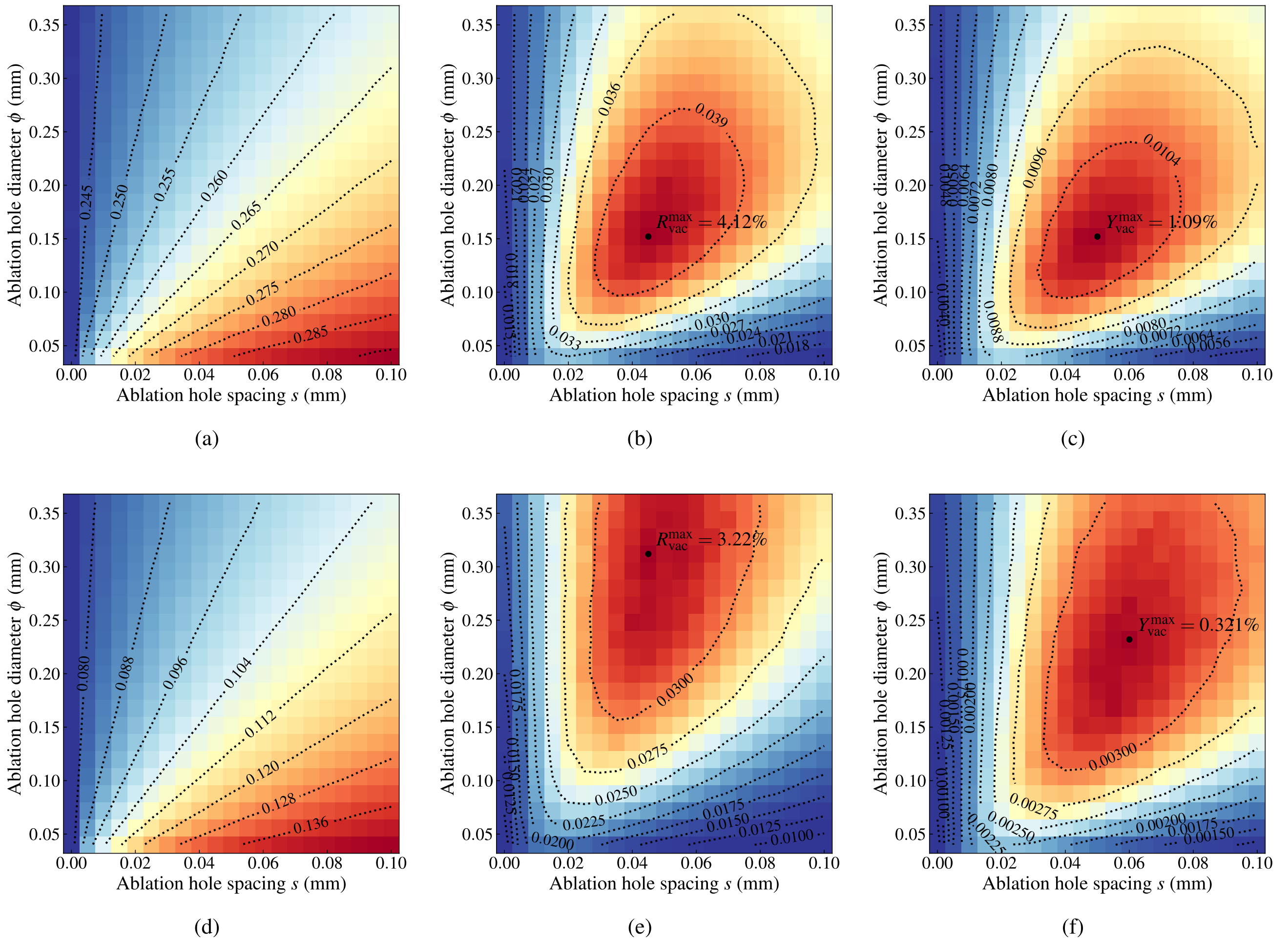

(a) (b) (c)

(d) (e) (f)

Fig. 20 (Color online) Projection of total muonium yield, muonium emission efficiency, and vacuum muonium yield under different beam conditions and target geometries [79]. **a** Total muonium yield $Y_{\rm tot}$ ($\sigma_{\rm p}/p = 2.5\%$, $d = 1$ mm); **b** Emission efficiency $R_{\rm vac}$ ($\sigma_{\rm p}/p = 2.5\%$, $d = 1$ mm); **c** Muonium yield in a vacuum $Y_{\rm vac}$ ($\sigma_{\rm p}/p = 2.5\%$, $d = 1$ mm); **d** Total muonium yield $Y_{\rm tot}$ ($\sigma_{\rm p}/p = 10\%$, $d = 5$ mm); **e** Emission efficiency $R_{\rm vac}$ ($\sigma_{\rm p}/p = 10\%$, $d = 5$ mm); **f** Muonium yield in a vacuum $Y_{\rm vac}$ ($\sigma_{\rm p}/p = 10\%$, $d = 5$ mm)

Table 2 Simulation of maximum muonium yield in a vacuum and corresponding optimal spacing and diameter with different beam condition [79]. Only statistical errors are shown in this table

$p_{\rm beam}$ (MeV/c)	$\frac{\sigma_{p_{\rm beam}}}{p_{\rm beam}}$ (%)	Depth d (mm)	Spacing s (μm)	Diameter ϕ (μm)	Max M yield in vacuum $Y_{\rm vac}$ (%)
28	2.5	1	50 ± 5	152 ± 16	1.092 ± 0.002
		2	55 ± 5	184 ± 16	1.134 ± 0.002
		5	55 ± 5	184 ± 16	1.122 ± 0.002
	5	1	50 ± 5	152 ± 16	0.583 ± 0.001
		2	60 ± 5	216 ± 16	0.607 ± 0.001
		5	50 ± 5	184 ± 16	0.604 ± 0.001
	10	1	50 ± 5	152 ± 16	0.305 ± 0.001
		2	55 ± 5	200 ± 16	0.320 ± 0.001
		5	60 ± 5	232 ± 16	0.321 ± 0.001

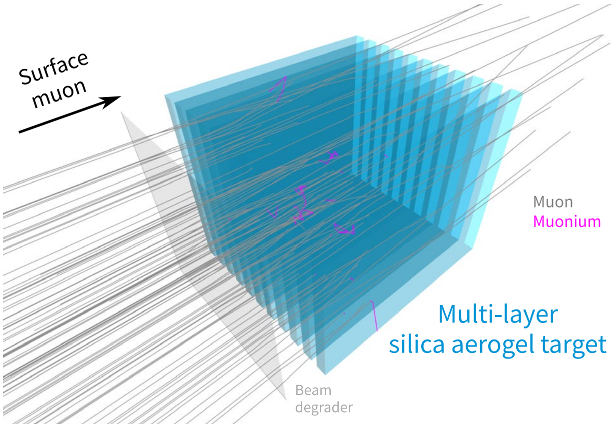

Fig. 21 (Color online) The multi-layer silica aerogel target concept

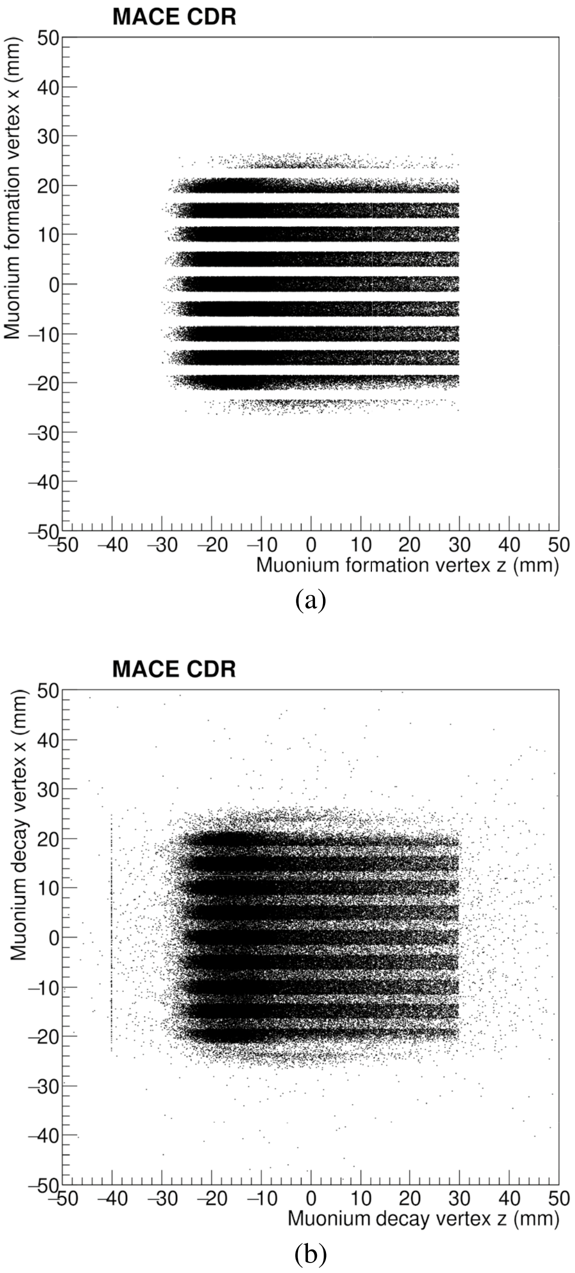

(a)

(b)

Fig. 22 Simulated distributions of muonium formation (**a**) and decay vertices (**b**). A few percents of muonium atoms will diffuse out of the target before their decay

Table 3 Simulated muonium yield in different multi-layer targets. Only statistical errors are shown in this table

Thickness (mm)	Spacing (mm)	Aerogel count	Y_{tot} (%)	R_{vac} (%)	Y_{vac} (%)
2	2	13	20.33(5)	24.3(1)	4.94(2)
	3	11	16.04(4)	27.6(1)	4.43(2)
	4	9	13.13(4)	29.3(2)	3.85(2)
3	2	11	22.40(5)	17.04(9)	3.82(2)
	3	9	19.01(5)	19.2(1)	3.66(2)
	4	8	16.00(4)	20.5(1)	3.28(2)
4	2	9	24.14(5)	13.08(8)	3.16(2)
	3	8	20.80(5)	14.83(9)	3.09(2)
	4	7	17.44(5)	15.8(1)	2.76(2)

pass through the target via the spaces between the silica aerogel layers, potentially leading to reduced utilization of the muon beam flux. To address this, a beam degrader may be introduced in front of the multilayer target to scatter the beam if necessary. Using this design, the utilization of muon beams can be effectively enhanced. Furthermore, unlike the single-layer target design, the longitudinal length of the multilayer target can be extended without significantly compromising the muonium emission efficiency because muonium atoms diffuse and escape primarily in the transverse direction. Consequently, this design achieves the goal of increasing the muon beam utilization while tolerating a wider beam momentum spread.

We conducted simulations of various multilayer target designs. We utilized a beam momentum of 24 MeV/c and an RMS spread of 1.35 MeV/c. The beam is assumed to be collimated, resulting in a beam spot of 40 mm×40 mm square, where the muons are uniformly distributed. Each layer had a longitudinal length of 60 mm, a height of 50 mm, and varying thicknesses of 2, 3, and 4 mm. The layers were perforated in a 50 mm×40 mm region at the center. The perforation parameters for the aerogel layers were inherited from the optimal parameters of the single-layer target design, that is, a hole spacing of 55 μm and a hole diameter of 184 μm. The spacing between adjacent layers was kept constant, varying from 2, 3, to 4 mm. The number of silica aerogel layers was selected to ensure that the overall height and width of the target shape matched.

In the simulation, 10^6 μ^+ were generated for each target design, and the results are summarized in Table 3. The definitions of the result parameters are consistent with those described in Sect. 5.2, with the exception that "in-vacuum muonium" is counted only in the vacuum region of interest, where atomic positrons from antimuonium decay can be accelerated and transported to the positron detection system. From the simulation results, we observed that the muonium yields in vacuum (Y_{vac}) are enhanced by factors of 2 to 4 compared to the single-layer target. This enhancement is primarily attributed to an increase in muonium emission efficiency (R_{vac}).

The optimal result is achieved with the smallest single-layer thickness and layer spacing, both at 2 mm, resulting in a muonium yield in vacuum of 4.94(2)%. Although the yield is high, the multilayer target has intrinsic limitations.

The major concern raised by excessive muonium scattering between the silica aerogel layers would quench the muonium conversion probability if the layer spacing is too narrow. Therefore, a larger layer spacing is preferred, and we selected a muonium yield in a vacuum of 3.8% as the benchmark parameter. In conclusion, the results demonstrate the possibility of increasing the muonium yield in a vacuum to a few percent if the target geometry is properly designed.

6 Overview of detector system

To identify the signal signature demonstrated in Sect. 3.1, the MACE detector design includes three primary components: a Michel electron magnetic spectrometer (MMS), a momentum-selective positron transport system (PTS), and a positron detection system (PDS), as shown in Fig. 23. The Michel electron magnetic spectrometer consists of a cylindrical drift chamber (CDC), a set of tiled timing counters (TTC), and a magnet. The MMS is used to measure the tracks and momenta of the high-energy electrons. The positron transport system includes an electrostatic accelerator and a positron transport solenoid, which transport low-energy positrons to the positron detection system

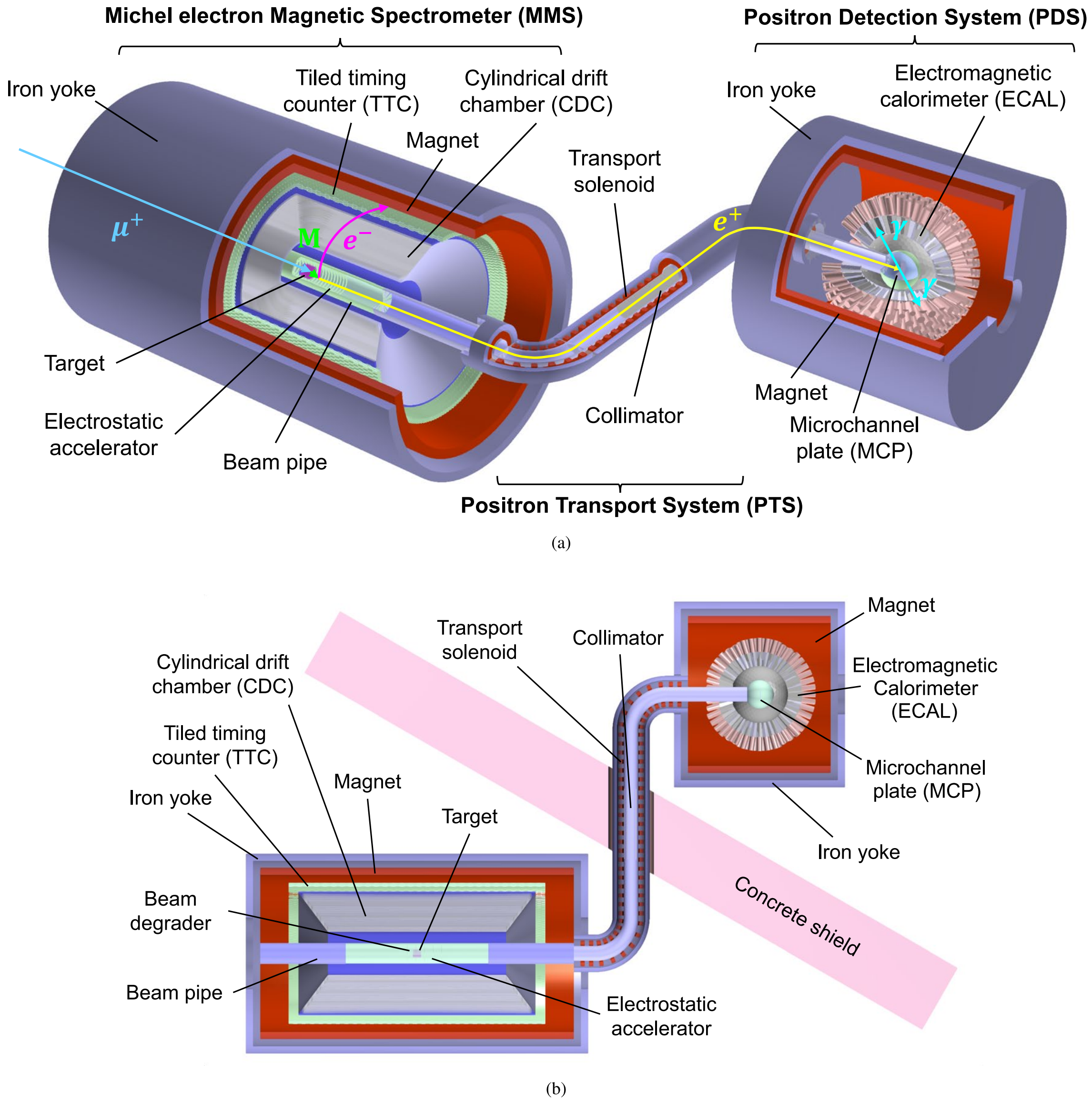

(a)

(b)

Fig. 23 (Color online) MACE detector concept. **a** Perspective view; **b** Top view while conserving their transverse position. PDS includes a microchannel plate (MCP) detector and an electromagnetic calorimeter (ECAL), with the MCP detecting the transverse position of positrons and the ECAL detecting gamma rays produced from annihilation events on the MCP.

MACE uses coincident detection from a Michel electron magnetic spectrometer and a positron detection system to discriminate and detect antimuonium signals. Initially, a positron was identified through the coincidence of a hit in the MCP and annihilation signals in the calorimeter. By considering the conservation of the transverse position of positrons in the transport system, the transverse projection of the positron was spatially matched with the track of high-energy electrons measured by the magnetic spectrometer. Most background positrons were filtered out during transportation in the solenoid using a fine collimator. Finally, by comparing the time difference measured by both the PDS and MMS with the expected signal time-of-flight, an antimuonium decay signal can be identified.

In summary, the detection scheme involves primary detector signals as follows:

- An energetic electron track in the Michel electron magnetic spectrometer (MMS);
- A hit on the microchannel plate (MCP);
- Annihilation gamma ray signals in the electromagnetic calorimeter (ECAL).

When these signals coincide, they are identified as a muonium-to-antimuonium conversion event:

- A positron is identified in the positron detection system (PDS), indicated by the MCP hit coinciding in time with the annihilation signals in the calorimeter;
- The positron's transverse position, indicated by the hit on the MCP, matches with the electron track detected in the MMS;
- The positron's time-of-flight (TOF) is within the expected signal TOF range.

7 Michel electron magnetic spectrometer

The Michel electron magnetic spectrometer (MMS) is responsible for detecting and identifying electrons or positrons and measuring their time, track, and momenta for coincidence detection and event selection purposes. The MMS must exhibit outstanding spatial resolution to enhance vertex reconstruction precision, thereby allowing the MACE to effectively reject accidental backgrounds. An extremely low charge misidentification rate is essential to avoid the introduction of additional accidental backgrounds. Moreover, it should possess a good momentum resolution to facilitate physical analysis and enhance sensitivity to other potential physics subjects.

The primary component of the MMS is a cylindrical drift chamber (CDC) designed to track the decay products of muons, muonium, and antimuonium, specifically the positrons and electrons. The CDC should feature a large geometric acceptance to ensure adequate signal efficiency as well as excellent spatial resolution for optimal momentum and vertex resolution. Surrounding the CDC barrel is a set of timing counters, known as the tiled timing counter (TTC), which functions as the event trigger. Both CDC and TTC are situated within an axial magnetic field to curve the charged tracks and discriminate between electrons and positrons. The central alignment of the entire MMS system corresponds to the muonium target, which is the origin point of most tracks.

7.1 Magnetic field and magnet

A solenoid magnet surrounds CDC and TTC to provide an axial magnetic field. Increasing the magnetic flux density can enhance the momentum resolution and reduce the charge misidentification rate of the MMS by increasing track curvature. However, the muonium conversion process is influenced by the magnetic field; because the target is positioned at the center of the MMS, this field affects the conversion process. A strong magnetic field suppresses the contributions of certain operators in the conversion process, creating a trade-off between the MMS performance and physical sensitivity. As discussed in Ref. [56, 57], muonium conversion induced by $(V \pm A) \times (V \pm A)$ and $(S \pm P) \times (S \pm P)$ effective couplings is significantly reduced when the magnetic field reaches 1 T or higher. To maintain sensitivity of the MACE to all effective operators and constrain the parameter space, the MMS operates at $B = 0.1$ T. This magnetic field achieves balance, ensuring MMS performance while preserving reasonable conversion probabilities associated with $(V \pm A) \times (V \pm A)$ and $(S \pm P) \times (S \pm P)$ couplings. This configuration is consistent with the choices made in the MACS experiment [8]. Further details of the magnet design are provided in Sect. 8.1.

7.2 Cylindrical drift chamber

7.2.1 Design objectives

A cylindrical drift chamber (CDC) is responsible for tracking the charged particles. To enhance sensitivity, identify between muonium or muon decay and antimuonium decay, and improve the discrimination between signal and background events, the drift chamber should have a high detection efficiency and large geometric acceptance. High spatial resolution, low charge misidentification rate, and high momentum resolution are also essential for enhancing sensitivity. These criteria guide the design of the MACE cylindrical drift chamber. Therefore, we propose the deployment of a light, small-cell cylindrical drift chamber with appropriate wiring configurations. The design objectives are described as follows.

Reducing the amount of materials is the primary focus of drift chamber design. The tracked particles, electrons, and positrons were significantly disturbed by multiple scattering and Coulomb scattering. These types of scattering affect the resolution of a drift chamber, also known as the material effect. The material budget is mainly composed of three parts: gas, wires, and inner wall. The endplates and outer walls are not considered because MACE does not consider the particle momentum after passing the CDC. Among these three parts, gas and wires are the main contributors to the material budget. Therefore, the adopting a helium-based gas becomes an optimal solution to improve the momentum resolution. This is also the choice for drift chambers constructed in recent years [81–84]. On the other hand, the vertex resolution is a primary focus of MACE to reject accidental backgrounds. A light inner wall leads to less track distortion, thereby contributing to the decay vertex resolution of a track coinciding with an MCP hit. A thin carbon fiber inner wall is a common solution in collider experiments. However, this is not sufficiently light for muon experiments. In MEG II, an aluminated Mylar cylindrical foil of 20 μm thickness is utilized to close the inner surface of the chamber [84]. Aluminated Mylar serves as an option for MACE to further reduce the material budget and improve vertex resolution. Except for gas and the inner wall, wires are another source of material budget. A direct method to reduce the number of wires is to reduce the number of cells. However, it reduces the rate tolerance of the drift chamber, which is not favorable for MACE because of the high event rate, as discussed below. In summary, helium-based gas and aluminated Mylar cylindrical foil as the inner wall serve as an optimal solution to minimize the material budget.

MACE will be connected to an intense muon beam with a flux of 10^8 μ^+/s, whose decay products will directly enter the CDC; therefore, the event rate and occupancy must be considered. The beam flux results in a physical event rate in the CDC of 7×10^7/s, assuming that 80% of the muons are stopped and decay within the MMS and that the MMS acceptance is 90%. The total event rate within a layer will be less than or equal to the total event rate, with the highest rate expected to be found in the innermost layer because it has the fewest cells. As a gas detector, CDC has a specific dead time after a trigger in a cell, during which subsequent track passages will not trigger the cell, resulting in missed events. The miss rate can be estimated using formula $2\tau n^2$, where τ represents the dead time and n is the event rate. Therefore, the event miss rate in a layer is given by

Table 4 Geometric parameters of the cylindrical drift chamber

Parameter	Value
Inner radius (cm)	150
Outer radius (mm)	415
Inner length (mm)	1200
Outer length (mm)	1600
Number of layers	21
Number of cells	3536
Geometric acceptance	88.8%

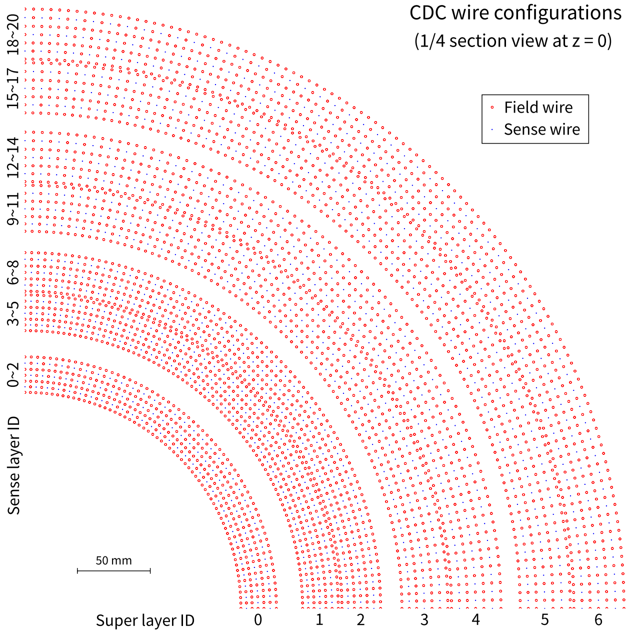

Fig. 24 (Color online) A 1/4 section view of CDC wires at $z = 0$, where the red and blue circles are the field and sense wires, respectively. The wire radii were scaled 20 times for clarity. The CDC consists of concentric layers of wires with alternating directions, the odd-numbered super layers being stereo and the even-numbered super layers being axial

$$n_{\text{miss}} = N_{\text{cell}} \times 2\tau \left(\frac{n_{\text{total}}}{N_{\text{cell}}} \right)^2 = \frac{2\tau n_{\text{total}}^2}{N_{\text{cell}}} , \tag{32}$$

where $n_{\text{total}} = 7 \times 10^7$/s is the physical event rate and N_{cell} is the number of cells in a layer. Assuming a dead time of $\tau = 100$ ns, if we want the miss rate in a layer to be less than the threshold of $n_{\text{threshold}} = 10^7$/s, i.e., $n_{\text{miss}} < n_{\text{threshold}}$, we find that

$$N_{\text{cell}} > \frac{2\tau n_{\text{total}}^2}{n_{\text{threshold}}} \approx 100 . \tag{33}$$

In other words, if one layer contains 100 cells, the ratio of the event miss rate to the physical event rate will be slightly more than ten percent. Therefore, a lower bound of at least

100 cells was established in each layer. For a cylindrical drift chamber with an inner diameter of 30 cm, this minimum number of cells implies a maximum cell width of 9 mm in the innermost layer, thus setting an upper limit for the cell width in that layer.

7.2.2 Wire configurations

Following these objectives, we considered CDC geometry consisting of near-squared cells. One cell had a 20 µm gold-plated tungsten sense wire at the center, surrounded by eight 80 µm aluminum field wires, as shown in Fig. 24. Cells are azimuthally arranged in sense layers, in which they share the same width, length, and stereo angle. Three adjacent sense layers are grouped into a super layer, in which the sense layers share the same stereo orientation, number of cells, and cell azimuth angular width. In a super layer, two adjacent layers are staggered by a half-cell to resolve the left-right ambiguity.

The current design contained seven super layers, with three sense layers in each super layer, resulting in a total of 21 layers. Each sense layer contains 124–212 cells according to the superlayer where they are located. This resulted in a total of 3540 cells, comprising 12980 field wires and 3540 sense wires. Among the seven super layers, three are axial layers whose cells orient axially, and the remaining four super layers are stereo layers. The stereo orientations are alternately arranged, with the first super layer being positively twisted, the third super layer being negatively twisted, etc., forming a UAVAUAV-twisted pattern. Detailed configurations are listed in Tables 4 and 5. Stereo layers have a hyperbolic profile as shown in Fig. 25. This introduces radial shrinkage toward the center, leaving a clear space between the next axial super layer in the region close to the central *xy* plane, as well as a clear space between the last axial layer in the region close to the endplate. Therefore, the field-wire layer is not shared between two adjacent super layers, resulting in cell geometries that are nearly identical.

The stereo angle (ϕ_{stereo}) is defined as the angle at which the projection of the line on the *xy* plane spans the origin, and ranges from 430 mrad to 815 mrad. A large stereo angle provides excellent resolution along the axial direction. However, additional considerations are needed in future technical design. The cell widths range from 8 to 12 mm, offering good event rate tolerance under intensive muon decay event rates. The inner radius and length of the CDC are 150 and 1200 mm, respectively, while the outer radius and length are 415 and 1600 mm, respectively. Consequently, the geometric acceptance of the CDC was 88.8%. This also specifies the geometric acceptance of the tiled timing counter (TTC) to be discussed below. The overall acceptance of the MMS system is a combination of CDC and TTC.

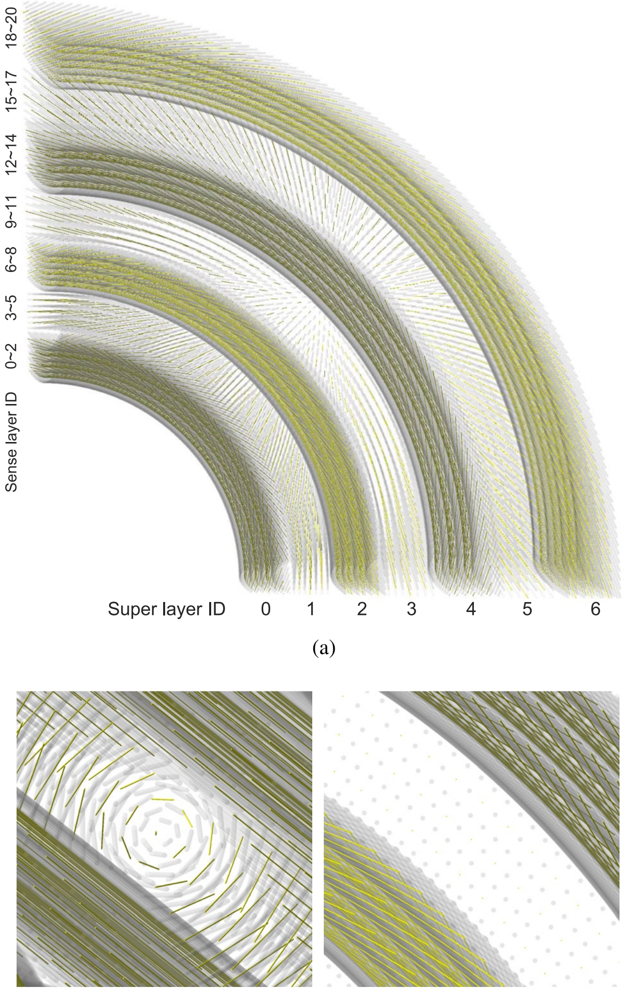

(a)

(b)

(c)

Fig. 25 (Color online) Perspective view of CDC wires, where golden wires denote sense wires and translucent-gray wires denote field wires. The wire radii were scaled 20 times to be clearly visible. A hyperbolic profile due to stereo wires in super layer 0, 2, 4, and 6 can be seen in the 1/4 clip-away view. **a** 1/4 clip-away perspective view; **b** The ID = 2 super layer; c The ID = 3 super layer

7.3 Tiled timing counter

The goal of MACE is to identify spontaneous muonium-to-antimuonium conversion events in a vacuum. The tiled timing counter (TTC) is one of the core components of the MACE detector system, with its primary objective being to provide timing for particle tracks, particularly for the signal electron tracks. TTC triggers a data acquisition system by detecting positrons or electrons resulting from muon decay or signal events. It is essential for a tiled timing counter to have a high time resolution to accurately measure the arrival times of these particles. This capability enhances the performance of the MACE detector system in two key ways: (1) it improves the time-of-flight resolution for signal

Table 5 Wire configurations of MACE cylindrical drift chamber

Super layer ID	Sense layer ID	Cell ID	Radius at layer center (mm)	ϕ_{stereo} (mrad)	$\phi_{\text{1st cell}}$ (mrad)	Cell width (mm)	Cell length along z (mm)
0	0	0–123	155.992	799.799	0	7.904	1222.530
	1	124–247	164.102	807.591	25.3354	8.315	1235.834
	2	248–371	172.633	815.790	0	8.747	1249.881
1	3	372–527	197.896	0	20.1384	7.971	1265.806
	4	528–683	206.030	0	0	8.298	1277.762
	5	684–839	214.499	0	20.1384	8.639	1290.209
2	6	840–1003	224.193	−611.622	0	8.589	1320.833
	7	1004–1167	232.950	−617.639	19.1561	8.925	1334.688
	8	1168–1331	242.049	−623.892	0	9.273	1349.115
3	9	1332–1495	265.361	0	19.1561	10.167	1365.356
	10	1496–1659	275.726	0	0	10.564	1380.606
	11	1660–1823	286.496	0	19.1561	10.976	1396.451
4	12	1824–1991	298.649	501.677	0	11.169	1428.736
	13	1992–2159	310.031	507.616	18.7000	11.595	1446.392
	14	2160–2327	321.847	513.782	0	12.037	1464.754
5	15	2328–2519	345.728	0	16.3625	11.314	1485.046
	16	2520–2711	357.230	0	0	11.690	1502.017
	17	2712–2903	369.115	0	16.3625	12.079	1519.553
6	18	2904–3115	381.894	−427.111	0	11.318	1552.408
	19	3116–3327	393.382	−431.826	14.8188	11.659	1570.086
	20	3328–3539	405.217	−436.683	0	12.010	1588.319

positrons by providing an accurate decay vertex time and (2) it increases the resolution of the CDC through enhanced drift time resolution, which assists in precise track reconstruction and minimizes the number of fake tracks.

7.3.1 Design objectives

a. Time resolution. A time resolution of $\mathcal{O}(100)$ ps was achieved using the TTC. TTC contributes to the measurement of the slow signal positron time-of-flight (TOF) by providing the anti-muonium decay time. The signal positron TOF is determined by the time difference between the decay time and hit time of a coincident microchannel plate (MCP) event. The improved time resolution narrows the signal region, enabling better rejection of background events. Based on the simulation results presented in Sect. 8.2, the intrinsic spread of the signal positron TOF distribution was approximately 7 ns. The MCP can achieve a time resolution of $\mathcal{O}(100)$ ps, which is approximately an order of magnitude better than the intrinsic TOF spread; thus, if the TTC also meets the $\mathcal{O}(100)$ ps time resolution requirement, it can eliminate the detector resolution effect on the TOF measurement. To satisfy the $\mathcal{O}(100)$ ps time resolution requirement, fast plastic scintillators such as EJ-228 or EJ-230 [85] with reasonably small dimensions of less than 50 mm are suitable options. These scintillators can achieve a scintillation rise time of 0.5 ns and a fall time of 1.5 ns, as specified in the vendor's product documentation (see Table 6).

Table 6 Properties of EJ-228 and EJ-230 scintillators [85]

Properties	EJ-228	EJ-230
Light output (% anthracene)	67	64
Scintillation efficiency (photons/1 MeV e^-)	10200	9700
Wavelength of maximum emission (nm)	391	391
Light attenuation length (cm)	-	120
Rise time (ns)	0.5	0.5
Decay time (ns)	1.4	1.5
Pulse width FWHM (ns)	1.2	1.3
H atoms per cm^3 ($\times 10^{22}$)	5.15	5.15
C atoms per cm^3 ($\times 10^{22}$)	4.69	4.69
Electrons per cm^3 ($\times 10^{23}$)	3.33	3.33
Density (g/cm^3)	1.023	1.023

b. Geometric configuration. The TTC system is designed as an array of many small scintillator tiles, where granularity and geometric configuration are essential parameters. In the MEG II experiment, the pixelated timing counter was designed with a high granularity, which enhanced the overall time resolution through multiple measurements. The entire timing counter successfully completed a test run incorporating electronic components, cooling systems, bias voltage supply, and calibration systems. During the test run, a resolution of less than 40 ps was achieved, with 6–10 hits [86]. For MACE, the coincidence of two or three adjacent scintillator tiles by a tilt design can further improve the time resolution while reducing the level of accidental coincidence events. The specific design details are discussed below.

c.Spatial resolution. An improved spatial resolution in TTC can aid track finding in the CDC by providing an approximate yet known hit position. While the CDC can detect hits on wires, the precise spatial locations through which tracks pass are not directly known. TTC partially compensates for this lack of information at the ends of the tracks. The spatial resolution is influenced by the size of the scintillator tiles; smaller tile sizes enhance the spatial resolution, but this increase comes at the expense of a greater number of channels and increased technical complexity, without a significant improvement in physical performance. Furthermore, the requirement for time resolution constrains the scintillator tile size to less than 50 mm, which is sufficient for providing an initial seed for track finding in the CDC. Consequently, a tile size of 50 mm was deemed to be appropriate.

d.Rate capability. MACE will be exposed to a muon beam with a flux of 10^8 μ^+/s, resulting in a total event rate in the Tiled Timing Counter (TTC) of a similar magnitude. Smaller scintillator tile sizes can help reduce the pile-up events. With scintillator tiles sized $\mathcal{O}(50\text{ mm})$ arranged in a tilting design, there are approximately 10,000 tiles in total, including at least 3,000 scintillator tile sets for multiple-tile coincidences. Consequently, the physical event rate for a single tile set was estimated to be approximately 3×10^4/s, leading to a pile-up event rate of approximately 3×10^4/s in the entire TTC system, assuming a resolving time of 5 ns. This accounted for only 300 ppm of the total physical event rate. Additionally, background particles in the experimental hall led to fake events in the TTC. A conservative estimate of the background hit rate is 10^4/s per tile, which results in an accidental two-tile coincidence event rate of approximately 3×10^3/s across the TTC system. This only corresponds to a physical event rate of 30 ppm. In conclusion, the rate capability satisfies the necessary criteria.

e. Detection efficiency. The detection efficiency of TTC affects the total efficiency of the MMS. The TTC detection efficiency is contributed both intrinsically and from the geometry. The plastic scintillator has good intrinsic detection efficiency for Michel's positrons and electrons, and the main efficiency loss is due to the geometric design. The TTC system should cover the entire barrel to ensure its acceptance. Furthermore, the tilt-tile design also affects the efficiency of the charged tracks of different signs, which will be discussed below.

Table 7 Geometric parameters of the tiled timing counter system

Parameter	Value
Layers along the z-axis	60
Tiles per layer	163
Total number of tiles	9780
Scintillator size (mm^3)	$50 \times 30 \times 5$
Tilt angle (°)	30
Total length (mm)	1800
Radius (mm)	480
Geometric acceptance	88.2%

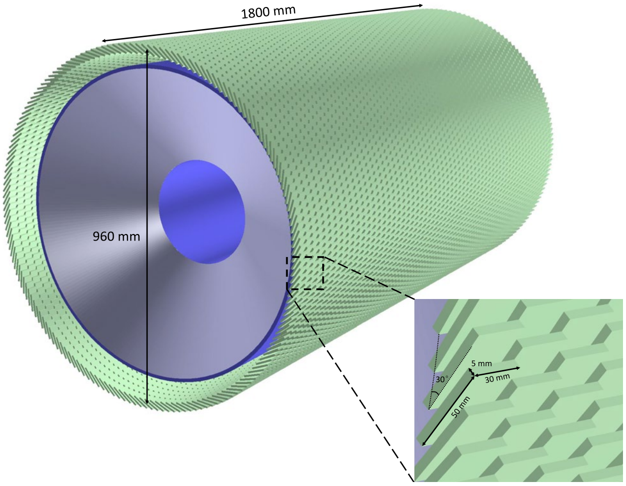

Fig. 26 (Color online) Perspective and zoom-in view of the tiled timing counter (green)

7.3.2 Conceptual design

Figure 26 illustrates the geometric design of TTC. Each unit in this design measured 50 mm × 30 mm × 5 mm. A total of 9,780 units were organized in an overlapping arrangement across 60 layers (along the z-axis) and 163 columns (along the azimuthal direction) at a tilt of 30°. This overlapping configuration facilitates two-to-three-tile coincidence detection, ensuring that most high-momentum charged tracks traverse at least two scintillators while minimizing the occurrence of accidental coincidences from the background particles. Compared to a design with two complete layers of scintillators, this approach reduces the number of channels and cabling complexity. The TTC configuration has a radius of 480 mm and total length along the z-axis of $60 \times 30\text{ mm} = 1.8$ m. Consequently, the geometric acceptance of the TTC system was calculated as 88.2%, which

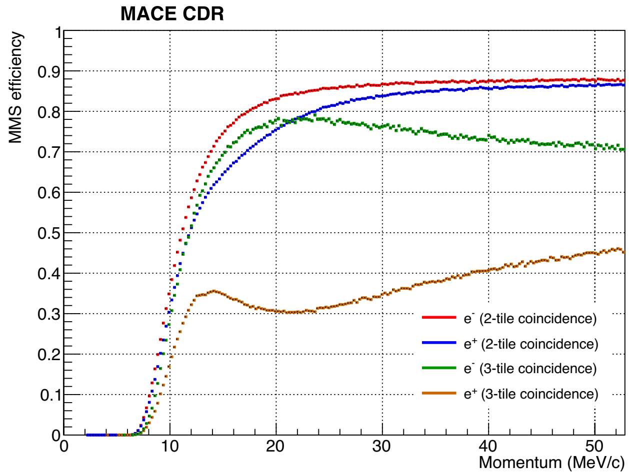

Fig. 27 (Color online) MMS tracking efficiencies for electrons and positrons at two different TTC coincidence thresholds. Reconstruction efficiencies are not included

is consistent with that of the CDC. The parameters can be summarized by Table 7.

The tilt of each scintillator tile was intentionally oriented in the direction where the largest surface was more perpendicular to the electron track. Because the TTC system is placed in an axial magnetic field, electrons and positrons are bent in different directions. This tilt design naturally favors tracks that are more perpendicular to the large surfaces of the tiles, resulting in the positively tilted layers being more sensitive to electrons, which are the decay products of antimuonium and of particular interest to MACE. Differences in detection efficiency can be observed in the efficiency curves shown in Fig. 27, and the results are discussed in Sect. 7.4. The 30-degree tilt angle was calculated to balance the spacing between adjacent tiles within a single layer and the overlap of their projected areas.

Silicon photomultipliers (SiPMs) are known for their excellent time resolution and photon detection efficiency (PDE), making them well suited for MACE timing counter. Two SiPMs are attached to each scintillator tile at its two smallest faces (measuring 10 mm × 100 mm). This double-ended readout reduces the timing bias owing to the different hit positions and improves the single-tile time resolution. The Hamamatsu S13360 series MPPC was considered because of its ~ 100 ps time resolution and 40–50% PDE [87]. The packaging scheme and reflector type of TTC scintillators are still under investigation. In conclusion, the TTC geometry and detector design are expected to satisfy the requirements of MACE.

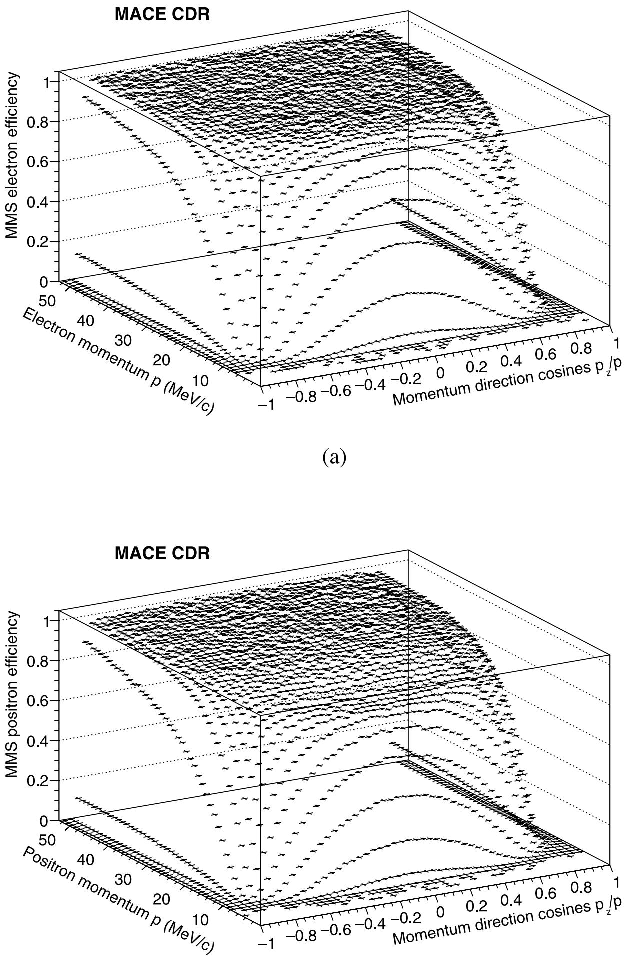

(a)

(b)

Fig. 28 MMS tracking efficiencies for electrons (**a**) and positrons (**b**) with 2-tile TTC coincidence. Reconstruction efficiencies are not included

7.4 Performance

In this section, we present the simulation results of the detection efficiency of the MMS system. As discussed earlier, the MMS consists of CDC and TTC, and their geometric acceptance is consistent with the design. A noteworthy characteristic of the TTC design is the overlapping arrangement of scintillator tiles, which results in differing expected coincidence probabilities for electrons and positrons owing to the influence of a magnetic field. In the fast simulation, we selected tracks that had a number of hit cells equal to or greater than the number of CDC layers and that hit at least two or three TTC tiles. The full track reconstruction algorithm was not applied; therefore, the results should be interpreted in terms of the geometric effects on the tracking efficiency. Complete tracking efficiency can be considered as the geometric efficiency multiplied by the reconstruction efficiency. Electrons and positrons with isotropic momentum ranging from 1 keV/*c* to 52.8 MeV/*c* were generated from the center of the MMS, and the efficiencies for events with 2-tile or 3-tile TTC coincidences are shown in Fig. 27, respectively. The direction-dependent tracking efficiencies for electrons and positrons are shown in Fig. 28.

As expected, at the 2-tile coincidence threshold, the efficiencies for both electrons and positrons increase with momentum, although the increase in positron efficiency is slower and consistently lower than that of electrons. In the high-momentum region, the electron and positron efficiencies converge at maximum values of 88% and 86%, respectively, and are limited mainly by geometric acceptance.

For the 3-tile coincidence threshold, while the positron efficiency remains lower than that of the electron, the efficiencies are no longer monotonic with respect to momentum. For electrons, the 3-tile efficiency initially increases, reaching a maximum around 20 MeV/*c*, before gradually decreasing as the momentum increases further. This initial increase can be attributed to the increasing gyration radius, whereas the subsequent decrease is due to the greater track curvature. If the track curvature becomes too large, an electron track is more likely to traverse two TTC tiles instead of three because of the overlapping design. In the case of positrons, the trend is similar during the initial increase, but the situation reverses at high momentum. The decrease at a high momentum can be attributed to a reason similar to that of electron. The decrease in efficiency observed between 10 and 20 MeV/*c* is likely because the track gyration radii match well with the TTC radius and tilt angle, leading to an optimal momentum at which tracks align with the TTC tile orientations, resulting in a lower coincidence probability.

MMS is responsible for tracking electrons and positrons from the decays of muon, muonium, or antimuonium. The decay momenta ranged from 0 to 53 MeV/*c*, with the majority falling within the high-momentum region. The momentum spectra of electrons from the antimuonium decay and positrons from the muon decay in the MMS are shown in Fig. 29. The momentum spectra for electrons and positrons are slightly different owing to differences in the tracking efficiency, as discussed earlier. According to the simulation results, the tracking efficiency (excluding the reconstruction efficiency) for Michel electrons and positrons was 84.6% and 81.8%, respectively. These efficiencies are close to the full geometric acceptance because efficiency losses are mostly contributed by the low-momentum region, where the Michel spectrum is low. Assuming a reconstruction efficiency of approximately 80%, the effective tracking efficiency for Michel electrons and positrons is approximately 68% and 65%, respectively, as listed in Table 8.

Generally, the 2-tile TTC coincidence is suitable when the accidental coincidence rate is not excessively high, allowing for an optimal detection efficiency. Meanwhile, the 3-tile coincidence can be employed if accidental coincidences need to be suppressed, although it results in reduced positron efficiency, while the electron efficiency remains reasonable. In conclusion, the MMS design was optimized for resolutions and tracking efficiencies, and the system allowed for adjustable coincidence configurations

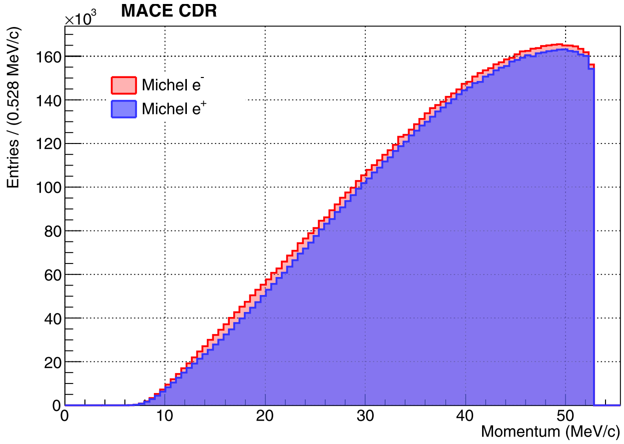

(a)

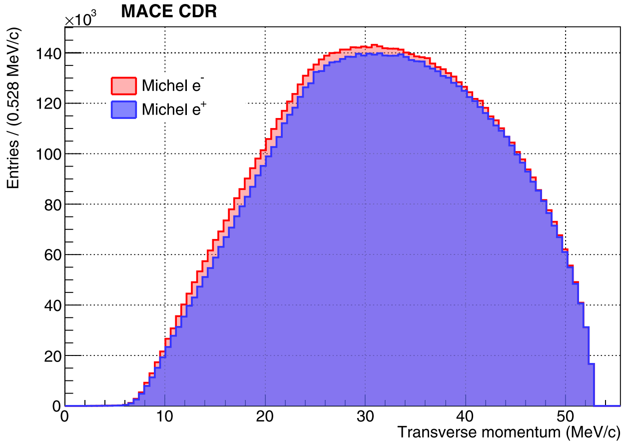

(b)

Fig. 29 (Color online) Michel positron momentum spectrum in MMS without momentum resolution. **a** Momentum spectrum; **b** Transverse momentum spectrum

Table 8 Tracking efficiency of MMS

Track	Efficiency		
	Geometry	Reconstruction	Total
	$\varepsilon_{\mathrm{MMS}}^{\mathrm{Geom}}$	$\varepsilon_{\mathrm{MMS}}^{\mathrm{Recon}}$	
e^- from $\overline{\mathrm{M}}$ decay	84.6%	~ 80%	68%
e^+ from μ^+ decay	81.8%	~ 80%	65%

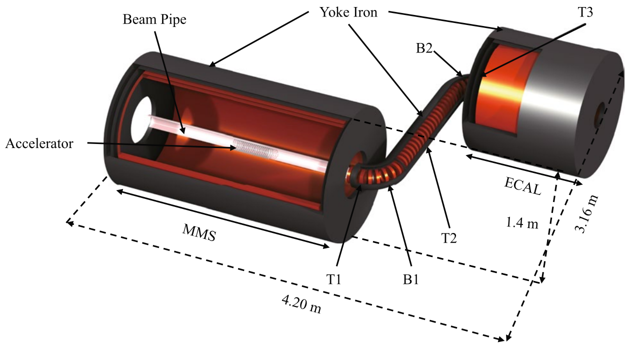

Fig. 30 (Color online) Concept of the MACE positron transport system (PTS). The outer gray shell represents the iron yoke, while the interior copper-colored component denotes the solenoid. Key elements and overall dimensions are indicated in the picture

for different background rates. The conceptual design of the MMS system can meet the requirements for the physical goals of MACE.

8 Positron transport system

The physical design of the MACE positron transport system (PTS) comprises two main components: an electrostatic accelerator and a solenoid system. This system was designed to transport low-energy atomic positrons produced in antimuonium decays from the target region to the microchannel plate (MCP) to detect signals. The design aims to minimize the background noise from high-energy particles, such as Michel positrons, to the greatest extent possible. In addition, a position-mapping algorithm was developed to reconstruct the 2D position of the low-energy positron.

8.1 Magnet and transport solenoid

As shown in Fig. 30, the solenoid system in the PTS has three components: the Michel electron magnetic spectrometer (MMS) solenoid, transport solenoid, and electromagnetic calorimeter (ECAL) solenoid. The MMS solenoid is cylindrical in shape, 2400 mm long, and 700 mm in radius, designed to bend charged tracks and confine low-energy positrons, surrounded by a 50 mm thick iron yoke. The S-shaped solenoid transports slow positrons to the MCP in the middle of the ECAL. The transport solenoid comprises five sections: three straight solenoids, T1, T2, and T3, and two toroid solenoids, B1 and B2, make up the system. Each solenoid had identical coils with a length of 30 mm, inner diameter of 120 mm, and outer diameter of 180 mm. T1 and T3 are 150 mm long and T2 is 1314.5 mm long. The arcs of B1 and B2 are each 90°, with a radius of 250 mm and opposite rotation directions, forming an S-shape. The transport solenoid is covered by a 30 mm thick iron yoke and connects the centers of the MMS solenoid and ECAL solenoid. The cylindrical ECAL solenoid is 1200 mm in length and 650 mm in radius and is surrounded by a 50 mm thick iron yoke, which can constrain the positrons after transportation.

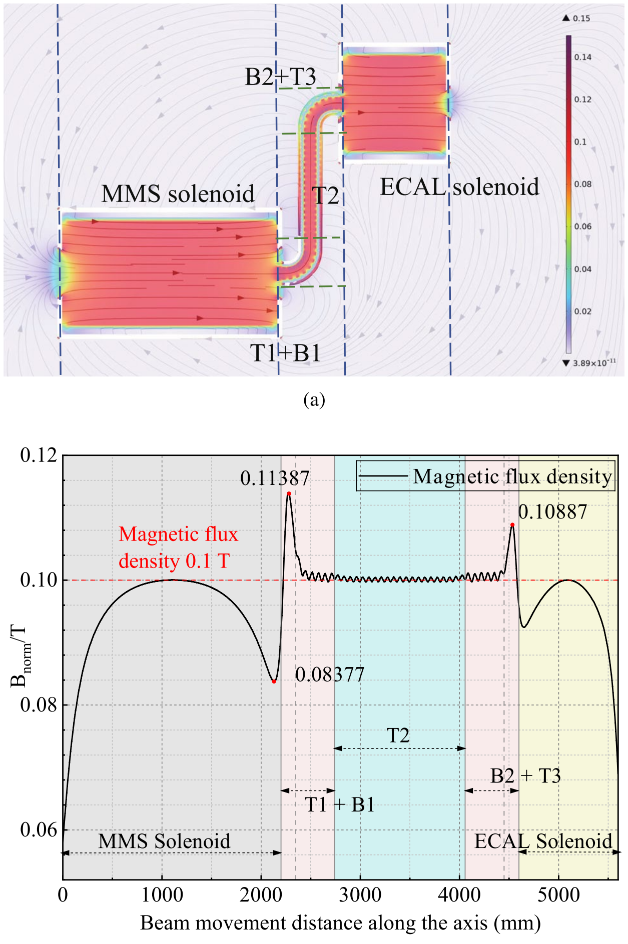

(a)

(b)

Fig. 31 (Color online) The magnetic field distribution. **a** The distribution of the overall magnetic field across the cross section of the PTS simulation. Magnetic field lines are also shown. The corresponding regions in (b) have been marked in the figure; **b** Distribution of the magnetic field along the central axis of the PTS solenoid. The reference line of 0.1T represents the ideal case

The S-shaped transport solenoid was designed to reduce the background signals. Low-energy positrons with small magnetic stiffness can be considered to follow the magnetic field lines during transport. In contrast, high-energy particles, which have greater magnetic stiffness, tend to collide with the solenoid at S-shaped turns, effectively acting as a momentum selector. In addition, as positrons are transported to the MCP, their transverse spatial coordinates and impact times can be measured. A position-mapping algorithm can then be employed to reconstruct the decay positions of particles in the target region. In this way, the PTS acts as a link between the spatial and timing information of events in the PDS and MMS, demonstrating how the MMS, PTS, and PDS collaborate to coincide with antimuonium events.

To transport positrons with a high spatial resolution, it is crucial to maintain a consistent magnetic field in the transportation region of the PTS. This requires that the magnetic fields produced by the MMS solenoid and ECAL solenoid have a magnitude similar to that of the transport solenoid, as this affects the magnetic field within the transport solenoid. In our experiment, we used a yoke to shield against the magnetic field interference between different regions. We then controlled the magnetic field and its distribution by adjusting the current through various components.

The magnetic field distribution is shown in Fig. 31. The arrangement of the magnetic flux lines confirms that the magnetic field is uniform. By adjusting the current in the different solenoids, we could control the magnetic field to approximately 0.1 T. The decrease in the magnetic field at the end of the MMS was attributed to the fringe field of the solenoid, whereas the increase was due to the connection between the MMS yoke and T1. The interaction between the MMS and T1, along with the enhancing effect of the yoke, contributed to the magnetic field reaching 0.114 T in this region. The same applies to T3; however, because the ECAL solenoid is smaller than the MMS solenoid, the edge effect is less pronounced. Because the maximum magnetic field intensity caused by the edge effect does not exceed the predetermined 12%, and the affected region is very short, this edge effect has little impact on the overall transmission performance according to the simulation results.

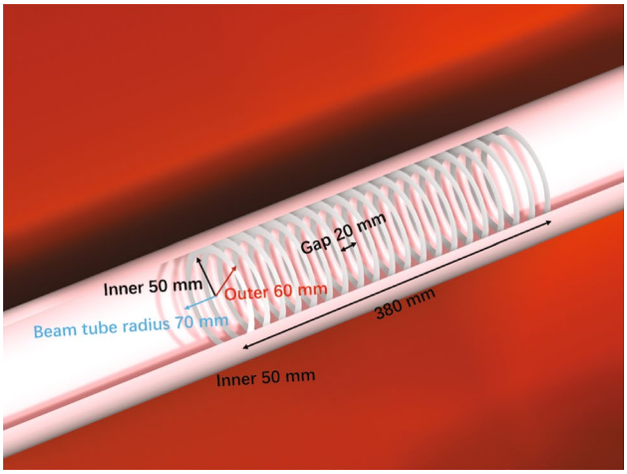

Fig. 32 (Color online) Concept of the electrostatic accelerator

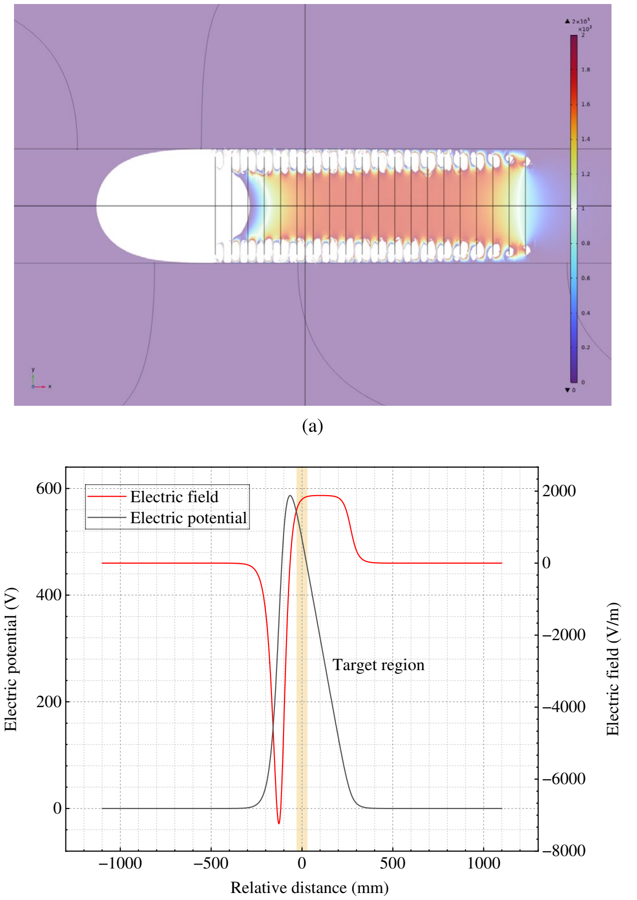

(a)

(b)

Fig. 33 (Color online) Accelerator electric field distribution. **a** Simulated electric field distribution along the axis of the electrostatic accelerator where the blank area represents the region with the reversed electric field; **b** The electric potential distribution in the axial beam direction. The orange-yellow shaded area is the location of the target area, the black line is the electric field in the beam direction, and the red line is the electric potential

8.2 Electrostatic accelerator

Signals in MACE are low-energy positrons produced by antimuonium decays. The kinetic energy spectrum is shown in Fig. 4c. The momenta of the positrons are isotropic, which means that they cannot be directed solely by a magnetic field toward the MCP. Additionally, their kinetic energy, typically a few tens of eV, is insufficient to activate MCP. However, accelerating the positrons along the axis by a few hundred volts can address both these challenges.

In this design, an electrostatic accelerator is used for acceleration. This device generates a uniform electric field in the acceleration section, enhancing the precision of the position mapping. Unlike typical designs that place the accelerator outside the beam pipe, the MACE electrostatic accelerator is positioned inside the beam pipe, which will be

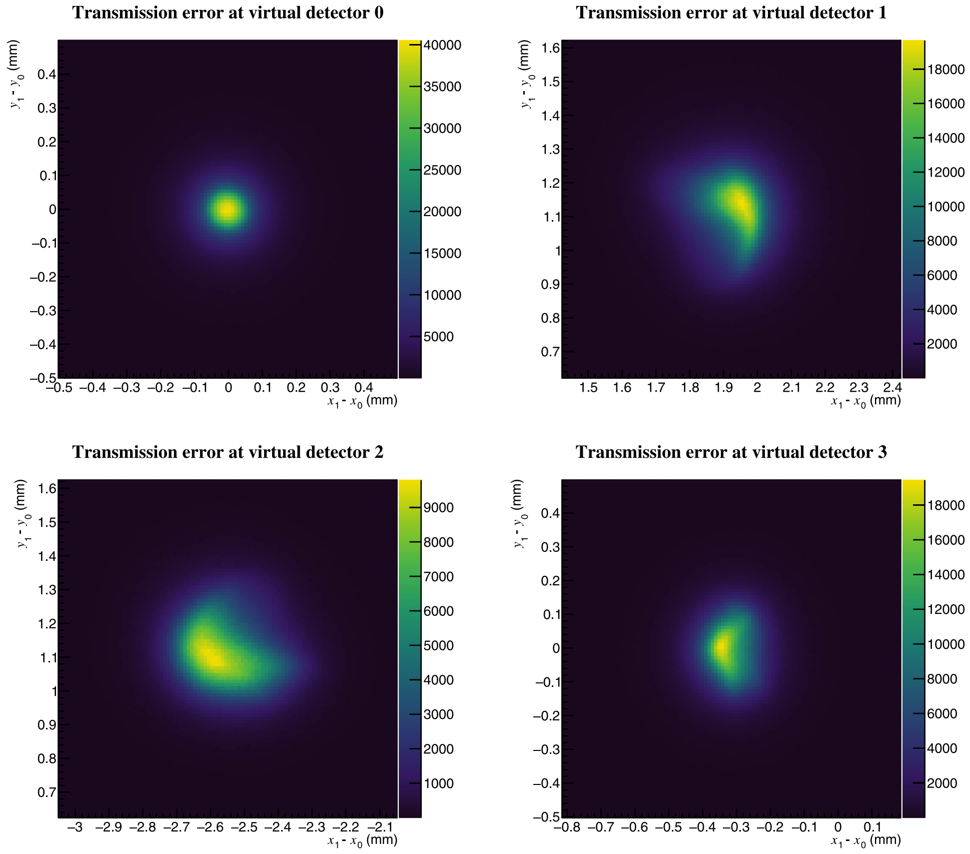

Fig. 34 (Color online) The relative displacement of the positron

grounded to prevent the accumulation of charge on it owing to this high-intensity but low accelerator energy situation.

As shown in Fig. 32, the electrostatic accelerator of a PTS consists of multiple circular thin sheets arranged at equal distances. It was situated within the beryllium beam tube along the axis of the MMS solenoid. The electrostatic accelerator has a length of 380 mm, an inner radius of 50 mm, and an outer radius of 60 mm, enveloping the 60 mm × 50 mm × 50 mm target region. The upper end of the accelerator was positioned 110 mm front from the center of the MMS solenoid and the target region. The highest potential is 780 V, the distance between adjacent accelerator sheets is 20 mm, and the potential difference is 41.6 V. The resulted electric field distribution is ploted by Fig. 33.

8.3 Performance

After the positron was transported to the ECAL solenoid, its transverse position was measured by the MCP. The transverse projection of the positron can be reconstructed using the solenoid position mapping algorithm. The distributions of the difference between the coordinates of the positron transported to the MCP and the coordinates of the antimuonium decay position in the Geant4 simulation results are shown in Fig. 34. In the plot, x_1 and y_1 represent the coordinates of the particle hitting the virtual detector; x_0 and y_0 represent the initial coordinates of the particle; and the horizontal and vertical coordinates x and y in the picture are the differences between the two, indicating the offset of the particle during transportation, not the beam spot. Virtual detectors 0 to 3 represent the positions of the virtual detectors in the beam direction: after acceleration, after B1, before B2, and in the middle of the MCP. The average values of the horizontal and vertical coordinates represent the change in relative position during particle transportation. The root mean square represents the spatial resolution of particle transportation, measuring 0.088(1) mm × 0.102(1) mm, and the offset of the transport was 0.315(1) mm in the x direction and 0.003(1) mm in the y direction. Our simulation included 10^7 initial incident particles. The signal transmission efficiency was 65.8%, as calculated from the ratio of events detected by each detector to the number of initial incident particles.

Beam vertical plane position mapping was performed on the 2D position detected by Virtual Detector 3. The position mapping of the positrons before and after transportation is shown in Fig. 35. In the analysis, the horizontal and vertical coordinates of the particles were considered separately. The coordinates of the transported particles were highly correlated with the corresponding initial coordinates, whereas the calculated coordinates of the transported particles had a low correlation with other initial coordinates, such as (x, y_0), with a correlation coefficient of less than 0.01. Therefore, it

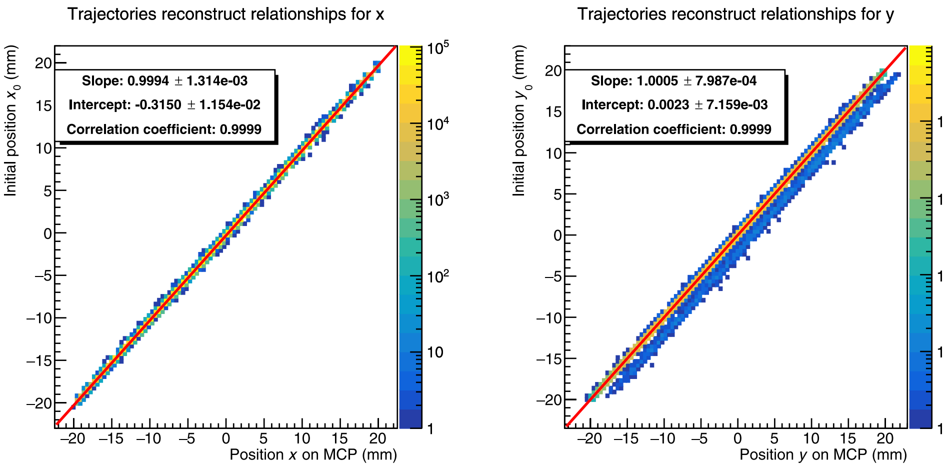

Fig. 35 (Color online) PTS position mapping analysis, the coordinates before transportation are marked as (x_0, y_0), and after transportation are marked as (x, y). The red line is the fitting line, and the parameters are given in the legend

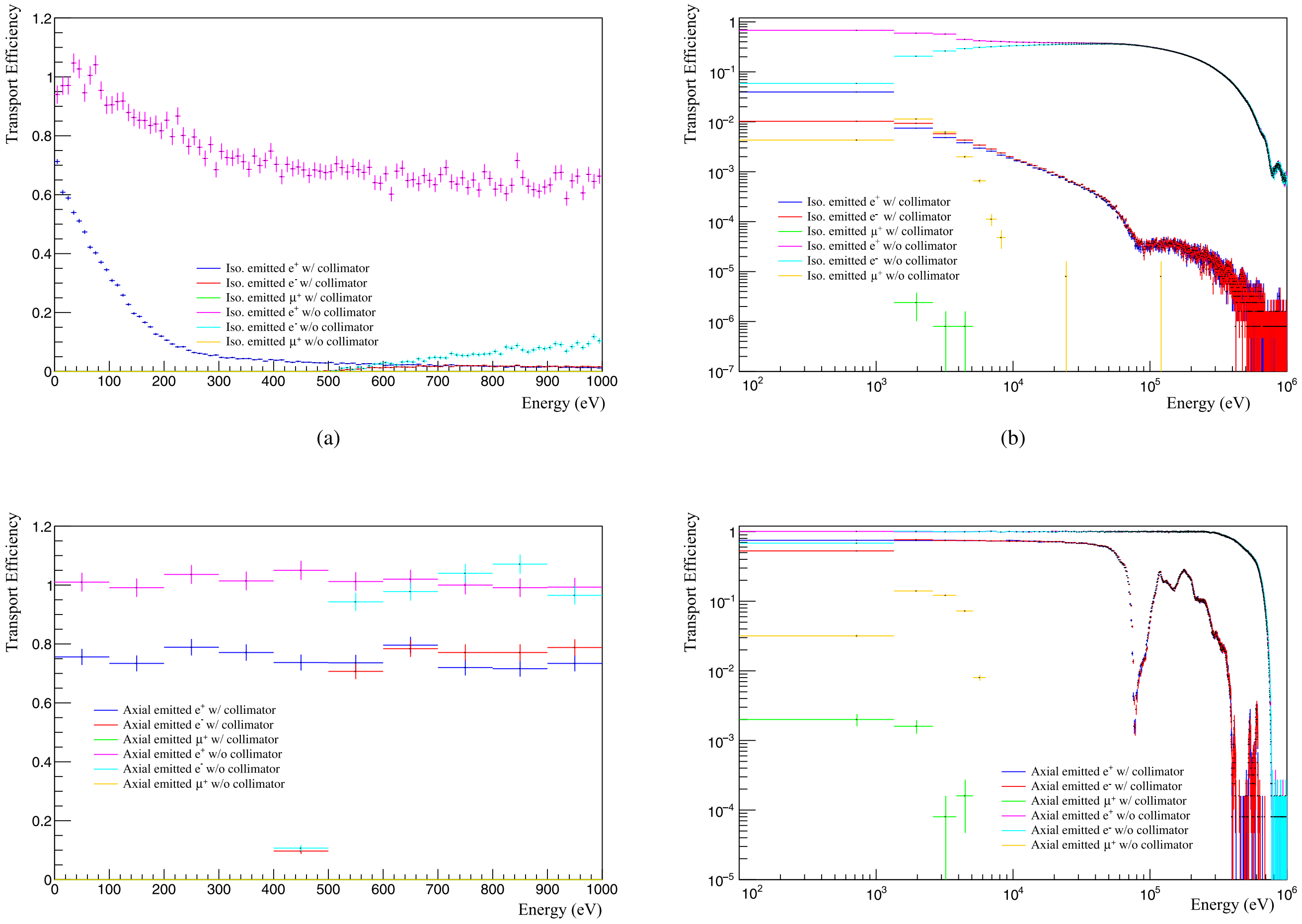

(a) (b)

(c) (d)

Fig. 36 (Color online) Simulation results of signal transmission efficiency for different charged particles at different energies with and without a collimator. **a** The simulated particle has an isotropic initial momentum and the upper limit of the simulated energy is 1 keV; **b** The simulated particle has an isotropic initial momentum and the upper limit of the simulated energy is 1 MeV; **c** The simulated particle has an initial momentum in the axial direction and the upper limit of the simulated energy is 1 keV; **d** The simulated particle has an initial momentum in the axial direction and the upper limit of the simulated energy is 1 MeV can be assumed that the position mapping function before and after the transportation of the positron has a linear relationship, and the slope is approximately 1, with almost no stretching, and only a partial offset in the vertical beam direction. This offset is consistent with the offset shown in Fig. 34; therefore, in the current simulation stage, it can be considered that the coordinate transformation before and after the positron transportation is only a position offset, with an offset of 0.315 mm in the x direction and 0.003 mm in the y direction.

Because low-energy positrons are produced over the entire target region, the acceleration potential and flight distance vary. Therefore, the overall flight time, that is, the time it takes for the positrons to be transported from the target region to the MCP, is approximately 322.4 ns, and the flight time width is 6.9 ns.

As shown in Fig. 36, the PTS system simulates the presence or absence of a collimator and differently charged particles e^+, e^-, μ^-, μ^+, π^+, and π^-. Because π^+ and π^- promptly decay and cannot be transported to the MCP, they are not shown in the figure, and the number of μ^- and μ^+ events is too small, so only μ^+ is given as a reference. It can be seen that the transmission efficiency is very low for charged particles other than electrons or positrons, and the PTS system is highly energy-selective. As the high-energy charged particles in MACE are mainly positrons from muon decay and their secondaries, the momentum direction can be regarded as isotropic. The following figure can be used to refer to the PTS system's ability to select the momentum.

It can be seen that the transmission efficiency of the particles decreases significantly when the collimator is present, especially for high-momentum particles, and the filtering capability of the collimator is outstanding. For positrons with small initial momenta (initial momentum ≤ 100 eV), the transmission efficiency was $\sim 75\%$. At this kinetic energy, the transmission efficiency of the electrons is extremely low because the momentum cannot overcome the reverse electric field. Low-energy μ^+ cannot be transported because of its limited lifetime, so the transmission efficiency is also extremely low. When the initial kinetic energy is greater than 500 eV, the kinetic energy of electrons can overcome the electric field of the electrostatic accelerator, and the transmission efficiency curves of the positrons and electrons gradually approach each other. The initial momentum of μ is sufficient to allow some of them to reach the MCP before decay; however, the maximum transmission efficiency does not exceed 1%. When the initial kinetic energy continued to increase, the transmission efficiency of μ dropped to 10^{-6} at 20 keV, and the transmission efficiency of electrons and positrons also decreased to 1%.

In summary, the physical design of the PTS effectively satisfied the requirements of the MACE system. The PTS achieved a high spatial resolution of 0.088(1) mm × 0.102(1) mm, showing excellent transmission capability. In terms of background suppression, the primary sources of the background are Michel positrons from muonium decay and muons in the beam. When the kinetic energy exceeds 20 keV, the transmission efficiency for Michel positrons decreases to 10^{-2}, whereas that for muons is 10^{-6}. Consequently, the current design demonstrated robust momentum selection capabilities, maintaining a signal transmission efficiency of 65.8%. The next step involves exploring the engineering implementation of this design.

9 Positron detection system

9.1 Microchannel plate

Nowadays, MCP, as a type of electron multipliers based on the secondary electron emission, has been widely used in high energy physics [82, 88] and other relevant fields [89–96] due to its excellent spatial and time resolution. MACE, as an experiment searching for a rare process beyond the standard model, also uses MCP as a part of the positron detector, expecting to better suppress background events using precise position and time information. After the decay of antimuonium, positrons are transported along the solenoid to the PDS and annihilate within the material once it hits the MCP, producing a pair of 511 keV gamma rays, which will soon be detected by the electromagnetic calorimeter. Before annihilation, some initial free electrons are produced by the ionization of the positron, amplified inside the channels of the MCP, and finally detected. The energy of the positrons to be detected is several hundred electron volts and the required time resolution is approximately $100 \sim 200$ ps. The spatial resolution of the MCP depends mainly on the distance between channels, which is typically < 10 μm. The strict requirement of time resolution excluded most of the mass-produced MCPs, so further R&D is needed. To make the design and optimization more convenient, a simulation program for MCP has been developed, which is still independent and can be combined into the MACE software system in the future. However, we still face challenges before the combination, such as the heavy burden of computing the electron avalanche.

The simulation of electron multipliers, such as the MCP, has always been difficult. On the one hand, the millions of electrons produced in the electron avalanche will definitely be a challenge for computing if they are simulated just track-by-track. However, the precision of the simulation cannot be guaranteed if phenomenological models are used because of the necessary approximation and simplification. Furthermore, the mechanism of secondary electron emission cannot be described accurately because of the large uncertainty in the dynamics of particles and the fluctuation

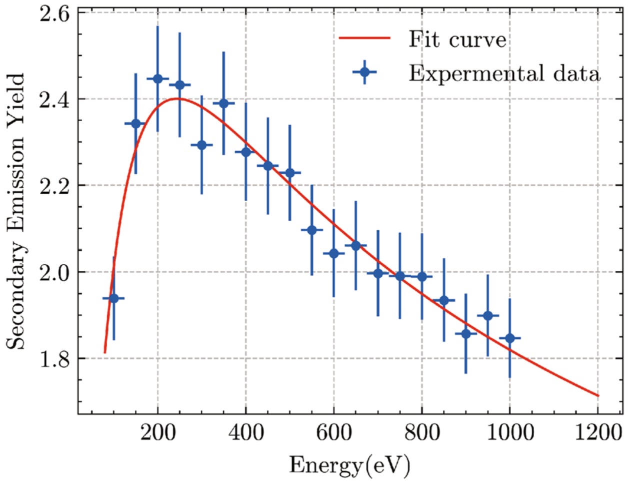

Fig. 37 (Color online) The measured SEY of lead glass overlaid with the best fit

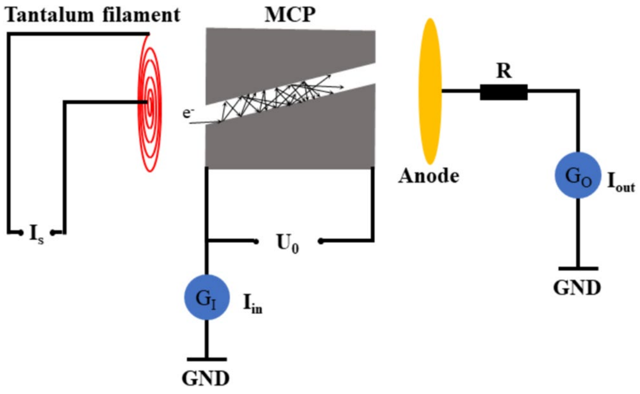

Fig. 38 (Color online) The schematic diagram of the device used to measure the MCP gain

of statistics. Thus far, much effort has been put into the simulation of electron multiplier devices worldwide based on multiple models [97–100]. Several commercial software programs have been developed for the general simulation of electron multipliers, including CST Studio Suite™ [101] and SIMION™ [102]. However, they are not so easy to be combined into the software system of MACE and difficult to be modified according the real case of the experiment, so that we developed an open-source software based on Geant4 [103] using Furman model [104].

The implementation of the Furman model into Geant4 can be found in detail in Ref. [105, 106]. It is difficult to obtain the real secondary electron yield (SEY) and the energy spectrum. In the simulation, the SEY distribution with respect to the energy of the incident electrons for lead glass was obtained by fitting the measured data, as shown in Fig. 37.

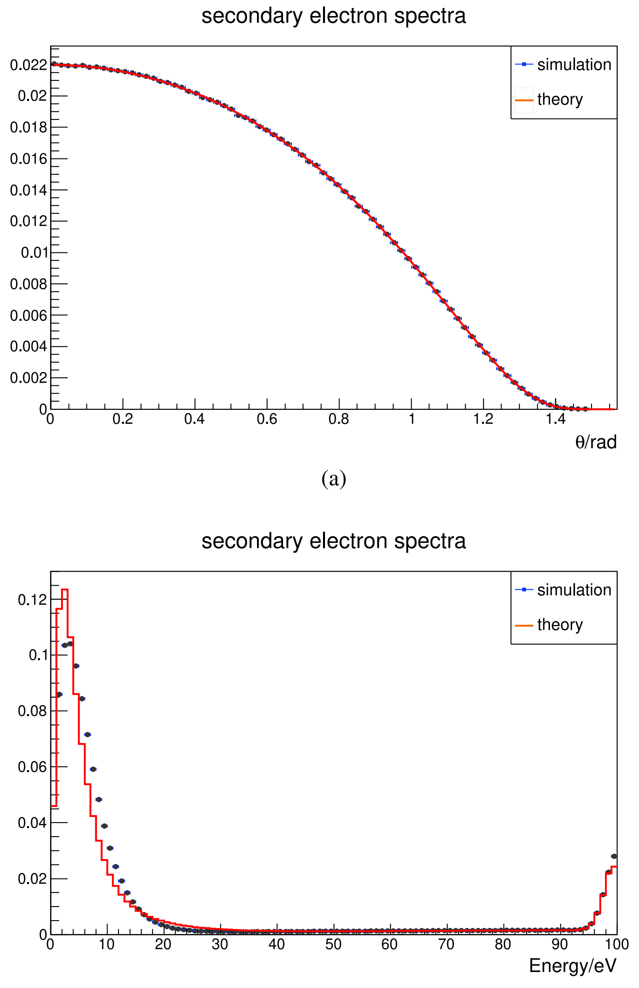

(a)

(b)

Fig. 39 (Color online) The angular (**a**) and kinetic energy distribution (**b**) of the secondary electrons produced by an incident electron with 100 eV energy. The red solid line is the theoretical prediction and the black points with error bars are the simulation results

The MCP gains at various applied voltages were measured using the device shown in Fig. 38. As illustrated in Fig. 38, a tantalum filament, the MCP to be measured, and an anode were placed sequentially inside a vacuum device. A voltage of U_0 is applied to the MCP. When the system is working, a current I_s flows through the tantalum filament, and some of the electrons emitted from the filament enter the input pore of the MCP, of which the input current I_{in} is measured by the galvanometer G_I. After the avalanche amplification in the MCP channel, the output current I_{out} is measured by the anode and the MCP gain at the applied voltage is then calculated by

$$G = \frac{I_{\mathrm{out}}}{I_{\mathrm{in}}}. \tag{34}$$

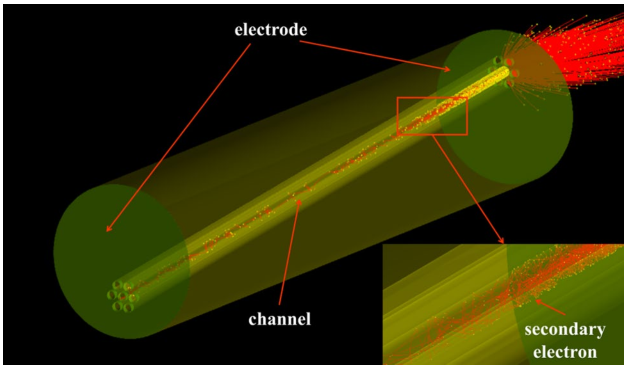

Fig. 40 (Color online) Simulation events using the simple MCP model

The energy spectrum of the secondary electrons for lead glass is adjusted from the measured spectrum of other materials and iterated in the simulation to approximate reality. Figure 39 shows the angular distribution and kinetic energy distribution of the secondary electrons when the energy of incident electron is 100 eV.

After the implementation of the secondary electron emission process, it will be brilliant to study the amplitude and shape of the signal when a certain electron from the initial ionization enters a channel because the response of each channel will be the same or at least similar to each other. Once the signal has been known in detail, the response of a single electron can be accessed by simple sampling so that the response of the entire MCP can be simulated quickly and precisely. We built a simplified geometry of MCP with only seven channels for the simulation of single-electron response, considering the complexity of constructing an MCP with millions of channels, as shown in Fig. 40. Limited by the rendering power of the computer, only 5000 tracks were drawn in this figure. However, amplification of the secondary electrons can be clearly observed.

To further validate our simulation, we simulated the gain of the two MCPs versus the applied voltages and compared them with the measured results. The geometries of #1 and #2 MCP were established in Geant4 based on actual measurements and are provided in Table 9. In the simulation, the kinematic information of all the particles that are able to reach the exit of the channel is recorded without considering the detection efficiency, fluctuation, or other relevant issues of the readout system; thus, the MCP gain is simply calculated by dividing the number of electrons at the exit by the number of electrons shot toward the MCP. The two pieces of MCPs are simulated at different applied voltages from 700 V to 1200 V with a step of 100 V using the same SEY and energy spectra of the secondary electrons. For each voltage, the gain was simulated 1000 times with random primary incident electrons, and the average was determined to be the gain at this voltage. The gains with respect to the voltages are shown in Fig. 41a and b.

Table 9 Geometric parameters of the two pieces of MCPs simulated in this work

Parameter	#1 MCP	#2 MCP
MCP diameter (mm)	25	24.8
MCP thickness (mm)	0.42	0.48
Pore diameter (μm)	10	6
Tilt angle (degree)	12	5.5
Body resistance (MΩ)	84	90
Input current (pA)	107	162

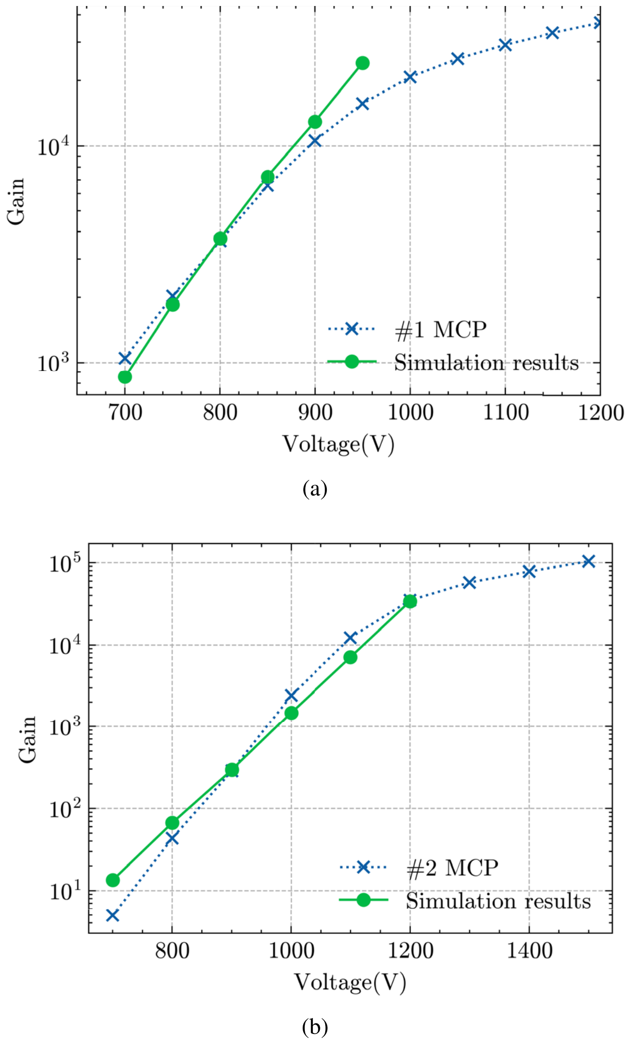

Fig. 41 (Color online) The gain of two MCPs versus applied voltage. The blue "×" markers denote the experimental measurements and the green points denote the simulated results. **a** #1 MCP **b** #2 MCP

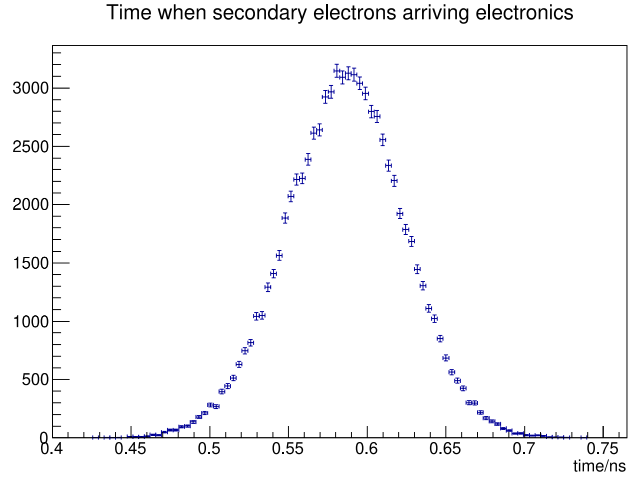

Fig. 42 (Color online) Time distribution of secondary electrons received by electronics. The horizontal axis denotes the time after the initial electron enters the channel

According to the simulation results shown in Fig. 41a and b, the gain will increase exponentially with increasing applied voltage, which is consistent with the experimental measurements and other studies [107], whereas the measured gain is obviously lower than the simulated result and tends to stabilize to a constant value when the applied voltages are sufficiently high because the multiplication is suppressed by the saturation effect [108, 109] which is not considered in the simulation at present. The distribution of the time when the secondary electrons arrive at the electronics for #2 MCP is shown in Fig. 42.

The simulation program for electron multipliers such as MCP has been summarized into an independent software named "MCPSim" [105]. In the future, a new MCP will be developed to satisfy the requirements of MACE. MCPSim will be used in development and optimization. Meanwhile, the simulation of MCP will be implemented in the software system of MACE with more proper consideration of the saturation and space charge effects.

9.2 Electromagnetic calorimeter

9.2.1 Overview

The primary purpose of the electromagnetic calorimeter (ECAL) is to enable the annihilation γ-rays with positron hits on the MCP and the rejection of various backgrounds. ECAL is expected to discriminate the annihilation signal from the background and retain all event information as much as possible. This leads to the following baseline performance specifications for the ECAL:

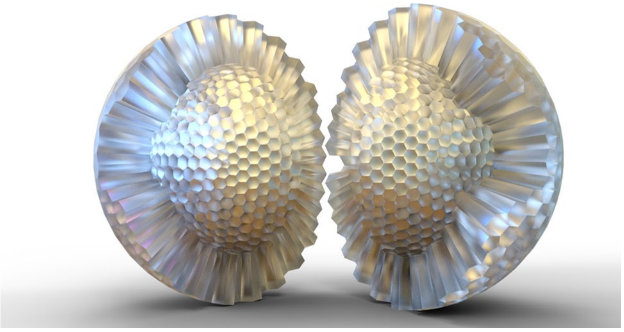

Fig. 43 (Color online) 3D rendered image of the ECAL geometry [111]

- An energy resolution of ~ 10% at 0.511 MeV to perform precise energy reconstruction, rejecting the contribution of natural backgrounds.
- A spatial resolution of ~ 1 cm to reconstruct the tracks of two back-to-back γ-rays, rejecting accidental coincidence.
- A timing resolution of ~ 1 ns to ensure that the energy deposits in ECAL modules are in time with MCP response.
- A geometrical acceptance of ~ 95% to prevent leakage of annihilation events.

In the next two sections, we first introduce the geometrical layout, module assembly, and event reconstruction of the ECAL. Then, simulation studies were conducted to estimate the performance of M-to-$\overline{\mathrm{M}}$ signal. Moreover, a proposal for the MACE Phase-I experiment, which consists of the ECAL and an inner tracker system for other muon cLFV process searches, will be further introduced in Sect. 13.

9.2.2 Conceptual design

To meet the aforementioned requirements (e.g., excellent energy resolution, high detection efficiency, and good geometrical acceptance), we proposed a Goldberg polyhedron geometry design of the ECAL (see Fig. 43). The Goldberg polyhedron consists of pentagons and hexagons, with every three faces meeting at the same vertex [110]. It is similar in appearance to a sphere as an inpolyhedron and possesses icosahedral rotational symmetry. A Class I GP(8, 0) Goldberg polyhedron geometric layout was introduced. It consists of 642 faces, including 12 regular pentagons and 630 irregular hexagons, which can be categorized into nine types. The modules created from the different types of faces were identified as Type-PEN and Type-HEX (01–09). There were 19 modules at the beam entrance and one module at the exit removed, resulting in

Table 10 Properties of BGO, CsI(Tl), and LYSO(Ce) scintillation crystal [37, 113]

Parameter	ρ (g/cm^3)	X_0 cm	R_{M} (cm)	dE/dx (MeV/cm)	τ_{decay} (ns)	$\lambda_{\max}$ (nm)	n	Relative output	Hygro- scopicity
BGO	7.13	1.12	2.23	9.0	300	480	2.15	21	no
CsI(Tl)	4.51	1.86	3.57	5.6	1220	550	1.79	165	slight
LYSO(Ce)	7.40	1.14	2.07	9.6	40	420	1.82	85	no

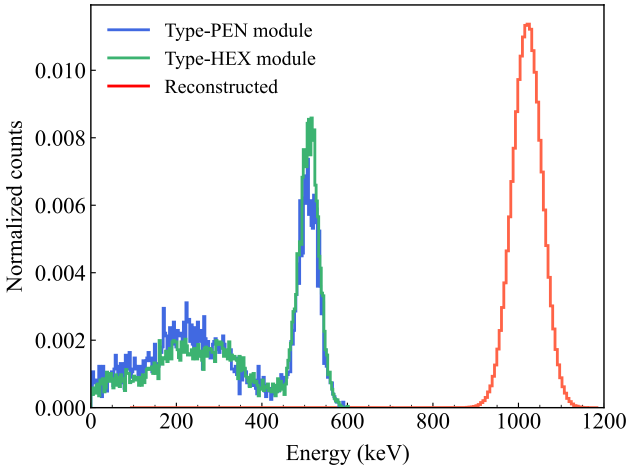

Fig. 44 (Color online) Spectra of a single Type-PEN module (*blue line*), a single Type-HEX module (*green line*) and reconstructed annihilation signals (*red line*) of M-to-$\bar{\mathrm{M}}$ conversion by simulation

Table 11 Summary of signal efficiencies in the Positron Detection System

Component	Efficiency type	Efficiency value
MCP	Detection efficiency $\varepsilon_{\mathrm{MCP}}$	32.6%
ECAL	Incident efficiency $\varepsilon^{\mathrm{In}}_{\mathrm{ECAL}}$	63.4%
	Geometric efficiency $\varepsilon^{\mathrm{Geom}}_{\mathrm{ECAL}}$	95.3%
	Reconstruction efficiency $\varepsilon^{\mathrm{Recon}}_{\mathrm{ECAL}}$	94.0%
Total signal efficiency		18.5%

a total of 622 modules and achieving 97% coverage of the 4π solid angle [111].

The ECAL should consider the particle energy in sub-MeV and several tens of MeV simultaneously, owing to the different physics goals in MACE Phase-I and MACE. In the 0.511 MeV energy regime of interest, a total absorption homogeneous calorimeter with inorganic scintillators generally provides excellent energy resolution, which is expected for MACE. Three types of crystals were considered for the MACE calorimeter: bismuth germanium oxide (BGO), thallium-doped cesium iodide (CsI:Tl), and cerium-doped lutetium-yttrium oxyorthosilicate (LYSO:Ce). The CsI(Tl) crystal was widely employed by the electromagnetic calorimeter of various experiments due to its high light yield [81, 82, 112]. However, it is characterized by a slow emission time, which may cause a loss of efficiency. The short radiation length also increases the cost of materials outside the ECAL. BGO combines an acceptable light output and a fast decay time, and is widely used in positron emission tomography (PET), which also investigates the signal of annihilation γ-rays. In addition, LYSO could be an appealing option because it is brighter and faster than BGO. The properties of these crystals are summarized in Table 10 [113].

The technical specifications of the photonsensor (e.g., the active area and photon detection efficiency) determine the efficiency of light collection. Photomultiplier Tubes (PMTs) and Silicon Photomultipliers (SiPMs) are commonly used photosensors in current particle and nuclear physics experiments. The active area of the PMTs was relatively larger than that of the SiPMs. However, they are characterized by a limited quantum efficiency (~20%), high operating voltage, and shielding requirements in magnetic fields. On the other hand, SiPMs offer excellent photon detection efficiency (~50%) and tolerance to magnetic fields. However, a single SiPM has small areas (usually 6 mm at maximum). Thus, SiPM arrays with large active areas are considered to enhance light collection efficiency.

9.2.3 Simulation

A beam of 10^8 μ^+ events with a momentum of 26.3 MeV/c entering the MACE detector has been simulated to evaluate the signal efficiency of ECAL. Following coincidence with MCP, a clustering algorithm was applied to search the seed modules and their adjacent modules. The energy of each triggered module was smeared, assuming an energy resolution of 10% at 0.511 MeV. We then estimated the energy sum and triggered time of the cluster, and applied an energy difference cut of $\Delta E_{\mathrm{recon}} < 0.1$ MeV to the reconstructed annihilation events. The resulting ECAL response spectra are shown in Fig. 44. Events that fell within the 3σ interval of the full-energy peak were identified as signal events.

9.3 Performance

The overall signal efficiency of the PDS can be derived from the MCP and ECAL results. First, the detection efficiency of MCP depends on the kinetic energy of the incident positron. According to the simulation results, the MCP efficiency for the positrons accelerated by the PTS was 32.6%. Second, we found that the primary components of the MCP, lead glass, and aluminum may induce multiple Compton scattering of 0.511 MeV photons. This effect resulted in a 36.6% efficiency loss, leading to a 63.4% incident efficiency of annihilation events for the ECAL. Additionally, the geometric and reconstruction efficiencies of ECAL were considered to be 95.3% and 94%, respectively. The total signal efficiency can be estimated as

$$\varepsilon_{\mathrm{PDS}} = \varepsilon_{\mathrm{MCP}}\varepsilon^{\mathrm{In}}_{\mathrm{ECAL}}\varepsilon^{\mathrm{Geom}}_{\mathrm{ECAL}}\varepsilon^{\mathrm{Recon}}_{\mathrm{ECAL}}\ . \tag{35}$$

The values of these efficiencies are summarized in Table 11. Consequently, this analysis yielded a signal efficiency of 18.5% for the PDS. A higher efficiency can be achieved using MCP with a low-material-budget substrate.

10 Offline software

10.1 Introduction

The significance of offline software has increased in high-precision frontier experiments. The MACE offline software is responsible for the physical event generation, detector simulation, event reconstruction, offline event display, and analysis. In the conceptual design stage, offline software supports Monte Carlo simulations of physical and background events to guide the detector system design and optimization. During the engineering stage, offline software plays a crucial role in detector alignment, and can enhance the understanding of real circumstances through detailed simulations. Once the physical run begins, the offline software serves as a bridge that connects the experimental data to the physical results. A high-quality offline software system can simplify the workflow of researchers and potentially reduce systematic errors by accommodating more advanced technologies and algorithms, leading to accelerated research progress and increased physical sensitivity.

There are some objectives to ensure the expected functionality and performance of offline software.

- **Framework and architecture**: A well-designed architecture helps the development of simulation applications, reconstruction algorithms, and analysis, ensuring code consistency and reusability while enhancing software quality for better maintainability and reduced errors.
- **Performance**: In the case of MACE as a precision frontier experiment, the event rate could reach 10^7/s, and distributed computing is necessary for comprehensive physical studies, detector optimization, and data reconstruction and analysis in future operations.
- **Validation**: The output of the offline software, especially the physical results, should be continuously checked and compared to experiment data whenever possible. This can minimize any technical or physical errors in the code.
- **Continuous integration (CI)**: CI involves the frequently build, deployment, and testing of the offline software to uphold its availability and quality.

10.2 Framework

The Mustard framework is the most fundamental library of the MACE offline software. Mustard is a generic offline software framework for particle physics experiments [114], which provides a modern, high-performance architecture for distributed computing capabilities, unified geometric interfaces, and a high-level abstraction layer of data models out of the box, accelerating the development and performance of applications and libraries. The Mustard framework was formerly developed within the MACE offline software and is now extracted as a general proposed framework. It is designed as a set of commonly

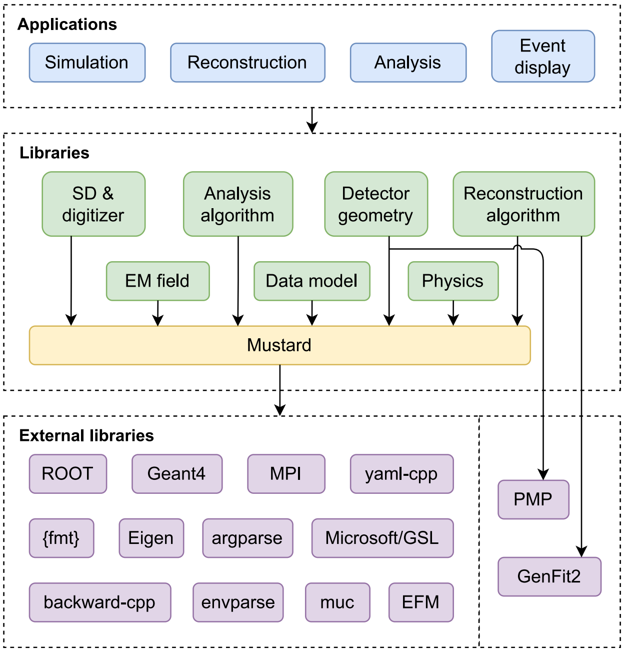

Fig. 45 (Color online) The architecture of MACE offline software

used interfaces and functionalities in fixed-target experimental simulation, reconstruction, and analysis, as shown in Fig. 45.

The framework was mainly developed with a concept-based object-oriented paradigm and template metaprogramming paradigm, utilizing the language constructs and standard library features of `C++20`. This approach enables the development of performance-critical utilities and interfaces without introducing extra runtime overheads. Following the technology roadmap, a low-level component inspired by the principles of the `C++` standard library involves a set of useful concepts, type traits, functions, and an optimized numeric algorithm. The low-level components are predominantly found in muc [115] and in the `Concept` and `Utility` components within Mustard.

Built on top of low-level infrastructure, Mustard provides a set of interfaces and utilities for distributed computing, simulation, customization of data models and distributed data processing, parameterized geometry construction and serialization, command argument parsing, logging, etc. An environmental component manages the resources and variables required for these functionalities. Mustard directly depends on MPI [116], ROOT [117], Geant4 [103, 118, 119], Eigen [120], and other libraries to form a high-level abstraction of these functionalities while maintaining compatibility with the common workflow of these underlying frameworks. A detailed description of these functionalities is provided in subsequent sections.

10.3 Parallel computing

MACE will be operated with a muon beam with a flux of 10^8/s and will collect data from 3×10^{15} muon or muonium decay events. Consequently, distributed parallel computing is essential for handling data processing requirements and carrying out simulations during the design stage. Two parallel computing models are investigated:

- Hybrid model: Multithreading for intra-node parallelism and communication, and message passing for inter-node parallelism and communication.
- Pure message passing model: Message passing for both intra- and inter-node parallelism and communication.

Both models demonstrated excellent scalability and performance, although they differed in practice. The hybrid model is found to be more memory-efficient and provides greater flexibility owing to its capability to finely control intra-node parallelism. However, it shows a slightly lower speedup owing to increased thread synchronization and potentially poorer CPU cache locality, as well as increased complexity in coding. On the other hand, the pure message passing model is slightly more memory consuming because of data (e.g., Geant4 data) duplication for each process within a node, but it offers superior speedup and reduced technical complexity. These are the results of potentially better CPU cache locality and absence of thread competition. Consequently, the pure message passing model was selected as the parallel computing model for the MACE offline software.

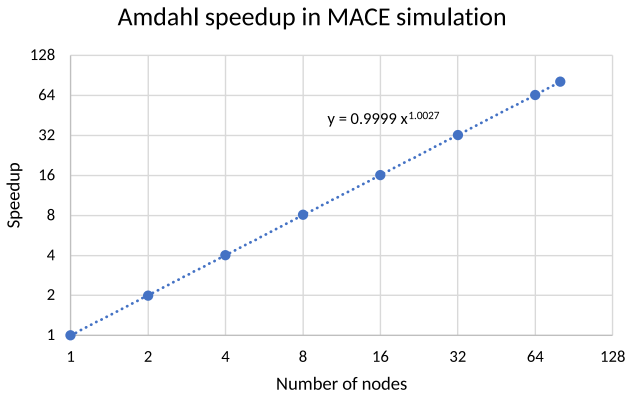

Fig. 46 (Color online) Speedup test at Tianhe-2 supercomputer. Each node has 24 cores. Results shows a linear speedup, and no significant performance degradation is observed

The message passing model is implemented based on the Message Passing Interface (MPI) [116]. MPI offers a scalable interface for distributed computing on high-performance computing (HPC) clusters and high-throughput computing (HTC) clusters. Within the Mustard framework, a generic executor based on MPI is provided for dynamically scheduling computing tasks among all the executing processes. The executor handles scheduling and execution while users customize the actual tasks. Building upon this extensible functionality is a Geant4 simulation run manager and an event-by-event data processor as solutions to distributed Geant4 simulation and distributed event reconstruction or analysis. In the executor, a master/slave pattern communication algorithm is employed for task division and assignment, and the overlap between computation and communication is maximized to minimize latency and enhance performance. A speedup test was performed and the results are shown in Fig. 46. The results demonstrate a linear speedup on 1920 cores (80 computing nodes) in the event loop of a benchmark simulation example, and no significant performance degradation was observed. Thus, it is concluded that the distributed computing infrastructure can meet the requirements for the future development of MACE offline software.

10.4 Event data model

The event data model is in the central position of the offline software system. It conceptualizes how data are produced and stored, data streamlines, and how data should be processed.

Therefore, it conceptualizes the large functional parts of offline software. The Mustard framework provides an interface for building a static event data model, encoding field information in the `C++` type system with the help of a template metaprogramming infrastructure. This enables the checking of data model consistency and usage in user code at compile time. With the names and types of all fields known at the compile time, Mustard also provides a zero-overhead interface that maps the data model to a tuple-like type. This interface serves as a bridge between the data model and the actual data object, which ensures consistency and is practical in any operation, such as reading/writing data from/to a disk or applying an algorithm to process the data. Based on the data model interface, the MACE offline software predefined some commonly used data models for simulation, reconstruction, and analysis applications. It is also simple to extend data models to developers and users. However, owing to the static nature of the event data model interface and architecture, it remains a challenge to dynamically define the data model via configuration files, such as JSON or YAML. This issue will be addressed in future studies.

10.5 Detector geometry and field

Geometric system are extensively used in both simulation and reconstruction to describe and define the geometry, material, and field of the detector system. The task of geometric framework is to describe the information required for both humans and machines. This process involves two aspects. A human-readable geometry description is generally a characteristic geometric parameter such as the inner radius of the CDC and the number of collimator foils. The machine needs a full description of the entire geometry, such as the position and transformation of every CDC wire. Therefore, a gap exists between the real human-readable parameters and exact geometry definition.

The geometric interface of the Mustard framework aims to address this discrepancy. It separates the human-readable detector description from the detailed definition of detector geometry. In this architecture, the detector definitions are responsible for the exact construction of the detector geometry and material, depending on the parameters specified in the corresponding detector descriptions. The detector description does nothing but provides an interface for defining and fetching these parameters. This architecture separates the technical parts from the physical parts during detector construction. The flow chart of detector construction is shown in Fig. 47.

The electromagnetic field is another essential subject in simulations and reconstruction. The Mustard framework provides an interface for users to define a set of reusable fields. The defined field can be used in both the simulation and reconstruction through the corresponding wrappers. The Mustard framework also supports the definition of interpolated electromagnetic fields from discrete field data to fulfill the requirement of importing the MACE field map.

10.6 Continuous integration

Continuous integration (CI) is the practice of frequently integrating software code, building, deploying and testing its functionality. CI can keep the software in an available state and efficiently incorporate newly developed functionalities into practice or production. CI also serves as a practice for observing and fixing errors at an early stage. The development branch of the MACE offline software has been continuously building and deploying on the Tianhe-2 supercomputer utilizing the container technique via an Apptainer (formerly known as Singularity) [121]. An autonomous workflow was developed to build fully optimized Apptainer images for different MPI applications. Currently, the image size ranges from approximately 4 GB for images with GEANT4 data and approximately 2 GB for images without GEANT4 data. They were uploaded to the Tianhe-2 supercomputer and updated on demand. The CI workflow is still under investigation, and it is planned to deploy a CI workflow on local or cloud servers to automatically perform the CI of the MACE offline software in the future.

10.7 Event display

Event display software has become increasingly important in experimental particle and nuclear physics research. This

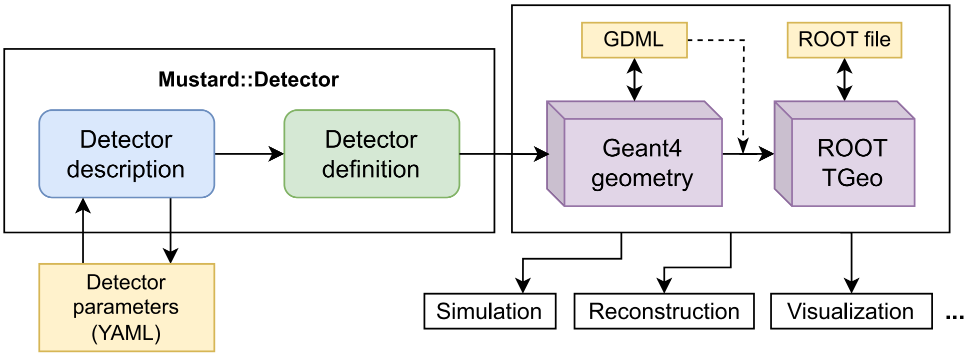

Fig. 47 (Color online) Flow chart of geometry management

software was used to visualize the detector response information and the reconstructed information for the particles that passed through the detectors. The importance of this software is threefold: First, it is essential for outreach and educational purposes. Students and new researchers can use event displays to gain a more intuitive understanding of how particles interact with detectors and how data are collected and analyzed. This visual approach helps to bridge the gap between theoretical knowledge and practical applications, making it easier to grasp complex concepts. Second, by providing a clear and detailed visualization of the event data, researchers may identify inconsistencies or errors in the data processing pipeline that might not be obvious through numerical data alone, allowing them to identify potential issues more easily in data analysis. Third, it is crucial for the online monitoring of data acquisition to ensure data quality. Real-time event displays allow researchers to monitor the data as they are being collected, quickly identifying any issues with the detectors or data acquisition system. This immediate feedback is vital for maintaining high data quality and ensuring that any problems are addressed promptly, thereby minimizing the risk of data loss or corruption.

For MACE, we need to develop event display software for similar purposes. We envision that the software should have the following contents and functionalities:

- **3D Models**: The software should contain 3D models for the main detectors of the MACE experimental apparatus. This provides a comprehensive visual representation of the experimental setup, aiding in the understanding and analysis of the data.
- **Detector Signals and Reconstructed Hits and Tracks**: For both experimental data and simulated events, the program should display detector signals as well as reconstructed hits and tracks.
- **Online Data Monitoring**: For online data monitoring, the program should automatically take some events from time to time from the data stream, analyze the event online, and display information as described in the previous point. This functionality is crucial for ensuring the continuous monitoring and immediate analysis of data to promptly detect any potential issues.
- **Average Occupancy Display**: The software should display the average occupancy of all detector channels over a period of time. This will help monitor the performance of the detectors and ensure that they are running properly. Any anomalies or irregularities in occupancy can be quickly identified and addressed.
- **User Interaction with 3D Modules**: The program should allow users to interact with the 3D modules. For instance, when a user clicks on an ECAL module, there should be a pop-up window displaying detailed information such as the channel name, high-voltage setting, and ADC spectrum over a period of time. This interactive feature enhances the usability of software and provides researchers with easy access to detailed detector information.

Game engines are suitable candidates for meeting these requirements, as they are designed to handle complex graphics, real-time rendering, and interactive environments, making them ideal for developing sophisticated event display software. Among the available game engines, Unreal Engine 5 [122] stands out as an optimal choice for several reasons.

1. It offers unparalleled graphical fidelity. Its advanced rendering capabilities can create highly detailed and realistic 3D models of the MACE experimental apparatus.
2. It provides powerful tools for real-time data processing and visualization. Its robust framework allows for the integration of live data streams, enabling the software to display detector signals, reconstructed hits, and tracks in real time. This capability is essential for online data monitoring and ensures that researchers can promptly detect and address any issues with the data acquisition system.
3. It supports extensive interactivity. With a user-friendly interface and comprehensive toolset, developers can create interactive 3D modules that allow users to click on specific components. This interactive feature significantly improves the usability of software, providing researchers with easy and intuitive access to crucial data.
4. It has robust support for Python through various plugins. This allows developers to utilize powerful Python libraries such as Matplotlib to create histograms and other visualizations for displaying data. The integration of Python simplifies the development process, making it easier to implement complex data analysis and visualization features directly within the software.
5. Unreal Engine 5 is free software, at least for educational and non-profit purposes, with an extensive user community and strong support network, significantly facilitating the development process.

Currently, the event display software development is in its early stages. We successfully imported the 3D models for the essential from Geant4 into Unreal Engine 5 (Fig. 48a). For simulated events, the software was already capable of displaying several key elements. With simple keyboard inputs, it can visualize the energy deposition on the ECAL modules for different events, showing how and where particles interact with the calorimeter (Fig. 48b). Additionally, the software can display electron tracks within the spectrometer, allowing researchers to observe the electron trajectories as they move through the magnetic field and eventually produce signals on the TTCs. Furthermore, the software can identify and display the drift cells activated by these

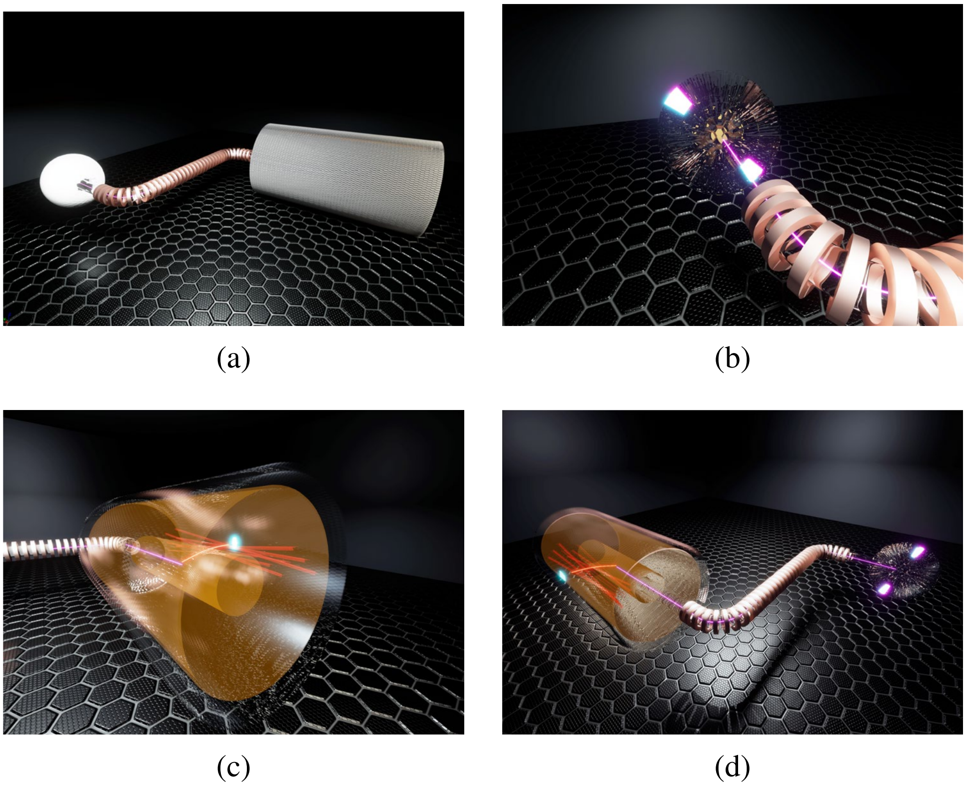
(a) (b) (c) (d)

Fig. 48 (Color online) **a** 3D modules imported from Geant4 into the Unreal Engine, including ECAL, MCP, PTS, TTC and CDC. Sensitive detectors will be made semi-transparent during event displays for better signal visualization. **b** An event display for the ECAL. Energy deposition in the ECAL modules was displayed using a rainbow color scheme, with purple indicating low energy and red indicating high energy. **c** A event display for the CDC. The highlighted curved tracks depict the electron trajectory, whereas the semi-transparent colored cylinders indicate the drift cells that were fired. The radii of the cylinders represent drift distances. The electron eventually hits the TTC, leaving detectable signals on several adjacent modules. **d** An overview of the entire event

particles, providing a detailed view of the particle interactions within the detector (Fig. 48c).

11 Background estimation

In this section, we summarize the background simulation results available at present. A summary of potential backgrounds can be seen in Table 12.

11.1 Physical backgrounds

a. Muon internal conversion decay $\mu^+ \to e^+e^-e^+\nu_e\bar{\nu}_\mu$. As stated in Sect. 3.2, the SM-allowed muon rare decay $\mu^+ \to e^+e^-e^+\nu_e\bar{\nu}_\mu$ is a major source of physical background. We generated 10^9 $\mu^+ \to e^+e^-e^+\nu_e\bar{\nu}_\mu$ events using the Metropolis-Hasting algorithm based on the leading-order squared amplitude of $\mu^+ \to e^+e^-e^+\nu_e\bar{\nu}_\mu$ [123]. Kinematic cuts corresponding the MMS geometry were applied to reduce the variance in the simulation results. Assuming a 10^8 $\mu\mathrm{OT/s}$ muon-on-target (μOT) flux, the generated internal conversion decay events correspond to 114.12 years of data, predicted by leading-order QED calculations based on McMule [124]. After event selection, the background rate was estimated to be $0.29 \pm 0.02/(10^8\ \mu\mathrm{OT/s} \cdot 1\ \mathrm{yr})$.

11.2 Accidental backgrounds

b.Beam-related Backgrounds. The muon beam produced by stopping π^+ on the surface of a target typically contains positrons or other particles of the same momentum [125]. These backgrounds are considered accidental coincidences. As shown in Sect. 4.2.2, the ratio of positrons to muons will reach the level of 1%. Assuming a 10^8 $\mu\mathrm{OT/s}$ muon-on-target flux, the upper limit of the background rate is estimated to be $0.07/(10^8\ \mu\mathrm{OT/s} \cdot 1\ \mathrm{yr})$ at 90% C.L.

c.Cosmic-Ray Muon Backgrounds. The EcoMug generator [126] was employed to generate cosmic-ray muon events for the simulation. The ECAL was placed at the center of a hypothetical tunnel surrounded by a copper solenoid and iron shield. Cosmic-ray muons are set to be emitted from a plane source at sea level. No event passed the event selection, and the 90% C.L. upper limit of the background rates was estimated to be $2/(10^8\ \mu\mathrm{OT/s} \cdot 1\ \mathrm{yr})$. Generally, a veto system can be installed outside the ECAL to further exclude the background contribution of cosmic-ray muons [2, 127].

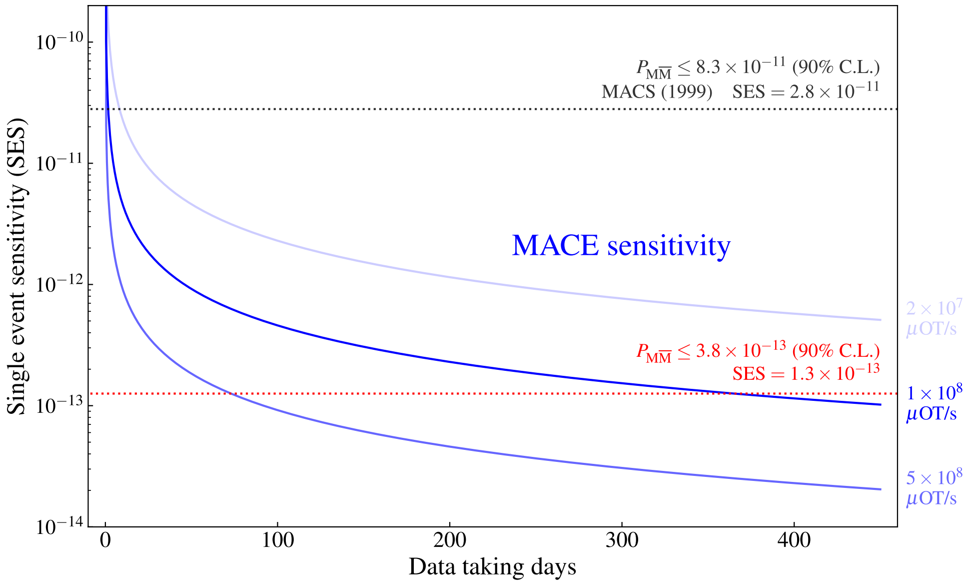

Fig. 49 (Color online) The MACE single event sensitivity (SES) to the muonium-to-antimuonium conversion

Table 12 Summary of currently investigated backgrounds

Background type		Counts per 10^8 μOT/s · 1 yr
Physical	$\mu^+ \to e^+e^-e^+\nu_e\bar{\nu}_\mu$	0.29 ± 0.02
Accidental	Beam postiron	< 0.07
	Cosmic ray (with veto)	< 0.1
Total		< 1

Table 13 Summary of signal efficiencies in the MACE detector system

Detector, component or analysis	Efficiency type	Efficiency
Magnetic spectrometer	Geometric ($\varepsilon^{\mathrm{geom}}_{\mathrm{MMS}}$)	84.6%
	Reconstruction ($\varepsilon^{\mathrm{recon}}_{\mathrm{MMS}}$)	∼ 80%
Positron transport system	Transmission ($\varepsilon_{\mathrm{PTS}}$)	65.8%
Microchannel plate	Detection ($\varepsilon_{\mathrm{MCP}}$)	32.6%
Electromagnetic calorimeter	Incident ($\varepsilon^{\mathrm{In}}_{\mathrm{ECAL}}$)	63.4%
	Geometric ($\varepsilon^{\mathrm{Geom}}_{\mathrm{ECAL}}$)	95.3%
	Reconstruction ($\varepsilon^{\mathrm{Recon}}_{\mathrm{ECAL}}$)	94.0%
Total detection efficiency		8.25%
Analysis	Event selection ($\varepsilon_{\mathrm{Cut}}$)	∼ 80%
Total signal efficiency		6.6%

12 Sensitivity

In the baseline run plan, MACE will take data from 1 year data acquisition duration with 10^8 s^{-1} muon-on-target (μOT) flux, with beam momentum of 24 MeV/c and an RMS spread of 1.35 MeV/c. A ratio of in-vacuum muonium to μOT ($N^{\mathrm{vac}}_{\mu}/N^{\mathrm{OT}}_{\mu^+}$) of 3.8% is possible to achieve in the muonium production target. Consequently, during the physical run, MACE is expected to collect data from $N^{\mathrm{vac}}_{\mu} = 1.20 \times 10^{14}$ muonium decay events in a vacuum of interest.

Not all antimuonium decay events in vacuum can be detected owing to limitations in the geometric acceptance and detection efficiency of the detector. The signal efficiency of each detector or component is summarized in Table 13. Background simulations from the previous section suggest that a near background-free search for muonium-to-antimuonium conversion is possible, and single event sensitivity (SES) can serve as an indicator of experimental sensitivity. Based on the number of muonium decay events in a vacuum and the signal efficiencies of all detectors or components, the single event sensitivity of the experimental design presented in this article to muonium-to-antimuonium conversion is estimated as

$$\begin{aligned}\mathrm{SES} &= \frac{1}{\varepsilon^{\mathrm{geom}}_{\mathrm{MMS}}\varepsilon^{\mathrm{recon}}_{\mathrm{MMS}}\varepsilon_{\mathrm{PTS}}\varepsilon_{\mathrm{MCP}}\varepsilon^{\mathrm{In}}_{\mathrm{ECAL}}\varepsilon^{\mathrm{Geom}}_{\mathrm{ECAL}}\varepsilon^{\mathrm{Recon}}_{\mathrm{ECAL}}\varepsilon_{\mathrm{Cut}}N^{\mathrm{vac}}_{\mathrm{M}}} \\ &= 1.3 \times 10^{-13}\,.\end{aligned} \tag{36}$$

We estimated the upper limit for the muonium-to-antimuonium conversion probability using the Poisson counting statistic [37]. Assuming a conservative background count expectation of $b = 1$ according to Table 12, and an observed event count of $n_{\mathrm{obs}} = b$, the experimental design presented in this article is expected to attain an upper limit, at a confidence level of $1 - \alpha = 0.9$ (Fig. 49),

$$\begin{aligned}P(\mathrm{M} \to \overline{\mathrm{M}}) &\lesssim \left(\frac{1}{2}F^{-1}_{\chi^2}\big(1-\alpha;2(n_{\mathrm{obs}}+1)\big) - b\right) \times \mathrm{SES} \\ &= 3.8 \times 10^{-13}\,.\end{aligned} \tag{37}$$

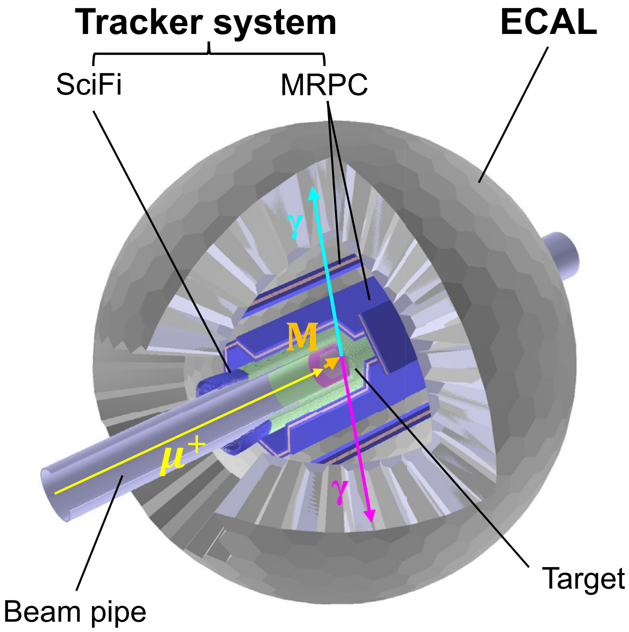

Fig. 50 (Color online) The MACE PHASE-I detector concept (an $M \to \gamma\gamma$ event is displayed for example)

13 Proposal of MACE PHASE-I

13.1 Introduction

Taking advantage of the optimized MACE detector system and the construction of high-intensity muon beams in China, the search for other cLFV processes involving muons could be forthcoming. Therefore, we propose the MACE PHASE-I experiment aimed at further physical goals. This will help evaluate the performance of particular sub-detectors before the full construction of MACE. Additionally, a measurement of muon polarization, similar to that performed in the MEG experiment [128], can be conducted to characterize the energy and angular distributions of the muon decay products.

Figure 50 presents the layout of PHASE-I detector system. The detector system is based on the ECAL and an extra inner tracker system, which consists of a scintillating fiber (SciFi) tracker and a multigap resistive plate chamber (MRPC) hodoscope. The tracker system is designed to provide the hit position and hit time of e^+ which could be a signal or background, depending on specific processes. The photons barely trigger the SciFi and MRPC, such that they can only be reconstructed by ECAL. The cLFV processes in the detector's capacity may include μ^+e^- scattering and the rare decay of muons and muonium. To better emphasize the necessity of the PHASE-I experimental stage, efforts to search for such processes in history are reviewed as follows.

Table 14 Muon beam requirements for MACE PHASE-I

Muon flux	10^6–10^7 μ^+/s
Working mode	Continuous wave
Beam spot diameter	$\lesssim 30$ mm
Momentum spreading (σ_p/p)	$\lesssim 10\%$
Positron-to-muon ratio	$\lesssim 1\%$
Data acquisition duration	360 days

13.1.1 $\mu^+ \to e^+\gamma\gamma$ decay

The Crystal Box experiment at the Los Alamos Meson Physics Facility (LAMPF) first constrained the branching ratio to $\mathcal{BR}(\mu^+ \to e^+\gamma\gamma) < 7.2 \times 10^{-11}$ at a 90% confidence level in 1988 [35]. There are no updated results or dedicated experimental plans for this decay mode. Several new physics models predict a higher rate or sensitivity of $\mu^+ \to e^+\gamma\gamma$ compared with $\mu^+ \to e^+\gamma$ [129, 130], which offers a solid motivation to search for this process.

13.1.2 Muonium decays

Muonium decay, for example, $M \to \gamma\gamma$, features a relatively clear final state consisting of two back-to-back 53 MeV photons. The most recent search for muonium decay can be traced back to an experiment conducted in 1959 by York et al. [26]. The detector system consists of a muon production target, a stopping target, and two sets of NaI scintillation counters. A 77 MeV π^+ beam was directed to a carbon block to produce decay muon, which was further stopped in a copper target. The experiment sets up a loose bound of $\mathcal{O}(10^{-5})$ on $\mu^+e^- \to \gamma\gamma$ [26, 131]. With the optimized detector system in PHASE-I, a significant improvement in sensitivity is expected for $M \to \gamma\gamma$ decay.

13.2 Muon beam

An estimation of the requirements for a muon beam is presented in Table 14. The beam intensity is primarily limited by the sensitivity and rate of accidental coincidences. An excessively low intensity is insufficient to meet the sensitivity goals of PHASE-I, whereas an excessively high intensity would lead to an increased rate of accidental coincidences, which would not contribute further to enhancing the sensitivity. As a conservative estimation, the optimal beam intensity ranged from 10^6 to 10^7 μ^+/s. In the next few years, the surface muon beam provided by CiADS is expected to achieve the required beam parameters.

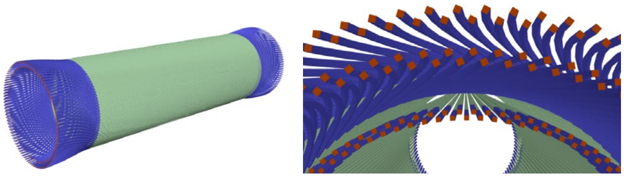
(a) (b)

Fig. 51 (Color online) **a** Overall view of the SciFi Tracker. The radius of the detector is approximately 5.5 cm, the length is approximately 32.5 cm. **b** Details of the SciFi tracker. In this figure, One of the three layers is made up of two layers of fibers. Each Scintillating fiber (green) is connected with an optical fiber (blue) and a SiPM (orange) is tied at the end of the optical fiber

13.3 Design of the detector system

13.3.1 Electromagnetic calorimeter

The basic design of the ECAL in PHASE-I is identical to Sect. 9.2, but with some modules around the beam window removed. Instead of the 0.511 MeV regime in MACE, the signal related to MACE PHASE-I is up to $\sim$ 50 MeV, which presents a challenge for the current ECAL design. Both BGO and LYSO crystals were considered because of their relatively high density and light yield. Currently, LYSO crystals ($\sim 12X_0$) are employed in PHASE-I simulation studies to achieve a better energy resolution and a more compact design. The fast emission time of LYSO also makes it capable to rejecting background and pileup events.

13.3.2 Tracker system

The timing and spatial resolution of ECAL are limited. More importantly, ECAL can hardly discriminate between e^+ and γ by itself. An inner tracker system was designed to identify e^+s and measure their arrival times and tracks. First, three layers of scintillating fibers were arranged along the surface of the cylinder outside the beam pipe. It reconstructs the track and hit times of incoming e^+. Second, the outer layer is an array of multigap resistive plate chamber (MRPC), which offers extremely high timing precision. This combination ensures a great enhancement of sensitivity by reducing any accidental and physical background as a result of increased tracking and timing precision.

a.Scintillating fiber tracker A scintillating fiber (SciFi) tracker for high-precision timing and tracking was designed. It is expected to have a time resolution of $\mathcal{O}(1)$ ns and a high detection efficiency for distinguishing the signal from the background. In the current design, the SciFi tracker comprises three layers: two helical layers and a transverse layer. The helical fibers were arranged at a tilt angle to ensure that they rotated 360° in the azimuthal angle ϕ from one side of the veto to the other side, whereas the transverse fibers extended parallel to the axial direction. Each layer contains 200 fibers and extends 325.4 mm along the axial direction with an average thickness of 1.3 mm, as shown in Fig. 51. The radii of each layer were 45, 50 and 55 mm, respectively. This design resulted in a geometric acceptance of 95.6%. The 1 mm width single cladding square scintillating fibers produced by Kuraray were considered in the benchmark design [132]. Each fiber was mechanically held in place independently. The scintillation light emitted in the fibers is transported by light guide fibers and read out by SiPMs, where the signals of each fiber are output individually. The total number of channels was 600 in the current design.

b.Multigap resistive plate chamber hodoscope Although the SciFi tracker can provide good spatial resolution, better timing capability is required to further suppress potential physical and accidental backgrounds. MRPC is typically used in high energy physics experiments as a time-of-flight detector owing to its high performance, simplicity, and low cost. The detector is mainly made of glass and plastic, and is finally housed in an aluminum alloy gas chamber filled with working gas. MRPC can achieve a detection efficiency exceeding 95% for charged particles, along with an excellent timing resolution of approximately 50 ps and $\mathcal{O}(1)$ mm spatial resolution [133]. The specification perfectly matches the requirements of the MACE PHASE-I. Under the current design, eight MRPC modules were situated between the SciFi tracker and the ECAL, fully covering the radial direction. The MRPC tags the charged particle along with the SciFi and provides high-precision time information for event reconstruction.

14 Summary

In this study, we reported the theoretical and experimental aspects of the conceptual design of MACE. With the current MACE detector concept, including the muonium production target, Michel electron magnetic spectrometer (MMS), positron transport system (PTS), and positron detection system (PDS), two orders of magnitude or better improvement in the muonium-to-antimuonium process compared to the current limit is forthcoming. Moreover, we intend to utilize a portion of the MACE detector to search for the rare muonium decay process before the full construction of MACE. Future works will be continuously conducted in areas such as full simulation and reconstruction, software development, technical design, and prototyping of each subdetector.

The observation of charged lepton flavor violation processes clearly indicates the presence of new physics beyond the Standard Model. Charged lepton flavor violations in processes such as $\mu^- N \to e^- N$ conversion, muon decays such as $\mu^+ \to e^+ \gamma$ and $\mu^+ \to e^+ e^- e^+$, and the conversion of muonium to antimuonium ($\mu^+e^- \to \mu^-e^+$) may exhibit significant effects that could be within the scope of future experiments. The proposed MACE concept holds promise for exploring new physics of the muonium-to-antimuonium conversion process. In conjunction with other flavor and collider searches, MACE will illuminate the mysteries of new physics beyond the Standard Model.

Acknowledgements We express our gratitude to Klaus Jungmann, Yoshitaka Kuno, Kim-Siang Khaw, Lorenzo Calibbi, Ce Zhang, Tsutomu Mibe, Yuichi Uesaka, Yu Bao, Ningqiang Song and many other colleagues for their insights and expertise during discussions. We also appreciate the professional and constructive comments provided by Xin Chen, Kim-Siang Khaw, Teng Li, Yi Liao, Yong Liu and Xiang Xiao in reviewing this article. The simulation benefited greatly from the provision of computing resources by the National Supercomputer Center in Guangzhou. The Feynman diagrams shown in this article are created using TikZ-Feynman.

References

1. A. Ilakovac, A. Pilaftsis, Flavor violating charged lepton decays in seesaw-type models. Nucl. Phys. B **437**, 491 (1995). https://doi.org/10.1016/0550-3213(94)00567-X
2. R. Abramishvili, G. Adamov, R.R. Akhmetshin et al., COMET phase-I technical design report. Prog. Theor. Exp. Phys. **2020**, 033C01 (2020). https://doi.org/10.1093/ptep/ptz125
3. L. Bartoszek, E. Barnes, J. P. Miller et al., Mu2e technical design report (2014). https://doi.org/10.48550/arXiv.1501.05241.
4. K. Arndt, H. Augustin, P. Baesso et al., (Mu3e), technical design of the phase I Mu3e experiment. Nucl. Instrum. Meth. A **1014**, 165679 (2021). https://doi.org/10.1016/j.nima.2021.165679
5. A.M. Baldini, E. Baracchini, C. Bemporad et al., (MEG II), the design of the MEG II experiment. Eur. Phys. J. C **78**, 380 (2018). https://doi.org/10.1140/epjc/s10052-018-5845-6
6. V.W. Hughes, D.W. McColm, K. Ziock et al., Formation of muonium and observation of its larmor precession. Phys. Rev. Lett. **5**, 63–65 (1960). https://doi.org/10.1103/PhysRevLett.5.63
7. B. Pontecorvo, Mesonium and anti-mesonium. Sov. Phys. JETP **6**, 429 (1957)
8. L. Willmann, P.V. Schmidt, H.P. Wirtz et al., New bounds from searching for muonium to anti-muonium conversion. Phys. Rev. Lett. **82**, 49–52 (1999). https://doi.org/10.1103/PhysRevLett.82.49
9. B. Grzadkowski, M. Iskrzynski, M. Misiak et al., Dimension-six terms in the standard model lagrangian. JHEP **10**, 085 (2010). https://doi.org/10.1007/JHEP10(2010)085
10. R. Conlin, A.A. Petrov, Muonium-antimuonium oscillations in effective field theory. Phys. Rev. D **102**, 095001 (2020). https://doi.org/10.1103/PhysRevD.102.095001
11. A.A. Petrov, R. Conlin, C. Grant, Studying $\Delta L = 2$ lepton flavor violation with muons. Universe **8**, 169 (2022). https://doi.org/10.3390/universe8030169.
12. E. Fernández-Martínez, X. Marcano, D. Naredo-Tuero, Global lepton flavour violating constraints on new physics. Eur. Phys. J. C **84**, 666 (2024). https://doi.org/10.1140/epjc/s10052-024-12973-6
13. J. Heeck, M. Sokhashvili, Lepton flavor violation by two units. Phys. Lett. B **852**, 138621 (2024). https://doi.org/10.1016/j.physletb.2024.138621
14. P. S. Bhupal Dev, R. N. Mohapatra, and Y. Zhang, Probing TeV scale origin of neutrino mass at future lepton colliders via neutral and doubly-charged scalars. Phys. Rev. D **98**(7), 075028 (2018). https://doi.org/10.1103/PhysRevD.98.075028
15. C. Han, D. Huang, J. Tang et al., Probing the doubly charged Higgs boson with a muonium to antimuonium conversion experiment. Phys. Rev. D **103**, 055023 (2021). https://doi.org/10.1103/PhysRevD.103.055023
16. L. Calibbi, T. Li, L. Mukherjee et al., Probing ALP lepton flavor violation at μTRISTAN. Phys. Rev. D **110**, 115009 (2024). https://doi.org/10.1103/PhysRevD.110.115009
17. P. Foldenauer, J. Jaeckel, Purely flavor-changing Z’ bosons and where they might hide. JHEP **05**, 010 (2017). https://doi.org/10.1007/JHEP05(2017)010
18. J. Kriewald, J. Orloff, E. Pinsard et al., Prospects for a flavour violating Z' explanation of $\Delta a_{\mu,e}$. Eur. Phys. J. C **82**, 844 (2022). https://doi.org/10.1140/epjc/s10052-022-10776-1
19. J. Liu, M. Song, H. Zhang, Revisiting for maximal flavor violating $Z'_{e\mu}$ and its phenomenology constraints. JHEP **10**, 128 (2024). https://doi.org/10.1007/JHEP10(2024)128
20. R. Ding, J. Li, M. Lu et al., Study of charged Lepton Flavor Violation in electron muon interactions. J. High Energy Phys. **2025**, 165 (2025). https://doi.org/10.1007/JHEP01(2025)165
21. A. Abada, A.M. Teixeira, Heavy neutral leptons and high-intensity observables. Front. Phys. **6**, 142 (2018). https://doi.org/10.3389/fphy.2018.00142
22. Y. Zhang, Charged lepton flavor violation at the high-energy colliders: neutrino mass relevant particles. Universe **8**, 164 (2022). https://doi.org/10.3390/universe8030164
23. C.-H. Chen, C.-W. Chiang, T. Nomura et al., Lepton flavor violation and scotogenic Majorana neutrino mass in a Stueckelberg $U(1)_X$ model. JHEP **09**, 166 (2022). https://doi.org/10.1007/JHEP09(2022)166
24. J. Kriewald, E. Pinsard, A.M. Teixeira, High-energy cLFV at μTRISTAN: HNL extensions of the Standard Model. J. High Energy Phys. **2025**, 116 (2025). https://doi.org/10.1007/JHEP02(2025)116
25. T. Fukuyama, Y. Mimura, Y. Uesaka, Models of the muonium to antimuonium transition. Phys. Rev. D **105**, 015026 (2022). https://doi.org/10.1103/PhysRevD.105.015026
26. C.M. York, C.O. Kim, W. Kernan, Search for the reaction $\mu^+ + e^- \to \gamma + \gamma$. Phys. Rev. Lett. **3**, 288–291 (1959). https://doi.org/10.1103/PhysRevLett.3.288
27. J. Dreitlein, H. Primakoff, Possible neutrinoless decay modes of the muon. Phys. Rev. **126**, 375–378 (1962). https://doi.org/10.1103/PhysRev.126.375
28. P.-J. Li, Z.-Q. Tan, C.-E. Wu, Weak decays of polarised muonium and polarised pionium. J. Phys. G **14**, 525–534 (1988). https://doi.org/10.1088/0305-4616/14/5/012
29. A. Czarnecki, G.P. Lepage, W.J. Marciano, Muonium decay. Phys. Rev. D **61**, 073001 (2000). https://doi.org/10.1103/PhysRevD.61.073001
30. J.O. Eeg, K. Kumericki, I. Picek, The double radiative annihilation of the heavy light fermion bound states. Fizika B **10**, 285–306 (2001)
31. G. Cvetic, C.O. Dib, C.-S. Kim et al., Lepton flavor violation in muonium decay and muon colliders in models with heavy neutrinos. Phys. Rev. D **74**, 093011 (2006). https://doi.org/10.1103/PhysRevD.74.093011
32. S.N. Gninenko, N.V. Krasnikov, V.A. Matveev, Invisible decay of muonium: tests of the standard model and searches for new physics. Phys. Rev. D **87**, 015016 (2013). https://doi.org/10.1103/PhysRevD.87.015016
33. A. Shkerin, Muonium annihilation into $\nu_e{}^{-}\nu_\mu$ and $\nu_e{}^{-}\nu_\mu$. Phys. Rev. D **88**, 013012 (2013). https://doi.org/10.1103/PhysRevD.88.013012
34. R. Conlin, Lepton Flavor Violation and effective field theories. Ph.D. thesis, Wayne State U., Detroit (2022)

35. R.D. Bolton, M.D. Cooper, J.S. Frank et al., Search for rare muon decays with the crystal box detector. Phys. Rev. D **38**, 2077 (1988). https://doi.org/10.1103/PhysRevD.38.2077
36. U. Bellgardt, G. Otter, R. Eichler et al., (SINDRUM), search for the decay $\mu^+ \to e^+e^+e^-$. Nucl. Phys. B **299**, 1–6 (1988). https://doi.org/10.1016/0550-3213(88)90462-2
37. S. Navas, C. Amsler, T. Gutsche et al., (Particle data group), review of particle physics. Phys. Rev. D **110**, 030001 (2024). https://doi.org/10.1103/PhysRevD.110.030001
38. G. Feinberg, S. Weinberg, Conversion of muonium into antimuonium. Phys. Rev. **123**, 1439–1443 (1961). https://doi.org/10.1103/PhysRev.123.1439
39. T.E. Clark, S.T. Love, Muonium-anti-muonium oscillations and massive Majorana neutrinos. Mod. Phys. Lett. A **19**, 297–306 (2004). https://doi.org/10.1142/S0217732304013143
40. G. Cvetic, C.O. Dib, C.S. Kim et al., Muonium-antimuonium conversion in models with heavy neutrinos. Phys. Rev. D **71**, 113013 (2005). https://doi.org/10.1103/PhysRevD.71.113013
41. T. Li, M.A. Schmidt, Sensitivity of future lepton colliders and low-energy experiments to charged lepton flavor violation from bileptons. Phys. Rev. D **100**, 115007 (2019). https://doi.org/10.1103/PhysRevD.100.115007
42. M. Endo, S. Iguro, T. Kitahara, Probing $e\mu$ flavor-violating ALP at Belle II. JHEP **06**, 040 (2020). https://doi.org/10.1007/JHEP06(2020)040
43. R.H. Bernstein, P.S. Cooper, Charged lepton flavor violation: an experimenter's guide. Phys. Rept. **532**, 27–64 (2013). https://doi.org/10.1016/j.physrep.2013.07.002
44. M.B. Voloshin, M.A. Shifman, On the annihilation constants of mesons consisting of a heavy and a light quark, and $B^0 \leftrightarrow \overline{B}^0$ oscillations. Sov. J. Nucl. Phys. **45**, 292 (1987)
45. G. Burdman, I. Shipsey, D^0 - $\bar{D}^0$ mixing and rare charm decays. Ann. Rev. Nucl. Part. Sci. **53**, 431–499 (2003). https://doi.org/10.1146/annurev.nucl.53.041002.110348
46. A. Lenz, U. Nierste, Theoretical update of $B_s - \bar{B}_s$ mixing. JHEP **06**, 072 (2007). https://doi.org/10.1088/1126-6708/2007/06/072
47. E. Golowich, J. Hewett, S. Pakvasa et al., Implications of D^0 - $\bar{D}^0$ mixing for new physics. Phys. Rev. D **76**, 095009 (2007). https://doi.org/10.1103/PhysRevD.76.095009
48. U. Nierste, Three Lectures on Meson Mixing and CKM phenomenology, in Helmholz International Summer School on Heavy Quark Physics (2009) pp. 1–38. arXiv:0904.1869
49. J. F. Donoghue, E. Golowich, B.R. Holstein, Dynamics of the standard model, Vol. 2 (CUP, 2014)
50. A.A. Petrov, *Indirect searches for new physics* (CRC Press, Boca Raton, 2021)
51. W.-J. Song, Y.-F. Shen, Q. Qin, Double-mixing CP violation in B decays. Eur. Phys. J. C **84**, 1030 (2024). https://doi.org/10.1140/epjc/s10052-024-13350-z
52. Y. Hamada, R. Kitano, R. Matsudo et al., μTRISTAN. PTEP **2022**, 053B02 (2022). https://doi.org/10.1093/ptep/ptac059
53. M. Dong, Q. Ouyang, G. Li et al. (CEPC Study Group), CEPC conceptual design report: Volume 2-Physics & Detector (2018). arXiv:1811.10545
54. A. Abada, M. Abbrescia, S.S. AbdusSalam et al., (FCC), FCC-ee: the lepton collider: future circular collider conceptual design report volume 2. Eur. Phys. J. ST **228**, 261–623 (2019). https://doi.org/10.1140/epjst/e2019-900045-4
55. J.P. Ellis, Tikz-feynman: feynman diagrams with tikz. Comput. Phys. Commun. **210**, 103–123 (2017). https://doi.org/10.1016/j.cpc.2016.08.019
56. T. Fukuyama, Y. Mimura, Y. Uesaka, Insights from the magnetic field dependence of the muonium-to-antimuonium transition. Phys. Rev. D **108**, 095029 (2023). https://doi.org/10.1103/PhysRevD.108.095029. arXiv:2309.02060 [hep-ph]
57. W.-S. Hou, G.-G. Wong, Magnetic field dependence of muonium-anti-muonium conversion. Phys. Lett. B **357**, 145–150 (1995). https://doi.org/10.1016/0370-2693(95)00893-P
58. K. Horikawa, K. Sasaki, Muonium-anti-muonium conversion in models with dilepton gauge bosons. Phys. Rev. D **53**, 560–563 (1996). https://doi.org/10.1103/PhysRevD.53.560
59. Y. Hamada, R. Kitano, R. Matsudo et al., Precision $\mu^+\mu^+$ and μ^+e^- elastic scatterings. PTEP **2023**, 013B07 (2023). https://doi.org/10.1093/ptep/ptac174
60. E. Spedicato (MUonE), Status of the MUonE experiment, PoS DISCRETE2022 **431**, 068 (2024). https://doi.org/10.22323/1.431.0068
61. A. Masiero, P. Paradisi, M. Passera, New physics at the MUonE experiment at CERN. Phys. Rev. D **102**, 075013 (2020). https://doi.org/10.1103/PhysRevD.102.075013
62. S. Zhao, J. Tang, Progress of muonium-to-antimuonium conversion experiment. Nucl. Part. Phys. Proc. **345**, 24–28 (2024). https://doi.org/10.1016/j.nuclphysbps.2024.05.005
63. W. Altmannshofer, P. Munbodh, T. Oh, Probing lepton flavor violation at circular electron-positron colliders. JHEP **08**, 026 (2023). https://doi.org/10.1007/JHEP08(2023)026
64. T.-P. Cheng, L.-F. Li, Muon number nonconservation effects in a gauge theory with V A currents and heavy neutral leptons. Phys. Rev. D **16**, 1425 (1977). https://doi.org/10.1103/PhysRevD.16.1425
65. B.W. Lee, R.E. Shrock, Natural suppression of symmetry violation in gauge theories: muon-lepton and electron lepton number nonconservation. Phys. Rev. D **16**, 1444 (1977). https://doi.org/10.1103/PhysRevD.16.1444
66. G. Hernández-Tomé, G. López Castro, and P. Roig, Flavor violating leptonic decays of τ and μ leptons in the Standard Model with massive neutrinos, Eur. Phys. J. C **79**(1), 84 (2019). https://doi.org/10.1140/epjc/s10052-019-6563-4
67. P. Blackstone, M. Fael, E. Passemar, $\tau \to \mu\mu\mu$ at a rate of one out of 10^{14} tau decays? Eur. Phys. J. C **80**, 506 (2020). https://doi.org/10.1140/epjc/s10052-020-8059-7
68. W.H. Bertl, S. Egli, R. Eichler et al., (SINDRUM), search for the decay $\mu^+ \to e^+e^+e^-$. Nucl. Phys. B **260**, 1–31 (1985). https://doi.org/10.1016/0550-3213(85)90308-6
69. R. Abela, J. Bagaturia, W.H. Bertl et al., Improved upper limit on muonium to anti-muonium conversion. Phys. Rev. Lett. **77**, 1950–1953 (1996). https://doi.org/10.1103/PhysRevLett.77.1950
70. L. Willmann, K. Jungmann, Muonium-antimuonium conversion. SciPost Phys. Proc. **5**, 009 (2021). https://doi.org/10.21468/SciPostPhysProc.5.009
71. F.C. Liu, Y. Takeuchi, S. Chen et al., Simulation studies of a high-repetition-rate electron-driven surface muon beamline at SHINE. Phys. Rev. Accel. Beams **28**(8), 083401 (2025). https://doi.org/10.1103/PhysRevAccelBeams.28.083401
72. H.-J. Cai, Y. He, S. Liu et al., Towards a high-intensity muon source. Phys. Rev. Accel. Beams **27**, 023403 (2024). https://doi.org/10.1103/PhysRevAccelBeams.27.023403
73. G. Feinberg, S. Weinberg, Conversion of muonium into antimuonium. Phys. Rev. **123**, 1439–1443 (1961). https://doi.org/10.1103/PhysRev.123.1439
74. W. Schwarz, V. Ebert, H. Geerds et al., Thermal muonium in vacuo from silica aerogels. J. Non-Cryst. Solids **145**, 244–249 (1992). https://doi.org/10.1016/S0022-3093(05)80465-X
75. G.A. Beer, Y. Fujiwara, S. Hirota et al., Enhancement of muonium emission rate from silica aerogel with a laser ablated surface. PTEP **2014**, 091C01 (2014). https://doi.org/10.1093/ptep/ptu116
76. A. Antognini, P. Crivelli, L. Gerchow et al., Room-temperature emission of muonium from aerogel and zeolite targets. Phys. Rev. A **106**, 052809 (2022). https://doi.org/10.1103/PhysRevA.106.052809

77. J. Beare, G. Beer, J.H. Brewer et al., Study of muonium emission from laser-ablated silica aerogel. PTEP **2020**, 123C01 (2020). https://doi.org/10.1093/ptep/ptaa145
78. S. Kamioka (J-PARC g-2/EDM experiment), Muon cooling at J-PARC, PoS Muon4Future2023 **452**, 008 (2024). https://doi.org/10.22323/1.452.0008
79. S. Zhao, J. Tang, Optimization of muonium yield in perforated silica aerogel. Phys. Rev. D **109**, 072012 (2024). https://doi.org/10.1103/PhysRevD.109.072012
80. C. Zhang, T. Hiraki, K. Ishida et al., Modeling the diffusion of muonium in silica aerogel and its application to a novel design of multi-layer target for thermal muon generation. Nucl. Instrum. Meth. A **1042**, 167443 (2022). https://doi.org/10.1016/j.nima.2022.167443
81. M. Ablikim, Z.H. An, J.Z. Bai et al., (BESIII), design and construction of the BESIII detector. Nucl. Instrum. Meth. A **614**, 345–399 (2010). https://doi.org/10.1016/j.nima.2009.12.050
82. T. Abe, I. Adachi, K. Adamczyk et al. Belle II technical design report (2010). arXiv:1011.0352 [physics.ins-det]
83. C. Wu, T.S. Wong, Y. Kuon et al., Test of a small prototype of the COMET cylindrical drift chamber. Nucl. Instrum. Meth. A **1015**, 165756 (2021). https://doi.org/10.1016/j.nima.2021.165756
84. A.M. Baldini, H. Benmansour, G. Boca et al., Performances of a new generation tracking detector: the MEG II cylindrical drift chamber. Eur. Phys. J. C **84**, 473 (2024). https://doi.org/10.1140/epjc/s10052-024-12711-y
85. Eljen Technology, Fast timing plastic scintillator EJ-228, EJ-230, https://eljentechnology.com/images/products/data_sheets/EJ-228_EJ-230.pdf
86. M. Nishimura, F. Berg, M. Biasotti et al., Full system of positron timing counter in MEG II having time resolution below 40 ps with fast plastic scintillator readout by SiPMs. Nucl. Instrum. Meth. A **958**, 162785 (2020). https://doi.org/10.1016/j.nima.2019.162785
87. Hamamatsu Photonics K.K. and its affiliates, MPPC S13360 series, https://www.hamamatsu.com/content/dam/hamamatsu-photonics/sites/documents/99_SALES_LIBRARY/ssd/s13360_series_kapd1052e.pdf
88. E. Etzelmüller, J. Schwiening, A. Ali et al., (PANDA Cherenkov Group), the PANDA DIRC detectors. Nucl. Instrum. Meth. A **952**, 161790 (2020). https://doi.org/10.1016/j.nima.2019.01.017
89. S. S. Murray and J. H. Chappell, The advanced X-ray astrophysics facility high resolution camera, in X-ray instrumentation in astronomy. Vol. 0597, edited by J. L. Culhane, International Society for Optics and Photonics (SPIE, 1986) pp. 274 – 283. https://doi.org/10.1117/12.966592
90. O. H. Siegmund, A. S. Tremsin, and J. V. Vallerga, High performance cross-strip detector technologies for space astrophysics. in 2007 IEEE Nuclear Science Symposium Conference Record, Vol. 3 (2007) pp. 2246–2251. https://doi.org/10.1109/NSSMIC.2007.4436595
91. M. Barbera, G. K. Austin, A. Collura et al., Development of the UV/ion shields for the Advanced X-ray Astrophysics Facility high-resolution camera (AXAF HRC), in EUV, X-Ray, and Gamma-Ray Instrumentation for Astronomy V. Vol. 2280, edited by O. H. W. Siegmund and J. V. Vallerga, International Society for Optics and Photonics (SPIE, 1994) pp. 214 – 228. https://doi.org/10.1117/12.186815
92. E.H. Lehmann, P. Vontobel, G. Frei et al., Neutron imaging-detector options and practical results. Nucl. Instrum. Methods Phys. Res., Sect. A **531**(1–2), 228–237 (2004). https://doi.org/10.1016/j.nima.2004.06.010
93. J.S. Preston, U. Pasaogullari, D.S. Hussey et al., High resolution neutron radiography imaging of microporous layers in PEFCs. ECS Trans. **41**, 319–328 (2011). https://doi.org/10.1149/1.3635565
94. M. Williams, R. Sealock, S. Majewski et al., Pet detector using waveshifting optical fibers and microchannel plate pmt with delay line readout. IEEE Trans. Nucl. Sci. **45**, 195–205 (1998). https://doi.org/10.1109/23.664171
95. W.-S. Choong, Investigation of a multi-anode microchannel plate pmt for time-of-flight pet. IEEE Trans. Nucl. Sci. **57**, 2417–2423 (2010). https://doi.org/10.1109/TNS.2010.2060211
96. H. Kim, C.-M. Kao, H. Frisch et al., A design of pet detector using microchannel plate pmt with transmission line readout (IEEE, 2009) pp. 3106–3110. https://doi.org/10.1109/NSSMIC.2009.5401676
97. F. Ozok, T. Yetkin, E.A. Yetkin et al., Geant4 simulation of a conceptual calorimeter based on secondary electron emission. J. Instrum. **12**, P07014 (2017). https://doi.org/10.1088/1748-0221/12/07/P07014
98. M. Wu, C.A. Kruschwitz, D.V. Morgan et al., Monte carlo simulations of microchannel plate detectors. i. steady-state voltage bias results. Rev. Sci. Instrum. **79**, 073104 (2008). https://doi.org/10.1063/1.2949119
99. G. Cheng, L. Liu, Y. Liu et al, Monte carlo study of the single-surface multipactor electron discharge on a dielectric. IEEE Trans. Plasma Sci. **37**, 1968–1974 (2009). https://doi.org/10.1109/TPS.2009.2016967
100. Y. Xie, X. Wang, Y. Zhang et al., Monte-carlo simulation of spatial resolution of an image intensifier in a saturation mode. AIP Conf. Proc. **1955**, 040007 (2018). https://doi.org/10.1063/1.5033671
101. D. Systèmes, CST Studio Suite: Electromagnetic field simulation software, https://www.cst.com/ (2022)
102. L. Scientific Instrument Services (SIS) by Adaptas Solutions, Simion: The field and particle trajectory simulator, https://simion.com/ (2022)
103. S. Agostinelli, J. Allison, K. Amako et al., (GEANT4), GEANT4-a simulation toolkit. Nucl. Instrum. Meth. A **506**, 250–303 (2003). https://doi.org/10.1016/S0168-9002(03)01368-8
104. M.A. Furman, M.T.F. Pivi, Probabilistic model for the simulation of secondary electron emission. Phys. Rev. ST Accel. Beams **5**, 124404 (2002). https://doi.org/10.1103/PhysRevSTAB.5.124404
105. H. Miao, H. Peng, B. Yan et al., MCPSim: A Geant4-based generic simulation toolkit for electron multipliers represented by Microchannel Plate (2023). arXiv:2310.05122
106. H. Peng, B. Yan, H. Miao et al., Simulating the secondary electron avalanche of MCP by Geant4. Nucl. Instrum. Meth. A **1062**, 169163 (2024). https://doi.org/10.1016/j.nima.2024.169163
107. D.S. Evans, Low energy charged-particle detection using the continuous-channel electron multiplier. Rev. Sci. Instrum. **36**, 375–382 (1965)
108. J. Adams, B. Manley, The mechanism of channel electron multiplication. IEEE Trans. Nucl. Sci. **13**, 88–99 (1966). https://doi.org/10.1109/TNS.1966.4324084
109. L. Harris, Saturation in continuous channel electron multipliers. Rev. Sci. Instrum. **42**, 987–992 (1971)
110. M. Goldberg, A class of multi-symmetric polyhedra. Tohoku Math. J. **43**, 104–108 (1937)
111. S. Chen, S. Zhao, W. Xiong, et al., Design of a CsI(Tl) Calorimeter for Muonium-to-Antimuonium Conversion Experiment, Front. Phys. (2024). arXiv:2408.17114
112. J. M. Bauer (BaBar EMC Group), The BaBar electromagnetic calorimeter: Status and performance improvements, in 2005 IEEE Nuclear Science Symposium and Medical Imaging Conference, 2 pp. 1038–1042 (2005). https://doi.org/10.1109/NSSMIC.2005.1596430
113. M. Yeh, R.-Y. Zhu, M. Demarteau et al., Materials for Future Calorimeters (2022). arXiv:2203.07154

114. S. Zhao, Mustard: A modern, distributed offline software framework for HEP experiments, https://github.com/zhao-shihan/Mustard
115. S. Zhao, muc: a standard non-standard C++ library, https://github.com/zhao-shihan/muc (2024)
116. Message Passing Interface Forum, MPI: A Message-Passing Interface Standard Version 4.1 (2023)
117. R. Brun, F. Rademakers, ROOT: an object oriented data analysis framework. Nucl. Instrum. Meth. A **389**, 81–86 (1997). https://doi.org/10.1016/S0168-9002(97)00048-X
118. J. Allison, K. Amako, J. Apostolakis et al., Geant4 developments and applications. IEEE Trans. Nucl. Sci. **53**, 270 (2006). https://doi.org/10.1109/TNS.2006.869826
119. J. Allison, J. Apostolakis, S.B. Lee et al., Recent developments in Geant4. Nucl. Instrum. Meth. A **835**, 186–225 (2016). https://doi.org/10.1016/j.nima.2016.06.125
120. B. Jacob, G. Guennebaud et al., Eigen is a C++ template library for linear algebra: matrices, vectors, numerical solvers, and related algorithms, https://eigen.tuxfamily.org
121. G.M. Kurtzer, V. Sochat, M.W. Bauer, Singularity: scientific containers for mobility of compute. PLoS ONE **12**, e0177459 (2017). https://doi.org/10.1371/journal.pone.0177459
122. Epic Games, Unreal Engine 5, https://www.unrealengine.com (2021)
123. R.M. Djilkibaev, R.V. Konoplich, Rare muon decay $\mu^+ \to e^+e^-e^+\nu_e\bar{\nu}_\mu$. Phys. Rev. D **79**, 073004 (2009). https://doi.org/10.1103/PhysRevD.79.073004
124. P. Banerjee, T. Engel, A. Signer et al., QED at NNLO with McMule. SciPost Phys. **9**, 027 (2020). https://doi.org/10.21468/SciPostPhys.9.2.027
125. Y. Xu, Y.-S. Ning, Z.-Z. Qin et al., Development of a scintillating-fiber-based beam monitor for the coherent muon-to-electron transition experiment. Nucl. Sci. Tech. **35**, 79 (2024). https://doi.org/10.1007/s41365-024-01442-0
126. D. Pagano, G. Bonomi, A. Donzella et al., EcoMug: an efficient cosmic muon generator for cosmic-ray muon applications. Nucl. Instrum. Meth. A **1014**, 165732 (2021). https://doi.org/10.1016/j.nima.2021.165732
127. R. Shah and G. Majumder, Expected Performance of Cosmic Muon Veto Detector (2024). arXiv:2403.06114
128. A.M. Baldini, Y. Bao, E. Baracchini et al., (MEG), Muon polarization in the MEG experiment: predictions and measurements. Eur. Phys. J. C **76**, 223 (2016). https://doi.org/10.1140/epjc/s10052-016-4047-3
129. F. Fortuna, X. Marcano, M. Marín et al., Lepton flavor violation from diphoton effective interactions. Phys. Rev. D **108**, 015008 (2023). https://doi.org/10.1103/PhysRevD.108.015008
130. Y. Uesaka, M. Yamanaka, Y. Kuno, $\mu^- \to e^-\gamma$ in a muonic atom as a probe for effective lepton flavor-violating operators involving photon fields. Phys. Rev. D **111**(3), 035017 (2025)
131. V.W. Hughes, C.S. Wu, *Muon physics, weak interactions* (Academic Press, New York, 1975), p.98
132. Kuraray, Plastic Scintillating Fiber (PSF), http://kuraraypsf.jp/psf/sf.html
133. Y. Wang, Y. Yu, Multigap resistive plate chambers for time of flight applications. Appl. Sci. **11**, 111 (2020). https://doi.org/10.3390/app11010111

Springer Nature or its licensor (e.g. a society or other partner) holds exclusive rights to this article under a publishing agreement with the author(s) or other rightsholder(s); author self-archiving of the accepted manuscript version of this article is solely governed by the terms of such publishing agreement and applicable law.

Authors and Affiliations

Ai-Yu Bai[1,2] · Han-Jie Cai[3,4] · Chang-Lin Chen[5] · Si-Yuan Chen[1,2] · Xu-Rong Chen[3,4,6] · Yu Chen[1,2] · Wei-Bin Cheng[7] · Ling-Yun Dai[5,8] · Rui-Rui Fan[9,10,11] · Li Gong[7] · Zi-Hao Guo[12] · Yuan He[3,4] · Zhi-Long Hou[9] · Yin-Yuan Huang[1,2] · Huan Jia[3,4] · Hao Jiang[1,2] · Han-Tao Jing[9] · Xiao-Shen Kang[7] · Hai-Bo Li[4,9] · Jin-Cheng Li[3,4] · Yang Li[9] · Da-Ming Liu[13] · Shu-Lin Liu[4,9,11] · Gui-Hao Lu[1,2] · Han Miao[4,9] · Yun-Song Ning[1,2] · Jian-Wei Niu[3,14] · Hua-Xing Peng[4,9,11] · Alexey A. Petrov[15] · Yuan-Shuai Qin[3] · Ming-Chen Sun[1,2] · Jian Tang[1,2] · Jing-Yu Tang[16] · Ye Tian[3] · Rong Wang[3,4] · Xiao-Dong Wang[17,18] · Yi Wang[13] · Zhi-Chao Wang[1,2] · Chen Wu[9,10] · Tian-Yu Xing[19,20] · Wei-Zhi Xiong[21] · Yu Xu[22] · Bao-Jun Yan[9,11] · De-Liang Yao[5,8] · Tao Yu[1,2] · Ye Yuan[4,9] · Yi Yuan[1,2] · Yao Zhang[9] · Yongchao Zhang[12] · Zhi-Lv Zhang[3] · Guang Zhao[9] · Shi-Han Zhao[1,2]

✉ Jian Tang
tangjian5@mail.sysu.edu.cn

1 School of Physics, Sun Yat-sen University, Guangzhou 510275, China

2 Platform for Muon Science and Technology, Sun Yat-sen University, Guangzhou 510275, China

3 Institute of Modern Physics, Chinese Academy of Sciences, Lanzhou 730000, China

4 University of Chinese Academy of Sciences, Beijing 100049, China

5 School of Physics and Electronics, Hunan University, Changsha 410082, China

6 Southern Center for Nuclear Science Theory (SCNT), Institute of Modern Physics, Chinese Academy of Sciences, Huizhou 516000, China

7 School of Physics, Liaoning University, Shenyang 110036, China

8 Hunan Provincial Key Laboratory of High-Energy Scale Physics and Applications, Hunan University, Changsha 410082, China

[9] Institute of High Energy Physics, Chinese Academy of Sciences, Beijing 100049, China

[10] China Spallation Neutron Source, Dongguan 523803, China

[11] State Key Laboratory of Particle Detection and Electronics, Beijing 100049, China

[12] School of Physics, Southeast University, Nanjing 211189, China

[13] Key Laboratory of Particle and Radiation Imaging, Department of Engineering Physics, Tsinghua University, Beijing 100084, China

[14] School of Nuclear Science and Technology, Lanzhou University, Lanzhou 730000, China

[15] Department of Physics and Astronomy, University of South Carolina, Columbia, South Carolina 29208, USA

[16] School of Nuclear Science and Technology, University of Science and Technology of China, Hefei 230026, China

[17] School of Nuclear Science and Technology, University of South China, Hengyang 421001, China

[18] Key Laboratory of Advanced Nuclear Energy Design and Safety (MOE), University of South China, Hengyang 421001, China

[19] INFN Sezione di Milano, Milano 20133, Italy

[20] Universita degli Studi di Milano, Milano 20122, Italy

[21] Key Laboratory of Particle Physics and Particle Irradiation (MOE), Institute of Frontier and Interdisciplinary Science, Shandong University, Qingdao 266237, China

[22] Advanced energy science and technology Guangdong laboratory, Huizhou 516007, China